CONTENTS

sciendo

DOI 10.2478/ama-2019-0020

acta mechanica et automatica, vol.13 no.3 (2019)

ANALYSIS OF THE INFLUENCE OF MAGNETIC INDUCTION RAMP PROFILE ON AXIAL FORCE AND FRICTION TORQUE GENERATED BY MR FLUID

Wojciech HORAK*, Marcin SZCZĘCH*

*AGH University of Science and Technology Faculty of Mechanical Engineering and Robotics, Department of Machine Design and Technology, al. Mickiewicza 30, 30-059 Cracow, Poland

horak@agh.edu.pl, szczech@agh.edu.pl

received 21 July 2019, revised 10 July 2019, accepted 15 July 2019

Abstract: The unique properties of magnetic fluids result from their ability to undergo reversible, almost immediate, changes in their rheological properties under the influence of magnetic fields as well as the possibility to position them by magnetic field forces. It is also possible to control the direction and flow rate of such fluids. These properties provide an efficient way to develop new types of controllable machines and devices, such as brakes, clutches and bearings. The objective of the study was to examine the axial force and torque friction of a magnetorheological (MR) fluid working in the shear flow mode (parallel plate system) subjected to different magnetic induction ramp profiles. The rotation speed and working gap height were also taken into account. Determining the response of the tested system to magnetic induction change in different working conditions was of particular interest.

Key words: MR Fluid, Axial Force, Torque, Control, Experiments, Magnetic Field Ramp

1. INTRODUCTION

Magnetorheological (MR) fluids are smart materials with controllable rheological characteristics that may be modified by external magnetic fields. These materials are suspensions of particles made of ferromagnetic material immersed in a carrier fluid that does not exhibit magnetic properties. MR fluids consist of particles with a size of up to a few micrometres, unlike ferrofluids (FFs) that are produced based on the particles with a diameter of several nanometres (Raj et al., 1995; Rosenweig, 1985; Vekas, 2008). The magnetic particles are usually covered with a surface-active compound in order to prevent the aggregation and sedimentation of the suspension. The properties of the fluid may be different because of the changes in the microstructure of the suspension occurring in the magnetic field (Odenbach et al., 2007). In the macroscopic scale, the magnetic field affects the stress state in a fluid in both the tangential (Lopez-Lopez et al., 2010; Odenbach et al., 2007; See and Tanner, 2003) and normal directions (Guo and Gong, 2012; Horak et al., 2017a, b). The range of change in rheological properties is a function of several factors, in particular, volume fraction of the magnetic particles in the fluid, magnetic properties of the particle material, surfactant type, carrier fluid type, particle size and shape. The behavior of MR fluids also depends on deformation conditions such as deformation rate (Horak et al., 2017b), flow direction [pressure (Kubik et al., 2017), shear (Guo and Goong, 2012; Jang et al., 2011; See and Tanner, 2003) or squeeze flow mode (Hegger and Maas, 2016)] and magnetic field distribution.

MR fluids are used in various technical applications, such as vibration dampers (Ajay Kumar et al., 2016; Bajkowski, 2012; Jasrzębski and Sapiński, 2017), brakes and clutches (Guldbake and Hesselbach, 2006), valves (Lopez-Lopez et al., 2010), bearings (Horak et al., 2017b) and precision polishing (Wang et al., 2016).

The parallel plate system used in the tests occurs in both measuring devices, for example, in the case of testing the rheological properties of magnetic fluids, as well as controllable devices, such as brakes or thrust bearings (Laun et al., 2008).

In the case of rheological tests, flow curves or the viscous and elastic modulus are determined under the influence of the magnetic field. But in contrast to this type of research, this publication describes the laboratory tests of the axial force and torque friction generated by selected MR fluids in this system. Different rotational speed and gap heights are considered. The phenomena occurring inside the MR fluid structure during the magnetic induction change are complicated and depend on many parameters (Chen et al., 2013). The purpose of the work was to describe the transient states of the particle structure change in the fluid observed during measurements in the case of increasing and decreasing ramp profile of magnetic field induction. The test results show the problems of using this type of fluid in controllable systems.

2. EXPERIMENTAL SETUP

The research experiments were performed on a test stand for the examination of magnetic fluids in shear and squeeze flow modes, described in detail in Horak et al. (2017c). The scheme of the device is presented in Figure 1a. On the support frame, there is an axial drive consisting of a linear servo motor (1) on which a rotary servo motor (2) is mounted.

An essential part of the measurement system is the torque and axial force transducer (3) on which the measuring plate is mounted. The examined sample is placed in the test cell (4). The scheme of the test cell is shown in Figure 1b. The magnetic fluid (6) is placed in the measuring gap formed between the flat rotary plate (5) and the core of the electromagnet (8). The value of magnetic induction is controlled by the current in the coil of the

DOI 10.2478/ama-2019-0020

electromagnet (9). A magnetic circuit is closed by the lower and upper parts of the test cell (7). Some elements (7 and 8) are made of ferromagnetic material. The rotary plate is made of a material with paramagnetic properties. The diameter of electromagnet core is d_r = 45 mm, and that of rotary plate is 60 mm. The height of magnetic gap is z = 9 mm. The height of the measuring gap h is adjustable by a linear servomotor with an accuracy of ±1 μm.

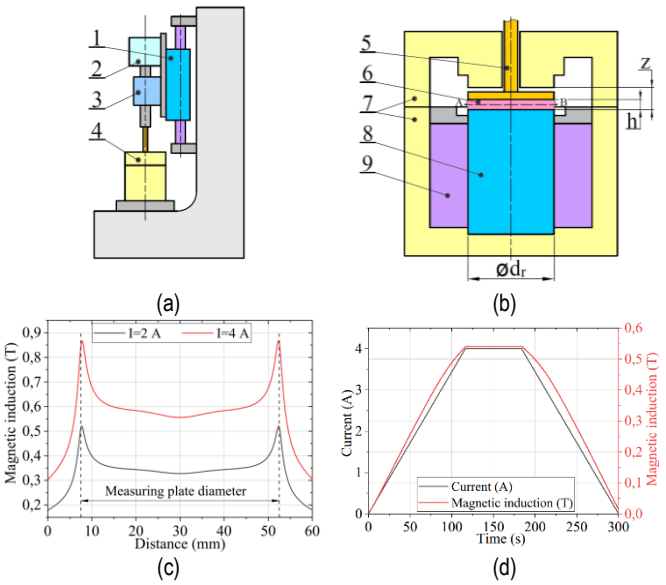

Fig. 1. (a) General view of the test stand, (b) scheme of the test stand, (c) scheme of the test cell and (d) distribution of the magnetic induction in the gap

Figure 1c shows the magnetic induction distribution in the measuring gap (measurement between Points A and B; see Fig. 1b). The magnetic induction is not a constant value on the plate diameter. On the edge of the core there is a local increase in the value. This provides the self-sealing effect [10] and the magnetic fluid is held in the region of the measuring gap. In turn, in the electromagnet core axis region, there are local decreases in the magnetic induction because of the opening present in the upper part of the test cell.

The tests were carried out for three measuring gap heights h = 0.25, 0.5 and 1 mm; the volume of the MR fluids was, respectively, v = 0.4, 0.8 and 1.6 ml. Each measurement was performed at the rotational speeds of n = 0, 1, 10, 50 and 100 min^{-1}. The trapezoidal current curve in the electromagnet coil was within the range I = 0–4 A, which corresponded to the magnetic induction B = 0–540 mT. The coil current curve can be divided into three stages: increase during 115 s, next stabilisation for 70 s and then decrease for the next 115 s. The slope of current change is 0.34 A/min. The current change and the corresponding magnetic field induction are shown in Figure 1d. Magnetic induction measurement was performed in the middle of the measuring plate diameter. In the electromagnet core and in the lower and upper parts of the test cell, there are orifices through which the coolant fluid flows. This provides temperature stabilisation of the cell. The tests were carried out under thermal stabilisation conditions at 20°C.

The examined fluid was hydrocarbon-based MR fluid (type: MRF-122EG) produced by LORD Corporation. It is known from the product card that the magnetic particle volume fraction is estimated as 22%, and the viscosity at 40°C in the absence of the magnetic field is 42 mPa·s. The saturation magnetisation is 360 kA/m. The fluid choice resulted from the relatively small particle volume fraction and the high saturation magnetisation. This fluid also has a wide range of applications, such as shock dampers and brakes.

Magnetic circuit elements have ferromagnetic properties and are characterised by residual magnetisation that is present when an external magnetic field is removed. Therefore, before every measurement, a demagnetising procedure was carried out. Demagnetisation was accomplished by supplying the electromagnet coil with a sinus function decaying in time (see Horak et al., 2017c). This ensured the repeatability conditions under which the research was conducted.

3. RESULTS AND DISCUSION

Figure 2 shows the results of axial force and torque measurement obtained at various rotational speeds and gap heights. For all cases, the axial force value (Fig. 2 a–c) observed in time differs significantly from the shape of the magnetic induction ramp. The smallest force values are achieved for the gap h = 0.25 mm and when the plate is not rotating.

Moreover, in the case of non-rotating plates, for different gaps, high force maintains for some time as a relatively constant value despite lowering magnetic induction. A similar phenomenon has been observed in Salwiński and Horak (2011). This behavior indicates that the normal force in MR fluids is the result not only of the magnetostatic pressure (Rosenweig, 1985), but even after magnetic field decay, the force can be maintained (in the absence of other extortions). This may be associated with the formation of lattice structures of ferromagnetic particles in the MR fluid, and especially the interaction of friction forces between particles (Hegger and Mass, 2016; Li and Zang, 2008). It can be seen that, during the first stage of the experiment, the axial force response is delayed compared to the current changes, with this phenomenon particularly visible in the absence of rotational speed.

Over in the time interval (0–25 s), the force for a certain time has a local upward trend, which temporarily undergoes a downward or stabilising trend and, for the case shown in Figure 2a, the force for some time even takes a negative value (about −4 N). This is probably due to the fact that, for some time, the particles in the MR fluid move towards the region of the highest magnetic induction (see Fig. 1c).

In an upward trend, the axial force curves for all speeds are similar, whereas the results obtained for the downward magnetic induction ramp show that, for all cases at higher rotational speeds, the axial force has lower values. This is probably associated with faster structure destruction inside the magnetic fluid, see also Gong et al. (2012), Guo and Gong (2012) Lopez-Lopez et al. (2010) and See and Tanner (2003). However, as the presented test results show, the influence of rotational speed on the normal force also depends on the ramp direction of magnetic field change.

During the second experiment stage (constant current), after a certain time, the force stops growing, and in the case of the speeds of 0, 1 and 10 min^{-1}, a constant value of the force, or even an increase, is observed. At 50 and 100 min^{-1}, in most cases, the force begins to decrease over time or some fluctuations are observed. Assuming the influence of the internal structure of MR

DOI 10.2478/ama-2019-0020

fluid on the value of the axial force, such results indicate that there is a limit rotational speed below which shearing does not decrease or even improve the ability of MR fluid to generate normal force. The state of magnetic particle chain formation can be considered through an analysis of the interplay between magnetic and hydrodynamic interactions, typically expressed using the Mason number (Klingenberg et al., 2007). The presence of sufficiently small Mason number values (at low rotational speed) encourages the formation of internal MR fluid structures (Shan et al., 2015). In addition, the shear deformation of MR fluid changes the contact conditions among the particles, thus changing the frictional forces (Hegger and Maas, 2016; Li and Zhang, 2008), with such a hypothesis additionally confirming the obtained results.

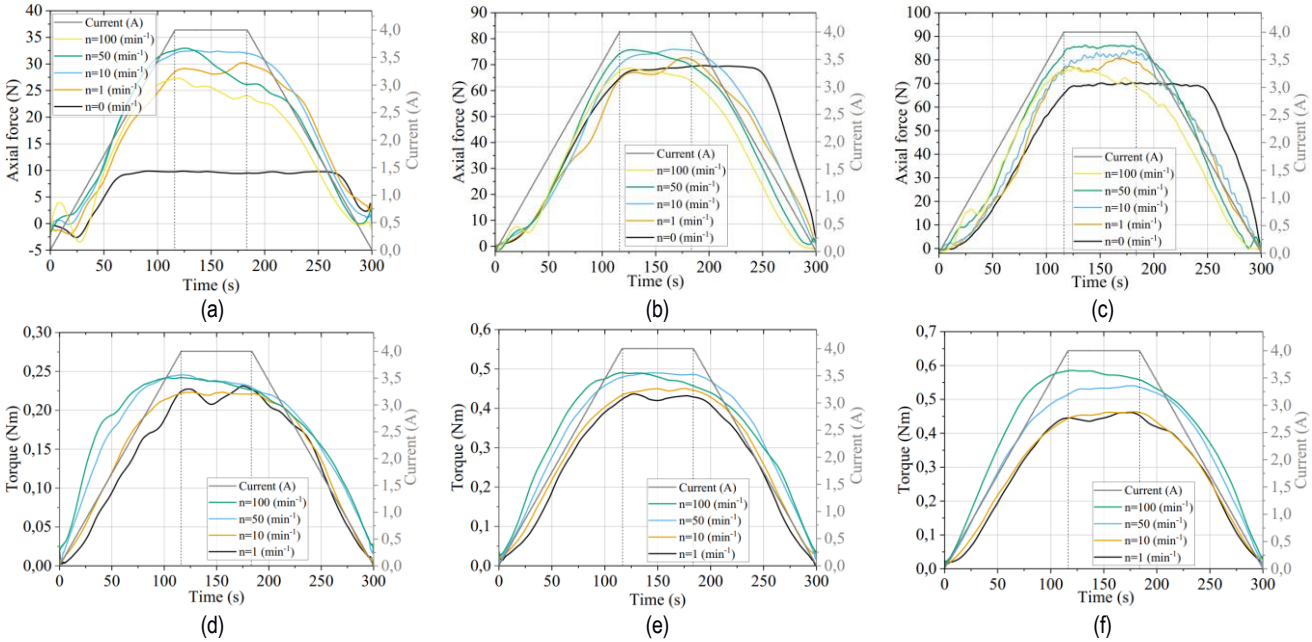

Fig. 2. Axial force measurement: (a) h = 0.25 mm, (b) h = 0.5 mm and (c) h = 1 mm. Torque measurement: (d) h = 0.25 mm, (e) h = 0.5 mm and (f) h = 1 mm

In Figure 3, the axial force slopes during the time of current force increasing and decreasing trends were shown. On the basis of the results, it can be concluded that the higher gap and the presence of rotational speed accelerates and facilitates the formation of axial force to a certain extent.

Figure 2d–f shows torque changes over measuring time. The curves, compared to the force response, are more similar in the shape of the applied current change (Fig. 1d). An asymmetry in value is also noticeable when comparing increasing and decreasing trends, which may be related to the magnetic hysteresis of the measuring cell elements. In the stage of constant current, the torque does not stabilise and, in most cases, a slight decrease in torque can be observed.

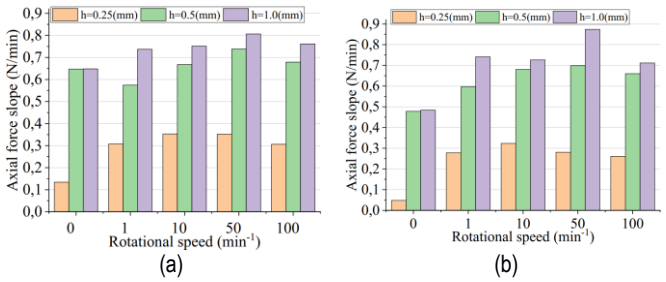

Fig. 3. Axial force slope: (a) current upward trend and (b) current downward trend

In the case of torque measurement, no significant differences are observed in the case of slope value between the upward and downward trends (see Fig. 4). Generally, higher slopes are observed for higher measuring gap heights. In the analysed case, there is no noticeable trend determining the impact of rotational speed on this parameter.

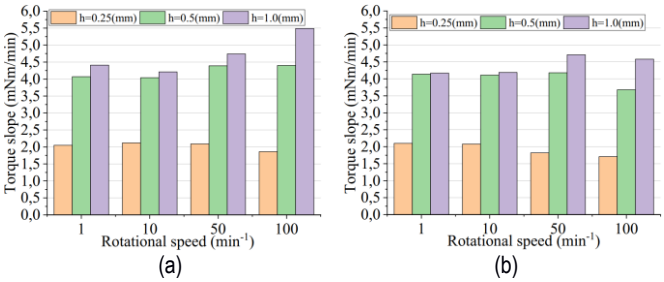

Fig. 4. Torque slope: (a) current upward trend and (b) current downward trend

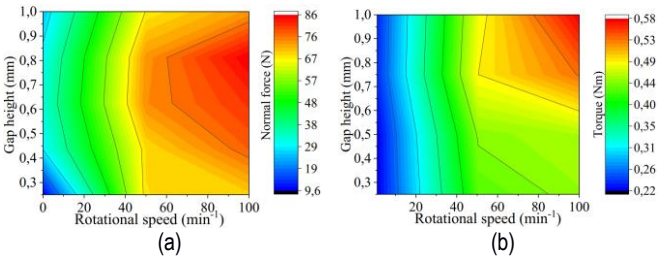

Fig. 5. Contour plots of mean: (a) axial force and (b) torque

DOI 10.2478/ama-2019-0020

Figure 5 shows contour plots illustrating the influence of the gap height and rotational speed on the axial force and torque. The charts were developed based on the average value measured during the constant current stage, and the graphs are the result of measured data interpolation.

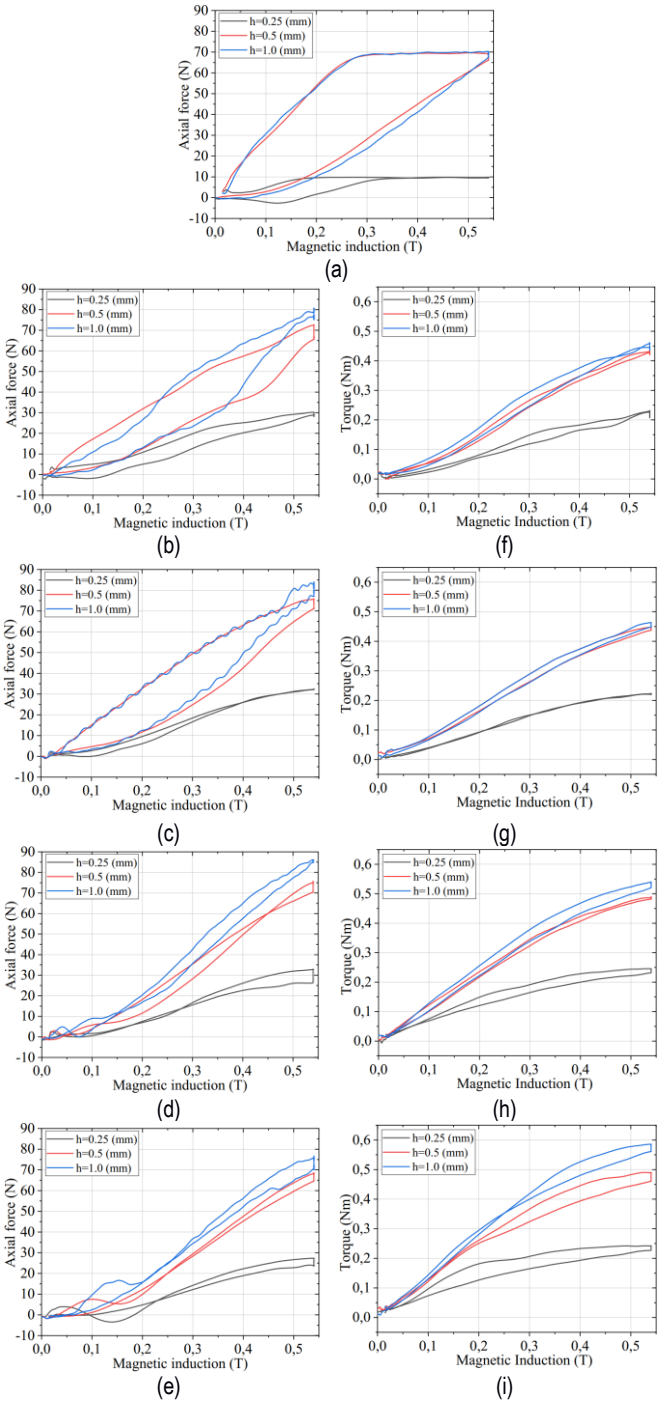

Fig. 6. Axial force versus magnetic induction hysteresis loops: (a) n = 0, (b) n = 1, (c) n = 10, (d) n = 50 and (e) n = 100 min^{-1} and torqueversus magnetic induction hysteresis loops: (f) n = 1, (g) n = 10, (h) n = 50, (i) n = 100 min^{-1}

As can be seen in Figure 5a, specified rotational speed and gap height values favour obtaining the highest axial force. Relatively small and excessively large gap height lowers the axial force. In the case of torque, higher values are observed for higher rotational speeds as well. Increasing the height of the working gap leads to higher values of torque (Fig. 5b). In the general case, an increase in torque (shear stress) according to the Bingham model as a result of increased share rate is expected (Horak et al., 2017b). As can be seen, the obtained results also show the significant influence of the MR fluid volume (layer height). The shear rate for higher rotational speed (100 min^{-1}) and the narrowest gap (0.25 mm) are 4 times higher in relation to the same rotational speed and the widest measuring gap (1 mm), but the measured torque is 2.6 times lower for a narrower gap.

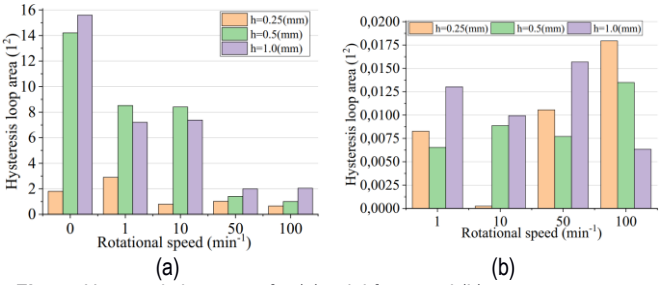

Fig. 7. Hysteresis loop area for (a) axial force and (b) torque

Figure 6 shows measured parameters versus magnetic induction as hysteresis loops. For the axial force when the measuring plate is non-rotating (Fig. 6a), h = 0.25 mm, the force reaches its maximum value at a relatively low magnetic field induction (about 0.15 T), however, the obtained force values are the lowest. Rotational speed (Fig. 6b–e) improves the ability to generate axial force, moreover, as shown in Figure 7a; for these measurements, the results have been obtained with a smaller hysteresis loop area, which may indicate an improvement in controlling the axial force in the presence of rotation.

In the case of torque curves (Fig. 6f–i), hysteresis loops are smaller (even several times) than those in the case of axial force (compare Fig. 7a to 7b). This observation is consistent with other experimental work (Szczęch and Horak, 2017).

4. CONCLUSIONS

An important aspect of MR fluid application in controllable machines and devices, such as brakes, clutches and bearings, is the ability to change the value of the force and the torque as a result of the magnetic induction variation. The main conclusions from the conducted studies can be formulated as follows:

- The axial force and torque value are significantly dependent on the height of the working gap and the rotational speed.
- Narrow as well as relatively wide gaps adversely affect the fluid ability to generate a normal force. This dependence is particularly noticeable at low rotational speeds.
- Owing to the ability of the MR fluid to generate the highest axial force, it is advantageous to subject the MR fluid to a correspondingly high deformation rate. Excessively high deformation causes a reduction in the axial force.
- The rotational speed may adversely affect the stability in the time of the axial force at certain magnetic field parameters (see Fig. 2a–c).
- Under the same rotational speeds, higher values of torque are observed for higher measuring gap heights.

- The response of the MR fluid in the form of a change in axial force and friction torque has a distinctly different course. A more complex issue is definitely the control of the axial force than the torque.

REFERENCES

1. **Ajay Kumar H. N., Shilpashree D. J., Adarsh M. S., Amith D., Kulkarni S.** (2016), Development of Smart Squeeze Film Dampers for Small Rotors, *Procedia Engineering*, 144, 790-800,
2. **Bajkowski J.M.** (2012), Design, analysis and performance evaluation of the linear, magnetorheological damper, *Acta Mechanica et Automatica*, 6(1), 5-9.
3. **Chen S., Huang J., Shu H., Sun T., Jian K.,** (2013) Analysis and Testing of Chain Characteristics and Rheological Properties for Magnetorheological Fluid, *Advances in Materials Science and Engineering*, 2013, 1-6.
4. **Gong X., Guo, Ch., Xuan Sh., Liu T., Zong L., Peng Ch.** (2012), Oscillatory normal forces of magnetorheological fluids, *Soft Matter*, 8(19), 5256-5261,
5. **Guldbakke J. M., Hesselbach J.** (2006), Development of bearings and a damper based on magnetically controllable fluids, *Journal of Physics*, 18, 2959.
6. **Guo Ch.Y., Gong X.L**. (2012,) Normal forces of magnetorheological fluids under oscillatory shear, *Journal of Magnetism and Magnetic Materials*, 324(6), 1218-1224.
7. **Hegger C. and Maas J.** (2016) Investigation of the squeeze strengthening effect in shear mode, *J. Intell. Mater. Syst. Struct.*, 27 1895–907.
8. **Horak W., Salwiński J., Szczęch M.** (2017a), Analysis of the influence of selected factors on the capacity of thrust sliding bearings lubricated with magnetic fluids, T*ribologia*, 48(4), 33–38.
9. **Horak W., Salwiński J., Szczęch M**. (2017b), Experimental Study on Normal Force in MR Fluids Under Low and High Shear Rates, *Machine Dynamics Research*, 41(1), 89-100.
10. **Horak W., Salwiński J., Szczęch M.** (2017c), Test stand for the examination of magnetic fluids in shear and squeeze flow mode, *Tribologia*, 48(2), 67–75.
11. **Jang K.I., Min B.K., Seok J.** (2011), A behavior model of a magnetorheological fluid in direct shear mode, *Journal of Magnetism and Magnetic Materials*, 323(10), 1324-1329.
12. **Jastrzębski Ł., Sapiński B.** (2017), Experimental Investigation of an Automotive Magnetorheological Shock Absorber, *Acta Mechanica et Automatica*, 11(4), 253-259.
13. **Klingenberg D.J., Ulicny J.C., Golden M.A.** (2007), Mason numbers for magnetorheology, *Journal of Rheology*, 51(5), 883–893;
14. **Kubík M., Macháček O., Strecker Z., Roupec J., Mazůrek I.** (2017), Design and testing of magnetorheological valve with fast force response time and great dynamic force range, *Smart Material and Structure*, 26 047002.
15. **Laun H. M., Schmidt G., Gabriel C., Kieburg C.**, (2008) Reliable plate–plate MRF magnetorheometry based on validated radial magnetic flux density profile simulations, *Rheologica Acta*, 47(9), 1049-1059.
16. **Li W., Zhang X**. (2008), The effect of friction on magnetorheological fluids, *Korea-Aust. Rheol. J*., 20, 45–50.
17. **López-López M.T., Kuzhir P., Durán J.D.G, Bossis G.** (2010), Normal stresses in a shear flow of magnetorheological suspensions: Viscoelastic versus Maxwell stresses, *Journal of Rheology*, 5(5), 1119-1136
18. **Odenbach S., Pop L.M.**, **Zubarev A.Yu**. (2007), Rheological properties of magnetic fluids and their microstructural background, *GAMM-Mitt*, 1, 195-204.
19. **Raj K., Moskowitz B., Casciari R.** (1995), Advances in ferrofluid technology, *Journal of Magnetism and Magnetic Materials*, 149, 174-180.
20. **Rosensweig R.E**. (1985), *Ferrohydrodynamics*, Cambridge University Press, Cambridge.
21. **Salwiński J., Horak W.** (2011), Measurement of normal force in magnetorheological and ferrofluid lubricated bearings, *Key Engineering Materials*, 490, 25-32.
22. **See H., Tanner R.** (2003), Shear rate dependence of the normal force of a magnetorheological suspension, *Rheologica Acta*, 42(1-2),166-170.
23. **Shan L., Chen K., Zhou M., Zhang X., Meng Y., Tian Y.** (2015), Shear history effect of magnetorheological fluids, *Smart Materials and Structures*, 24(10), 105030.
24. **Szczęch M., Horak W.** (2017), Numerical simulation and experimental validation of the critical pressure value in ferromagnetic fluid seals, *IEEE Transactions on Magnetics*, 53(7), 1–5.
25. **Vekas L.** (2008), Ferrofluids and Magnetorheological Fluids, *Advances in Science and Technology*, 54, 127-136.
26. **Wang Y., Yin S., Huang H.**, (2016) Polishing characteristics and mechanism in magnetorheological planarization using a permanent magnetic yoke with translational movement, *Precis. Eng.*, 43, 93–104.

This work is financed by AGH University of Science and Technology, Faculty of Mechanical Engineering and Robotics, research program No. 16.16.130.942

DOI 10.2478/ama-2019-0021

NON-LINEAR ANALYSIS OF AIR PRESSURE FLUCTUATIONS DURING BUBBLE DEPARTURE SYNCHRONISATION

Paweł DZIENIS*, Romuald MOSDORF*, Tomasz WYSZKOWSKI, Gabriela RAFAŁKO*

*Faculty of Mechanical Engineering, Bialystok University of Technology, Wiejska 45C, 15-351 Białystok, Poland

p.dzienis@pb.edu.pl, r.mosdorf@pb.edu.pl, wyszkowski.tomasz@gmail.com, girejkogabriela@gmail.com

received 27 May 2019, revised 6 September 2019, accepted 10 September 2019

Abstract: In the recent paper, non-linear methods of data analysis were used to study bubble departure synchronisation. In the experiment, bubbles were generated in engine oils from two neighbouring brass nozzles (with an inner diameter of 1 mm). During the experiment, the time series of air pressure oscillations in the air supply system and voltage changes on phototransistor were recorded. The analysis of bubble departure synchronisation was performed using a correlation coefficient. The following methods of non-linear data analysis are considered. Fast Fourier Transformation, autocorrelation, attractor reconstruction, correlation dimension, largest Lyapunov exponent and recurrence plot analysis were used to examine the correlation between bubbles behaviour and character of pressure fluctuations. Non-linear analysis of bubble departure synchronisation revealed that the way of bubble departures from two neighbouring nozzles does not depend simply on the character of pressure fluctuations in the nozzle air supply systems. The chaotic changes of the air pressure oscillations do not always determine the chaotic bubble departures.

Key words: Bubble Departures, Alternative Bubble Departures, Nonlinear Methods of Data Analysis

1. INTRODUCTION

The bubbles–bubbles and bubbles–liquid interactions occur in many technological applications such as hydrocarbon industries, chemical processes, bubble column reactors or boiling heat transfer. Understanding the interactions between moving gas bubbles in oils would be useful in optimising the devices for degassing or transporting oils (Lavensona et al., 2016).

The interactions between bubbles generated in water and silicone oils from two adjacent orifices were discussed in the articles by Sanada et al. (2009), Legendere et al. (2003) and Snabre and Magnifotcham (1997). It was concluded that interactions between bubbles can cause two kinds of bubble behaviours – bubble coalescence and bubble bouncing. The kinds of bubble behaviours depend on Reynold, Morton and Webber numbers concerning bubbles. In the case when bubbles do not coalesce, then the alternative, chaotic or simultaneous bubble departures from neighbouring nozzles occur. The bubbles generated in the water and an aqueous glycerine solution from two neighbouring microtubes were analysed and described in the article by Kazakis et al. (2008). It was shown that bubbles–bubbles interactions depend on liquid properties, gas flow rate and distance between the tubes. Alternative bubble departures were investigated by Mosdorf and Wyszkowski (2011, 2013). The mentioned works confirm that bubbles departed from neighbouring nozzles interact with each other. Interactions between bubbles cause the moving bubbles to form unique structures above nozzle outlets. During alternative bubble departures, bubbles depart periodically. Such interactions modify the hydrodynamic condition above the nozzle outlets. Consequently, they modify the air pressure oscillations in air supply systems (Fermat et al., 1998; Vazques et al., 2010; Dzienis and Mosdorf, 2014). The synchronisation of bubble departures from neighbouring nozzles related to air pressure changes is not fully understood.

Vezques et al. (2010), Dzienis and Mosdorf (2014) and Mosdorf et al. (2017) suggested that bubbles behaviour over the nozzle's outlet is correlated with air pressure fluctuations. Usually, both bubbles behaviour and pressure fluctuations have a chaotic character. In the recent article, pressure signals recorded in two nozzles (with an inner diameter of 1 mm) of the gas supply system are investigated using methods of non-linear data analysis. The following methods of non-linear data analysis were used: Fast Fourier Transformation, autocorrelation, attractor reconstruction, correlation dimension, largest Lyapunov exponent and recurrence plot (RP) analysis. The analysis was conducted for an almost periodic bubble departure processes. The process was almost periodic but not completely correlated with the air pressure changes in the air supply system. The changes in time of alternative and simultaneous bubble departures were observed. In this article, the correlation between bubbles behaviour and pressure fluctuations character is examined. The recent article shows that the character of bubble departures from two neighbouring nozzles does not depend simply on the pressure fluctuations in the nozzle air supply systems. The chaotic changes in the air pressure oscillations do not always determine the chaotic bubble departures.

2. EXPERIMENTAL SETUP AND DATA CHARACTERISTICS

In the experiment, bubbles were generated from two neighbouring brass nozzles to the glass tank with the dimensions

of 400×400×700 mm. The tank (Fig. 1 – 2) was filled with mineral engine oil. Nozzles with an inner diameter of 1.1 mm (Fig. 1 – 1) were placed at the bottom of a tank. The distance (*S*) between nozzles was equal to 4 mm. The scheme of the experimental setup is shown in Fig. 1.

The air was supplied to air tanks using air pumps (Fig. 1 – 9). The air pressure was set using the proportional pressure reducing valves – Metalwork Regtronic (Fig. 1 – 7). The adjustable pressure range of pressure reducing valve was 0.05–10 bar. The accuracy of the pressure reducing valve was 0.5%. During the experiment, the air pressure was equal to 0.2 bar. The air volume flow rate was measured using flow meters – MEDSON s.c Sho-Rate-Europe Rev D, P10412A (Fig. 1 – 4) with an accuracy of 5%. The air volume flow rate was in the range of 0.014 L/min to 0.125 L/min. During the experiment, the temperature of the liquid was approximately 20°C. The temperature of the liquid was controlled by the digital thermometer – MAXIM DS18B20.

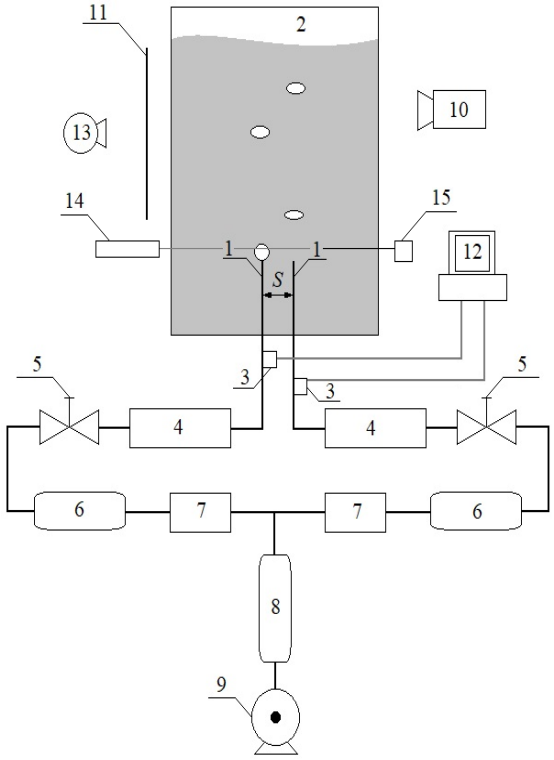

Fig. 1. Schema of experimental setup. 1 – nozzles, 2 –glass tank, 3 – pressure sensors, 4 – flow meters, 5 – air valves, 6 – air tanks, 7 – pressure regulators, 8 – air tank, 9 – air pomp, 10 – high speed camera, 11 – shutter, 12 – data acquisition station, 13 – light source, 14 – laser, 15 – phototransistor

In the experiment, bubble movement, time series of voltage changes on phototransistor and pressure changes in the gas supply system were recorded. Bubble movement was recorded using a high-speed camera – CASIO EX FX 1 (Fig. 1 – 10). Videos were recorded in grey scale with a speed of 600 fps. The gathered films were divided into frames. The example video frames are shown in Fig. 2.

In Fig. 2, two subsequent frames of bubble chain formation are presented for air volume flow rates of 0.0260 L/min and 0.0657 L/min. The time period between frames marked with I and II in Fig. 2 is equal to 0.039 s. When the air volume flow rate is q = 0.0260 L/min, then two bubbles coalesce above nozzle outlets (Fig. 2). When the air volume flow rate is 0.0657 L/min, then four bubbles coalesce above the nozzle outlet. The different number of coalesced bubbles causes a decrease in the distance between subsequent bubbles. Despite the fact that the frequency of bubble departures is the highest in the case presented in Fig. 2b, the bubble distance is greater in comparison with the mentioned distance in Fig. 2a.

Air pressure fluctuations were measured with the silicon pressure sensor – Frescale Semiconductor MPX12DP (Fig. 1 – 3). Time series of pressure changes were recorded using data acquisition station DT9800 (Fig. 1 – 12) with a sampling frequency of 1 kHz. The time series for particular air volume flow rates (*q*) are presented in Fig. 3.

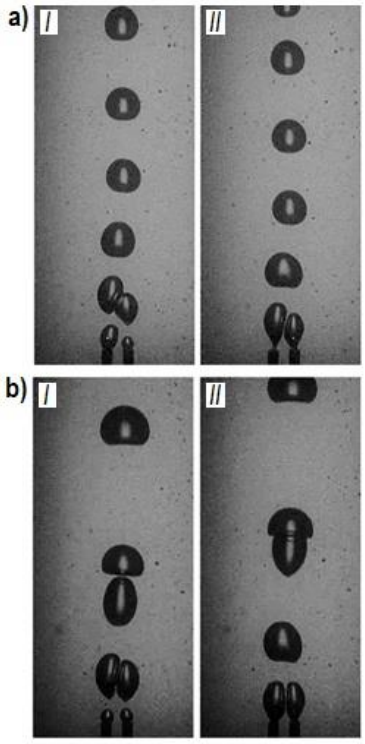

Fig. 2. The example frames of recorded videos. (a) Air volume flow rate *q* = 0.0260 L/min (alternative bubble departures happen – frame *I*) and (b) air volume flow rate *q* = 0.0657 L/min (simultaneous bubble departures happen – frame *II*)

Pressure oscillations in gas supply systems for air volume flow rate *q* = 0.0260 L/min are presented in Fig. 3a (left nozzle) and Fig. 3b (right nozzle). In the time series of pressure changes in both nozzles, the following phenomena appear: pressure fluctuations caused by bubble departures and long-term pressure oscillations. The long-term pressure oscillations decrease in the left nozzle as the expenditure increases the air volume flow rate (Fig. 3). In this case, the bubbles departed in an almost periodic way. In the right nozzle, long-term pressure oscillations occurred despite the increase of air volume flow rate (Fig. 3d). In this case, the bubbles departed in a non-periodic way. The occurrence of long-term pressure oscillations and the different characters of bubble departures lead the authors of this article to use non-linear methods of data analysis to study the interactions between departed and growing bubbles.

Moreover, during the experiment, the bubble growing time was measured using a laser–phototransistor system. The laser beam was placed approximately 1 mm above the nozzle outlets. The process of bubble growing caused the interruption of the laser

DOI 10.2478/ama-2019-0021

beam. The voltage on the phototransistor for the bubble growth was equal to ~0.2 V. After the bubble departure, the laser beam was not interrupted. At this moment, the value of the voltage was equal to ~4.8 V. Time series of voltage changes on phototransistor were recorded simultaneously with a time series of pressure fluctuations.

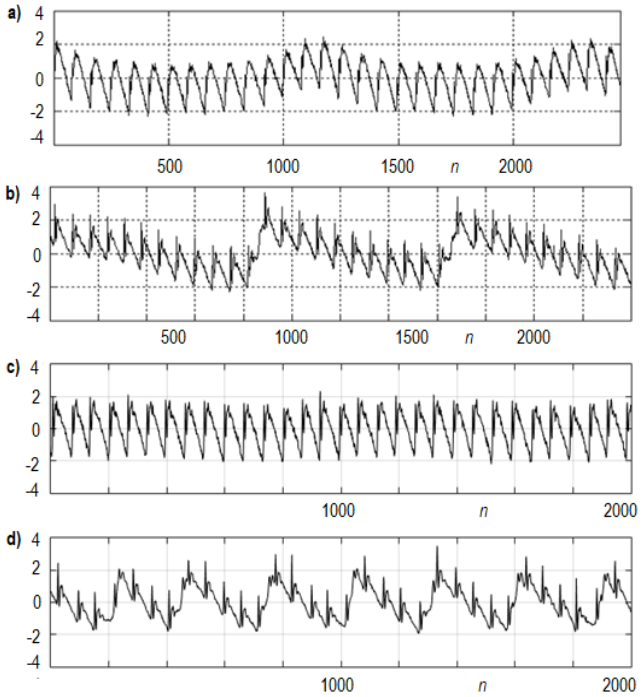

Fig. 3. The time series of pressure changes in gas supply system in the left and right nozzles: (a) q = 0.0260 L/min, left nozzle; (b) q = 0.0260 L/min, right nozzle; (c) q = 0.0657 L/min, left nozzle and (d) q = 0.0657 L/min, right nozzle

In order to determine the duration of the simultaneous and alternative bubble departures, the correlation coefficient (Cor) was calculated in the moving window of time which is equal to a single cycle of bubble departures (~0.14 s for 85 samples, Fig. 3a and b; ~0.12 s for 71 samples, Fig. 3c and d). *Cor* was calculated according to the following formula:

$$Cor = \frac{Cov(x_{i,L}, x_{i,R})}{\sigma_{x,L}, \sigma_{x,R}} \quad (1)$$

where: *cov* is the covariance, σ is the standard deviation of signal, $x_{i,L}$ denotes the time series of pressure fluctuations in left nozzle and $x_{i,R}$ is the time series of pressure fluctuations in the right nozzle.

When *Cor* tends to 1 or −1, then time series $x_{i,L}$ and $x_{i,R}$ are correlated. When *Cor* is close to 0, then the time series $x_{i,L}$ and $x_{i,R}$ are not correlated. When value *Cor* is close to 1, then bubbles depart (from twin nozzle) at the same time. When the value of *Cor* is negative, then bubbles depart alternatively. The changes of *Cor* for pressure fluctuations time series are presented in Fig. 4.

The correlation coefficient was calculated for a time series of pressure fluctuations (dotted lines – Fig. 4) and time series from phototransistor (solid line – Fig. 4). The correlation coefficient evaluated from phototransistor signals is helpful to determine the time period of alternative or simultaneous bubble departures.

In the case presented in Fig. 3a (q = 0.0260 L/min), alternative bubble departures occur during five subsequent cycles of bubble departures and are interrupted by two acts of simultaneous bubble departures. In Fig. 3b, the occurrence period of alternative bubble departures is equal to 10 cycles. The reappearance of alternative bubble departures takes place after three cycles of simultaneous bubble departures. It can be concluded that the increase of air volume flow rate causes an elongation of the alternative bubble departure occurrence period.

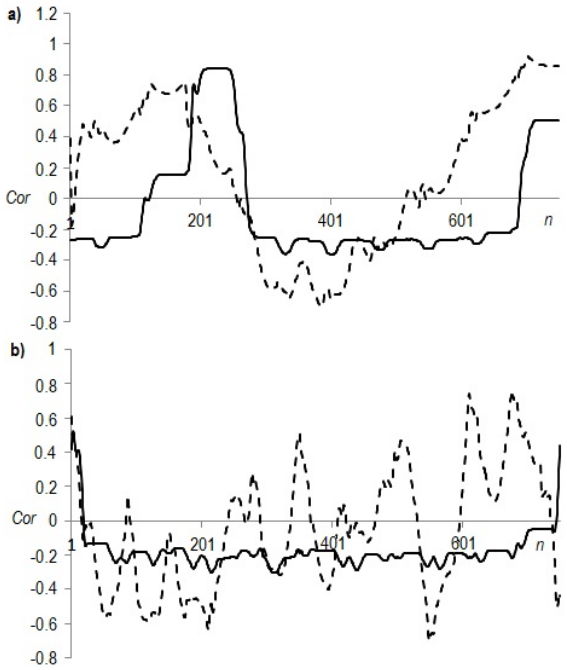

Fig. 4. The correlation coefficient, *Cor*, changes for pressure fluctuations (dotted lines) and phototransistor signals (solid lines): (a) q = 0.0260 L/min and (b) q = 0.0657 L/min

During the alternative bubble departures (presented in Fig. 3b), intense, chaotic fluctuations of the air pressure correlation coefficient were observed. During the alternative bubble departures (presented in Fig. 3a), the value of the correlation coefficient increased continuously and its oscillations were weaker in comparison with the case presented in Fig. 3b.

3. NON-LINEAR ANALYSIS OF PRESSURE FLUCTUATIONS

The following methods of non-linear data analysis are used in this study:

- the frequency analysis – Fast Fourier Transformation,
- autocorrelation,
- attractor reconstruction,
- calculation of correlation dimension and largest Lyapunov exponent, and
- RP analysis.

3.1 The frequency analysis

The frequency of bubble departures is constant during periodic bubble departures; but when bubbles depart chaotically, then the frequency of bubble departures is variable. The observation proves that analysis of bubble departures' frequency

is complicated. Therefore, to estimate the frequency of bubble departures, the Fourier Transformation was introduced. The Fourier Transformation evaluates the time-domain data in the frequency domain, which is treated as bubble departures' frequency. The Fourier Transformation has the following form (Torrence and Compo, 1998):

$$F_k = \sum_{n=0}^{n-1} x_n e^{-j\frac{2\pi}{n}kl} \tag{2}$$

The power spectrum is defined as $P=|F_k|^2$. Power spectrums for time series of pressure changes in gas supply systems are shown in Fig. 5.

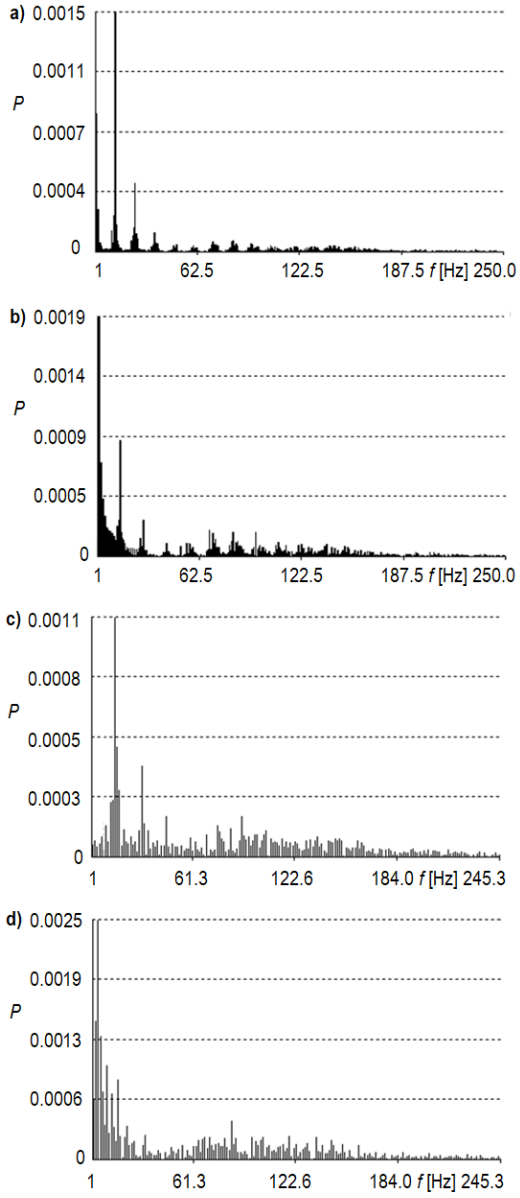

Fig. 5. Fourier power spectrums for time series of pressure changes in gas supply systems for left and right nozzles: (a) q = 0.0260 L/min, left nozzle; (b) q = 0.0260 L/min, right nozzle; (c) q = 0.0657 L/min, left nozzle and (d) q = 0.0657 L/min, right nozzle

In Fig. 5, the power spectrums for pressure changes in the right and left nozzles were calculated separately. In Fig. 5a and c, the dominant frequency of pressure fluctuations indicates the bubble departure frequency (13.59 Hz – Fig. 5a; 16.14 Hz – Fig. 5c). Fig 5b and d illustrates that the dominant frequency of pressure fluctuations are connected with the long-term pressure fluctuations (connected with the disappearance of alternative bubble departures). The frequencies of the bubble departures are evaluated using the 'second dominant frequency' (12.62 Hz – Fig. 5b; 15.95 Hz – Fig. 5d).

An increase in air volume flow rate diminishes the differences between frequencies of bubble departures from the left and right nozzle in comparison with the case presented in Fig. 5a and b.

3.2 Attractor reconstructions

The attractor reconstruction was carried out using the stroboscope coordination (Schuster, 1993). This method calculates subsequent coordinates of attractor points based on the samples between which the distance is equal to time delay. The time delay influences the attractor shape. In the recent article, the time delay was estimated using a method based on the analysis of autocorrelation function (Ca). The time delay (τ) was calculated using the following criterion (Grassberger and Procaccia, 1983):

$$C_a(\tau) \sim 0.5 C_a(0) \tag{3}$$

where C_a is defined as (Schuster, 1993):

$$C_a(\tau) = \frac{1}{N}\sum_{i=0}^{n} x_i x_{i+\tau} \tag{4}$$

where: N is the number of samples and x_i is the value of i sample.

The function (4) is constant or oscillates when τ increases for data generated by the periodical system (Schuster, 1993). In the case of chaotic data, the value of the autocorrelation function rapidly decreases when τ increases.

The attractor reconstruction was carried out using the stroboscope coordination (Schuster, 1993). This method calculates subsequent coordinates of attractor points based on the samples between which the distance is equal to time delay. The time delay influences the attractor shape. In the recent article, the time delay was estimated using a method based on the analysis of autocorrelation function (C_a). The time delay (τ) was calculated using the following criterion (Grassberger and Procaccia, 1983):

$$C_a(\tau) \sim 0.5 C_a(0) \tag{3}$$

where C_a is defined as (Schuster, 1993):

$$C_a(\tau) = \frac{1}{N}\sum_{i=0}^{n} x_i x_{i+\tau} \tag{4}$$

where N is the number of samples and x_i is the value of i sample.

The function (4) is constant or oscillates when τ increases for data generated by the periodical system (Schuster, 1993). In the case of chaotic data, the value of the autocorrelation function rapidly decreases when τ increases.

In Fig. 6, the autocorrelation functions for time series of pressure fluctuation in gas supply systems for the left and right nozzles are presented.

Considering the air volume flow rate q = 0.0260 L/min (Fig. 6a and b), the time delay (τ) is equal to 17 and 41 for the left nozzle and right nozzle, respectively. When the air volume flow rate is equal to q = 0.0657 L/min, the time delay (τ) is equal to 11 for the left nozzle and 28 for the right nozzle.

DOI 10.2478/ama-2019-0021

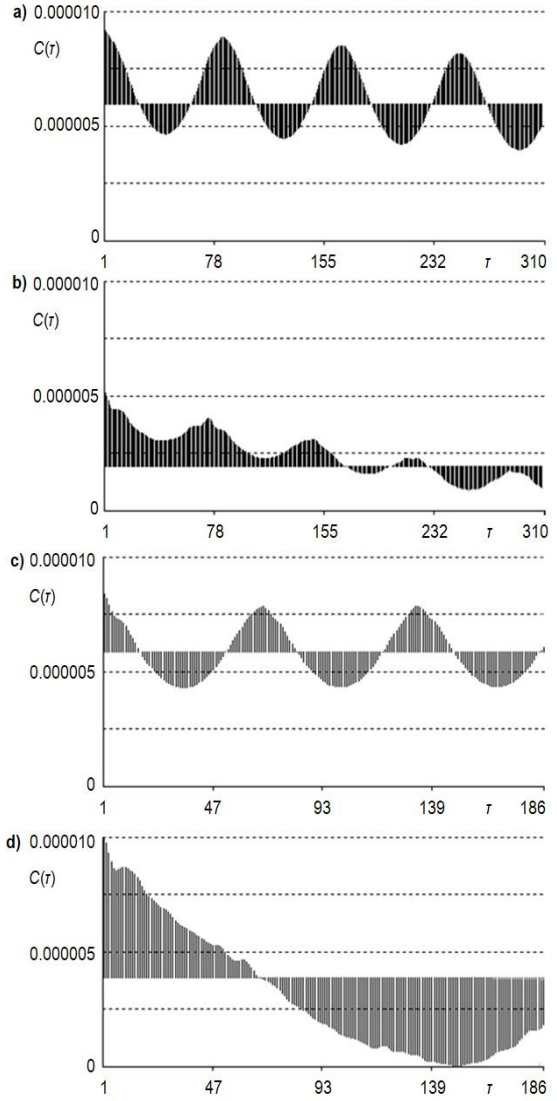

Fig. 6. Autocorrelation functions for time series of pressure fluctuation in gas supply system for the left and right nozzles: (a) q = 0.0260 L/min, left nozzle; (b) q = 0.0260 L/min, right nozzle; (c) q = 0.0657 L/min, left nozzle and (d) q = 0.0657 L/min, right nozzle

The values of time delay were used to form the reconstructions of three-dimensional (3D) attractors. The 3D attractor reconstructions for time series of pressure changes are presented in Fig. 7.

For the air volume flow rates q = 0.0260 L/min – left nozzle (Fig. 7a) and q = 0.0657 L/min – left nozzle (Fig. 7c), the reconstructed trajectories of 3D attractors form a torus. It indicates that the bubble departures are quasiperiodic. The shapes of trajectories presented in Fig. 7b and d do not form a torus. According to this observation, a chaotic character of bubble departures is assumed.

The correlation dimension, D_2, is one of the characteristics of the attractor. In the recent article, the correlation dimension was calculated using Grassberger–Procaccia algorithm (Grassberger and Procaccia, 1983), where:

$$D_2 = \lim_{r\to 0} \frac{1}{\ln r} \ln \sum_i p_i^2 \tag{5}$$

$$\sum_i p_i^2 \approx \lim_{N\to\infty} \frac{1}{N^2} \sum_{i,j} \Theta\left(r - \left|\overrightarrow{x_i} - \overrightarrow{x_j}\right|\right) \tag{6}$$

where: $\Theta(x)$ is Heaviside's step function, p is the probability, r is distance, x_i is the time series of pressure fluctuations in the left nozzle and x_j is the time series of pressure fluctuations in the right nozzle.

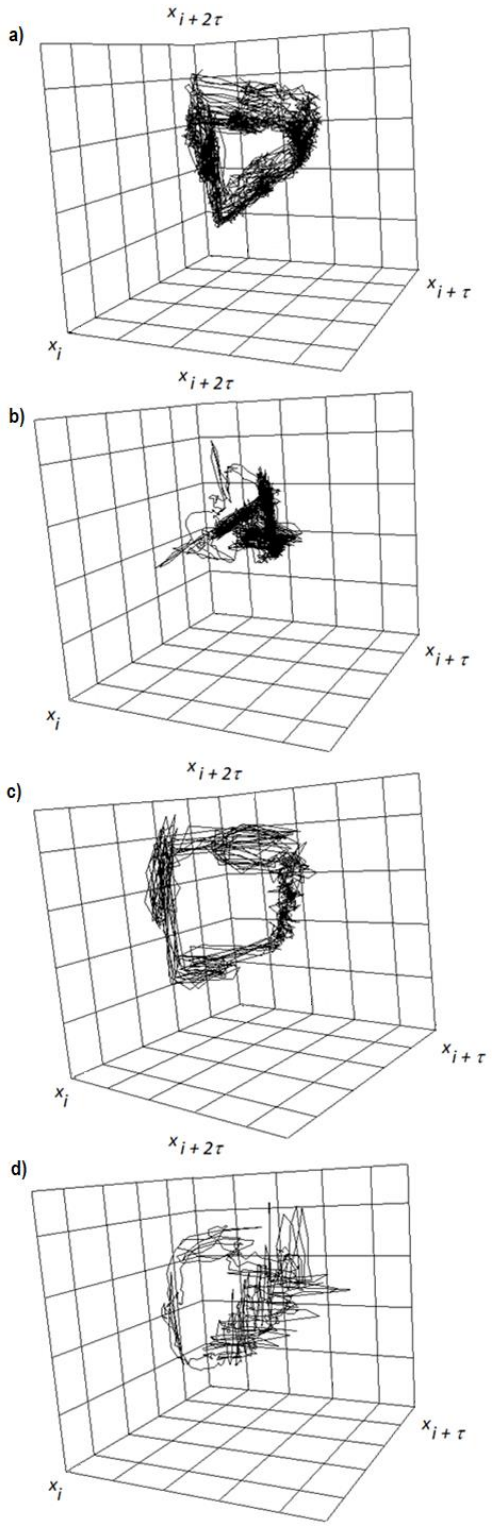

Fig. 7. The three-dimensional attractor reconstructions for time series of pressure changes in gas supply system for left and right nozzles: (a) q = 0.0260 L/min, left nozzle; (b) q = 0.0260 L/min, right nozzle; (c) q = 0.0657 L/min, left nozzle and (d) q = 0.0657 L/min, right nozzle

DOI 10.2478/ama-2019-0021

The graphs of log(*C*) function of log(*r*) for the analysed time series were shown in Fig. 8.

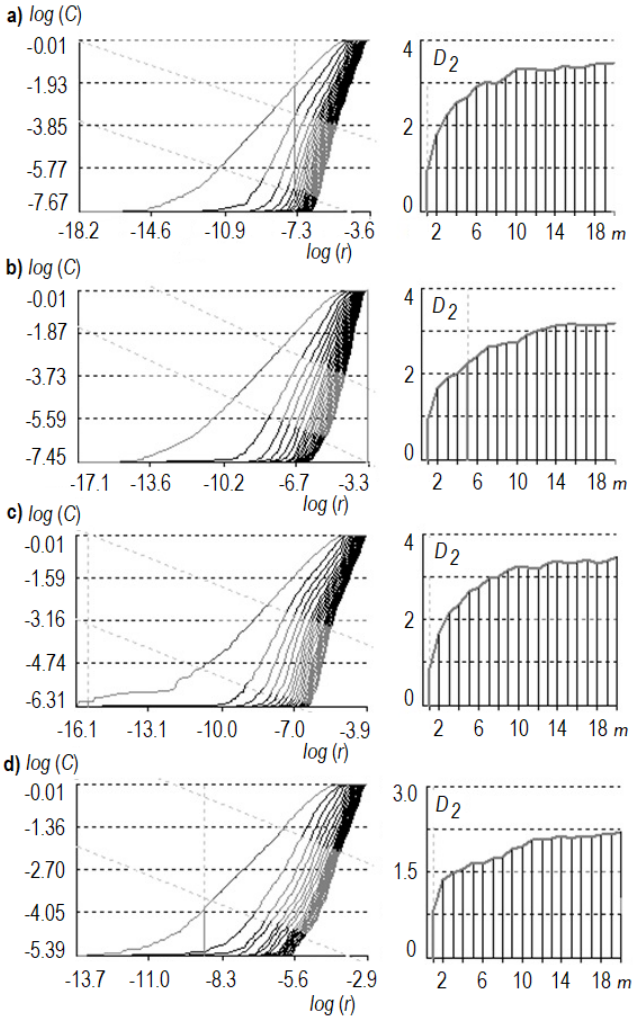

Fig. 8. Graphs of log(C) versus log(r) and correlation dimensions for time series of pressure changes in gas supply systems for left and right nozzles: (a) q = 0.0260 L/min, left nozzle; (b) q = 0.0260 L/min, right nozzle; (c) q = 0.0657 L/min, left nozzle and (d) q = 0.0657 L/min, right nozzle

The correlation dimension D_2 is equal to 4 for both analysed nozzles when the air volume flow rate is q = 0.0260 L/min (Fig. 8a and b). For the air volume flow rate q = 0.0657 L/min, D_2 is 4 (Fig. 8c) and 3 (Fig. 8d) for the left nozzle and right nozzle, respectively.

3.3 Largest Lyapunov exponent

The largest Lyapunov exponent is helpful to identify the intensity of chaotic changes of analysed time series. The largest Lyapunov exponent is calculated according to the following formula (Wolf et al., 1985):

$$\lambda = \sum_{j=1}^{m} \log_2 \frac{d(x_{j+1})}{d(x_j)} \tag{7}$$

In the process of Largest Lyapunov exponent estimation, two points of the attractor (reconstructed for time series) immersed in m-dimensional space are selected. The distance between these points is marked as $d(x_j)$ and is calculated after one orbiting period. After a certain time, the distance between the selected points is calculated again. This distance is denoted as $d(x_{j+1})$.
The values of the largest Lyapunov exponent for analysed time series are shown in Fig. 9.

The value of λ is evaluated as the last value of the curve in the graph (Fig. 9). When the air volume flow rate q = 0.0260 L/min, then the largest Lyapunov value calculated is 31.35 (Fig. 9a) and 58.84 (Fig. 9b) for the left and right nozzles, respectively. For the value of air volume flow rate q = 0.0657 L/min, the largest Lyapunov exponent equals to 39.20 and 90.07 for the left and right nozzles, respectively (Fig. 9c and d).

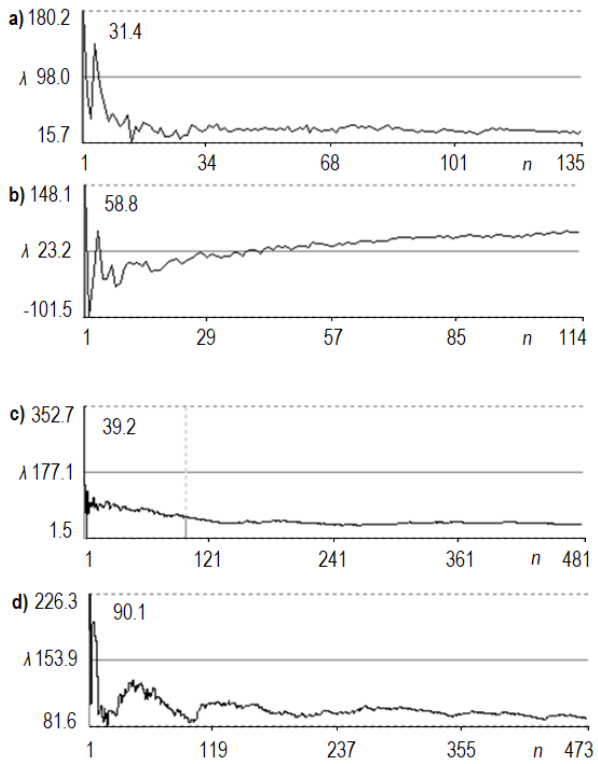

Fig. 9. The largest Lyapunov exponent for time series of pressure changes in gas supply systems for left and right nozzles: (a) q = 0.0260 L/min, left nozzle; (b) q = 0.0260 L/min, right nozzle; (c) q = 0.0657 L/min, left nozzle and (d) q = 0.0657 L/min, right nozzle

3.4 RP analysis

In order to determine the repeatability of the pressure changes in the gas supply system in the subsequent cycles of bubble departures, RPs were used. RP is the technique of visualisation of the recurrence of states in m-dimensional phase space. The recurrence of a state at the time i at a different time j is marked with black dots in the plot. In the RP, vertical and horizontal axes represent time. The RP is defined as (Marwan et al., 2007):

$$R_{i,j} = \Theta\left(\varepsilon_i - \left\|x_i - x_j\right\|\right), \quad x_i \in \Re^n, \quad i,j = 1 \ldots N \tag{8}$$

where N is the number of considered states x_i, ε is the threshold distance for states which are identified as the same, $\|\cdot\|$ is a norm and $\Theta(\cdot)$ is the Heaviside function.

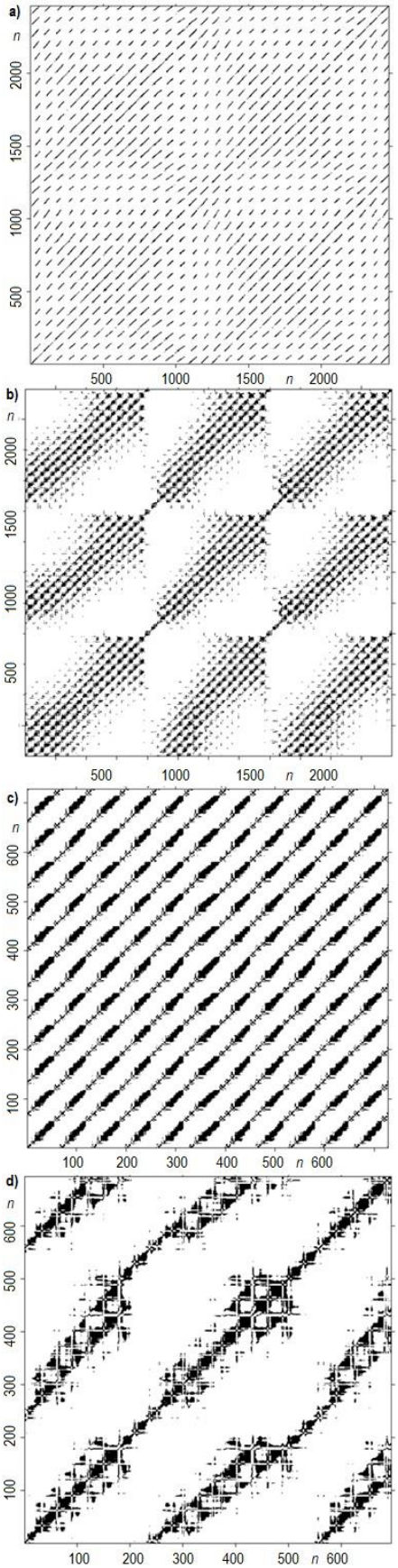

Fig. 10. The recurrence plots for time series of pressure changes in gas supply systems for left and right nozzles: (a) q = 0.0260 L/min, left nozzle; (b) q = 0.0260 L/min, right nozzle; (c) q = 0.0657 L/min, left nozzle and (d) q = 0.0657 L/min, right nozzle

In Fig. 10, the RPs for analysed time series are presented. RPs were calculated using the CRP toolbox implemented by Marwan (2019) in Matlab. Periodic oscillations of pressure create the parallel diagonal lines on RP. The distance between diagonal lines indicates the time between subsequent bubble departures. The RP shown in Fig. 10a and c proves that bubbles from the left nozzle departed almost periodically. The gaps between diagonal lines are created by small chaotic pressure fluctuations occurred after the bubble departures. The RP presented in Fig. 10b and d indicates that pressure fluctuations have a chaotic character (in the right nozzles).

Quantity analysis of RP presented in Fig. 10 was calculated using the following coefficients:

- Recurrence rate (*RR*) determines the percentage of recurrence points in the RP:

$$RR = \frac{1}{N^2} sum_{i,j=1}^{N} R_{i,j}$$

- Averaged diagonal line length:

$$L = \frac{\sum_{l=l_{min}}^{N} lP(l)}{\sum_{l=1}^{N} P(l)}$$

- Trapping time is the average length of the vertical lines:

$$TT = \frac{\sum_{v=v_{min}}^{N} vP(v)}{\sum_{v=v_{min}}^{N} vP(v)}$$

where N is the number of points on the phase space trajectory, $P(l)$ and $P(v)$ denote histogram of the line lengths of diagonal and vertical lines, respectively.

The obtained values of coefficients are presented in Table 1.

Tab. 1. The values of recurrence rate (*RR*), averaged diagonal line length (*L*) and trapping time (*TT*)

q (L/min)	*Nozzle*	*RR*	*L*	*TT*
0.0260	Left	0.14	9.73	11.09
0.0260	Right	0.12	5.37	7.26
0.0657	Left	0.18	8.29	7.73
0.0657	Right	0.12	4.88	6.43

The obtained values of *RR* and *L* coefficients indicate that pressure fluctuations in the left nozzle are more predictable in comparison with pressure fluctuations in the right nozzle. It is observed for both analysed air volume flow rates. The values of *TT* coefficient point that the dominant frequency of the attractors' trajectory in four-dimensional space is lower in the left nozzle than in the right nozzle. The mentioned differences are greater for lower air volume flow rate. The results of analysis confirms that the frequencies of bubble departures from both nozzles become similar when the air volume flow rate is increased.

4. CONCLUSIONS

In this article, the synchronisation of bubble departures from twin nozzles in engine oils was analysed. In the experiment, the alternative and simultaneous bubble departures were observed.

It has been shown that for the alternative bubble departures, the correlation of air pressure fluctuations in the neighbouring nozzle increases continuously. Finally, it leads to the disappearance of alternative bubble departures. The mentioned process is repeated in a cyclic way.

Non-linear analysis of bubble departure synchronisations proves that the way of bubble departures from two neighbouring nozzles does not depend simply on the character of pressure fluctuations in the nozzle air supply systems. Chaotic changes of the air pressure oscillations do not always determine the chaotic character of bubble departures. Such situations are observed for alternative bubble departures in engine oil. The obtained results confirm the conclusions presented in the article by Vazquez et al. (2010).

REFERENCES

1. **Dzienis P., Mosdorf R.** (2014), Stability of periodic bubble departures at a low frequency, *Chemical Engineering Science,*109, 171-182.
2. **Femat R., Ramirez J.A., Soria A.** (1998), Chaotic flow structure in a vertical bubble column, *Physics Letters A*,248 (1), 67–79.
3. **Grassberger P., and Procaccia I.** (1983), Measuring the strangeness of strange attractors, *Physica - D*,9, 189–208.
4. **Kazakis N.A., Mouza A.A., Paras S.V.** (2008), Coalescence during bubble formation at two neighbouring pores: an experimental study in microscopic scale, *Chemical Engineering Science,*63, 5160–5178
5. **Lavensona D.M., Kelkara A.V., Daniel A. B., Mohammad S.A., Koubab G., Aicheleb C.P.** (2016), Gas evolution rates – A critical uncertainty in challenged gas-liquid separations, *Journal of Petroleum Science and Engineering*, 147, 816-828
6. **Legendre D., Magnaudet J., Mougin G.** (2003), Hydrodynamic interactions between two spherical bubbles rising side by side in a viscous liquid,*Journal of Fluid Mechanics,*497, 133–166.
7. **Marwan N.**(2019), Cross Recurrence Plot Toolbox for Matlab, Ver. 5.15, Release 28.10, http://tocsy.pik-potsdam.de.
8. **Marwan N., Romano M. C., Thiel M., Kurths J.** (2007),Recurrence Plots for the Analysis of Complex Systems,*Physics Reports*, 438, 237 – 329.
9. **Mosdorf R., Dzienis P., Litak G.** (2017), The loss of synchronization between air pressure fluctuations and liquid flow inside the nozzle during the chaotic bubble departures, *Meccanica*, 52, 2641–2654
10. **Mosdorf R., Wyszkowski T.** (2011), Experimental investigations of deterministic chaos appearance in bubbling flow, *International Journal of Heat and Mass Transfer,* 54, 5060–5069.
11. **Mosdorf R., Wyszkowski T.** (2013), Self-organising structure of bubbles departures, *International Journal of Heat and Mass Transfer*, 61, 277–286.
12. **Sanada T., Sato A., Shirota M.T., Watanabe M.** (2009), Motion and coalescence of a pair of bubbles rising side by side, *Chemical Engineering Science*, 64, 2659-2671.
13. **Schuster H.G.** (1993), *Deterministic Chaos. An Introduction*, PWN, Warszawa (in Polish).
14. **Snabre P., Magnifotcham F.** (1997), Formation and rise of a bubble stream in viscous liquid,*European Physical Journal B*, 4, 369-377.
15. **Torrence C., Compo G. P.** (1998), A practical guide to wavelet analysis, *Bulletin of the American Meteorological Society*,79, 61-78.
16. **Vazquez A., Leifer I., Sanchez R.M.** (2010), Consideration of the dynamic forces during bubble growth in a capillary tube, *Chemical Engineering Science*, 65, 4046–4054.
17. **Wolf A., Swift J.B., Swinney H.L., Vastano J.A.** (1985), Determining Lyapunov Exponent from a Time series, *Physica-D*, 16, 285–317.

This work has been accomplished under the research project No. UMO-2011/03/N/ST8/04079 financed by the Polish National Science Center.

DESIGN OF AN OPTIMAL FUZZY CONTROLLER OF AN UNDER-ACTUATED MANIPULATOR BASED ON TEACHING-LEARNING-BASED OPTIMIZATION

Mohammad Javad MAHMOODABADI,[*] Amineh YAZDIZADEH BAGHINI[*]

[*]Department of Mechanical Engineering, Sirjan University of Technology, Sirjan, P.O. Box: 78185-439, Iran

mahmoodabadi@sirjantech.ac.ir, amineh.yazdizadeh@yahoo.com

received 24 April 2019, revised 20 September 2019, accepted 24 September 2019

Abstract: In this paper, an optimal fuzzy controller based on the Teaching-Learning-Based Optimization (TLBO) algorithm has been presented for the stabilization of a two-link planar horizontal under-actuated manipulator with two revolute (2R) joints. For the considered fuzzy control method, a singleton fuzzifier, a centre average defuzzifier and a product inference engine have been used. The TLBO algorithm has been implemented for searching the optimum parameters of the fuzzy controller with consideration of time integral of the absolute error of the state variables as the objective function. The proposed control method has been utilized for the 2R under-actuated manipulator with the second passive joint wherein the model moves in the horizontal plane and friction forces have been considered. Simulation results of the offered control method have been illustrated for the stabilization of the considered robot system. Moreover, for different initial conditions, the effectiveness and the robustness of the mentioned strategy have been challenged.

Keywords: Optimal controller, Fuzzy control, Teaching-learning-based optimization, Under-actuated system, 2R planar horizontal manipulator

1. INTRODUCTION

In the last two decades, many researchers have shown interest in the control and stabilization of under-actuated manipulators and it has remained an open problem till now. A system with lower number of control inputs than degrees of freedom is said to be an under-actuated one. Utilizing the under-actuated systems is economical because of energy saving, reduced cost and weight, although they have the disadvantage that the control of these systems is more complicate. Furthermore, if one of actuators of a fully actuated system fails, it is convenient to have a controller for the under-actuated system in this situation.

A popular and powerful solution to attack this problem is utilizing control methods based on fuzzy logic. These techniques are implemented to design stabilizers according to the synthesis of fuzzy IF-THEN rules heuristically determined by the knowledge and experience of an expert. There are variant versions of the fuzzy control methods based on the kinds of fuzzifiers, the defuzzifiers and the inference engines applied by researchers. For instance, in the field of fuzzy control of under-actuated systems, Jianiang et al. (2001) presented a new fuzzy controller based on a sum-product inference engine system for stabilization of a ball and beam system. Ho et al. (2007) proposed a stable adaptive fuzzy-based tracking control for a robot manipulator. Karimi et al. (2011) introduced a new type-2 fuzzy logic controller to handle a nonlinear inverted pendulum system. Mahmoodabadi et al. (2016) implemented an optimal fuzzy technique to stabilize two nonlinear systems. Mahmoodabadi and Danesh (2017) applied a fuzzy approach based on the gravitational search algorithm to set the state variables of a ball and beam system. Caoyang et al. (2017) introduced nonlinear guidance and fuzzy control for three-dimensional path following of an autonomous underwater vehicle. Naghibi et al. (2017) presented a fuzzy controller with integrator for control of manipulators. Nguyen et al. (2018) designed and experimented fuzzy steering control for autonomous vehicles' saturation. Lin et al. (2018) exhibited the performance of the adaptive fuzzy output feedback stabilization control for the surface vessel. Zakeri et al. (2019) introduced an optimal interval type-2 fuzzy fractional order super twisting algorithm for stabilization of dynamical systems. Deng et al. (2019) displayed event-triggered robust fuzzy path following control for ships with input saturation. Wang et al. (2019) represented fuzzy unknown observer-based robust adaptive path following the control of underactuated surface vehicles subject to multiple unknowns. Vahidi-Moghaddam et al. (2019) organized disturbance-observer-based fuzzy terminal sliding mode control for uncertain nonlinear systems.

On the other hand, the synthesis of control policies has been presented as optimization problems of certain performance measures of the controlled systems. A very effective means of solving such optimum controller design problems is utilizing evolutionary algorithms such as Teaching-Learning-Based Optimization (TLBO). This algorithm as a new nature-inspired optimization algorithm works based on the influence of a teacher on its learners. It is also a population-based method and uses a population of solutions to find the optimum global solution. At first, Rao et al. (2011) showed the better performance of TLBO over other nature-inspired optimization methods for the constrained benchmark functions and mechanical design problems. Furthermore, Rao et al. (2012) proposed it to find a solution for continuous non-linear large scale optimization problems. Khoban (2014) used TLBO for optimum design of a feedback linearization controller to achieve the best trajectory tracking for non-holonomic wheeled mobile robots.

This research tries to present an optimal fuzzy controller based on a TLBO algorithm for stabilization of a two-link under-actuated manipulator. For this fuzzy control method, a singleton fuzzifier, a centre average defuzzifier and a product inference engine have been used. The TLBO algorithm has been designed for searching the optimum design variables of the fuzzy controller. The proposed control method has been utilized for the 2R under-actuated manipulator with a second passive joint wherein the model moves in the horizontal plane and the friction forces have been considered.

The rest of the paper is organized as follows. The mathematical model of the considered under actuated manipulator is explained in Section 2. The descriptions of the considered fuzzy system and the proposed fuzzy controller are stated in Sections 3 and 4, respectively. Moreover, Section 4 briefly introduces the TLBO algorithm, design variables and objective functions. The introduced fuzzy controller is implemented on the 2R planar under-actuated manipulator in Section 6. Furthermore, the optimization of the control parameters by the TLBO algorithm and the simulation results are included in this section. Finally, the conclusion is made in Section 7.

2. THE MATHEMATICAL MODEL OF THE UNDER-ACTUATED MANIPULATOR

The configuration of the considered manipulator is illustrated in Fig. 1, which has two degrees of freedom with revolute joints and two links that move on the frictional horizontal plane. The first revolute joint is active whereas the second one is considered as a passive pin.

If the generalized coordinates $\mathrm{q_i}$, $\mathrm{i} = 1{,}2$ are regarded as the joint angles, then the dynamic model of the system can be written as follow (Spong et al., 2005).

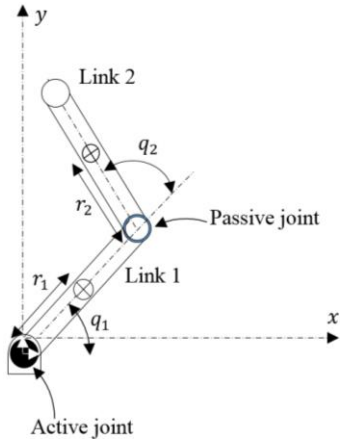

Fig 1. A schematic of the 2R planar under-actuated manipulator with the second passive joint

$$M(q)\ddot{q} + h(q,\dot{q}) = \tau \tag{1}$$

where, $\dot{\mathrm{q}}$ is the vector of the generalized velocities, $\ddot{\mathrm{q}}$ is the vector of the generalized accelerations, $\mathrm{M(q)} \in \mathrm{R}^{2\times 2}$ denotes the inertia matrix and $\mathrm{h}(\dot{\mathrm{q}}, \ddot{\mathrm{q}})$ contains the centrifugal, Coriolis and possibly gravitational terms; although here, the gravitational terms have not been considered because the manipulator has been assumed to move on the horizontal plane.

In order to simplify the motion equations, the following constant parameters are defined.

$$z_1 = m_1 r_1^2 + m_2 l_1^2 + I_1 \tag{2}$$

$$z_2 = m_2 r_2^2 + I_2 \tag{3}$$

$$z_3 = m_2 l_1 r_2 \tag{4}$$

where, $\mathrm{m_1}$ and $\mathrm{m_2}$ illustrate the link masses, $\mathrm{l_1}$ and $\mathrm{l_2}$ show the link lengths, $\mathrm{I_1}$ and $\mathrm{I_2}$ are the moments of inertia, and $\mathrm{r_1}$ and $\mathrm{r_2}$ depict the centers of the masses. Hence, the elements of $\mathrm{M(q)}$ and $\mathrm{h(q,\dot{q})}$ are considered as follow:

$$m_{11} = z_1 + z_2 + 2z_3 \operatorname{Cos} q_2 \tag{5}$$

$$m_{12} = z_2 + z_3 \operatorname{Cos} q_2 \tag{6}$$

$$m_{21} = m_{12} \tag{7}$$

$$m_{22} = z_2 \tag{8}$$

$$h_1 = -z_3(2\dot{q}_1\dot{q}_2 + \dot{q}_2^2) \operatorname{Sin} q_2 \tag{9}$$

$$h_2 = z_3\dot{q}_1^2 \operatorname{Sin} q_2 \tag{10}$$

It must be mentioned that both the frictions (Coulomb and viscous) are considered for the passive joint. The viscous friction $\mathrm{F_V}$ is defined as proportional to the velocity of the second joint.

$$F_V = b\dot{q} \tag{11}$$

where, b is a viscous friction constant. The Coulomb friction $\mathrm{F_c}$ is regarded as constant with a sign dependence on the joint velocity and is given by:

$$F_c = SGN(\dot{q})\, c \tag{12}$$

where, c is the Coulomb friction constant. In order to eliminate the chattering phenomena caused by the sign function, it will be replaced by the following saturation function.

$$sat(\dot{q}) = \begin{cases} 1 & \dot{q} > k \\ -1 & \dot{q} < -k \\ \dot{q} & -k < \dot{q} < k \end{cases} \tag{13}$$

where, k is a positive constant; and here, regarded as k = 0.01. Therefore, the equations of motion can be formulated as follows (Spong et al., 2005).

$$m_{11}\ddot{q}_1 + m_{12}\ddot{q}_2 + h_1 = \tau - sat(\dot{q}_1)c_1 - b_1\dot{q}_1 \tag{14}$$

$$m_{21}\ddot{q}_1 + m_{22}\ddot{q}_2 + h_2 = -sat(\dot{q}_2)c_2 - b_2\dot{q}_2 \tag{15}$$

Moreover, the state-space equations are written as follows:

$$\begin{bmatrix}\dot{y}_1\\ \dot{y}_2\\ \dot{y}_3\\ \dot{y}_4\end{bmatrix} = \begin{bmatrix}0 & 1 & 0 & 0\\ 0 & -\frac{m_{12}}{m_{22}}b_1 & 0 & b_2\\ 0 & 0 & 0 & 1\\ 0 & \frac{m_{12}}{m_{11}}b_1 & 0 & -b_2\end{bmatrix}\begin{bmatrix}y_1\\ y_2\\ y_3\\ y_4\end{bmatrix} + \begin{bmatrix}0\\ \frac{1}{m_{11}-m_{12}^2/m_{22}}\\ 0\\ -\frac{m_{12}/m_{11}}{m_{22}-m_{12}^2/m_{11}}\end{bmatrix}\tau + \begin{bmatrix}0\\ \frac{c_1 sat(y_2)-h_1+m_{12}/m_{22}(c_2 sat(y_4)+h_2}{m_{11}-m_{12}^2/m_{22}}\\ 0\\ \frac{-c_2 sat(y_4)-h_2-m_{12}/m_{11}(-c_1 sat(y_2)-h_1)}{m_{22}-m_{12}^2/m_{11}}\end{bmatrix} \tag{16}$$

where, $[y_1, y_2, y_3, y_4]$ are the state variables corresponding to $[q_1, \dot{q}_1, q_2, \dot{q}_2]$, respectively. The considered control method proposes a suitable manipulated variable (U) to move the two links from the initial conditions to the desired positions. The relationship between U and torque τ is given as follows:

$$\tau = c_1\, sat(y_2) + b_1 y_2 + h_1 - \left(\frac{m_{12}}{m_{22}}(c_2\, sat(y_4) + b_2 y_4 + h_2)\right) + \left(m_{11} - \frac{m_{12}^2}{m_{22}}\right) U \quad (17)$$

3. THE CONSIDERED FUZZY SYSTEM AND PROPOSED FUZZY CONTROLLER

Three types of fuzzy systems are commonly implemented in the literature: (i) pure fuzzy systems, (ii) Takagi-Sugeno-Kang (TSK) fuzzy systems, and (iii) fuzzy systems with fuzzifier and defuzzifier. The main problem with the pure fuzzy system is that its inputs and outputs are fuzzy sets, whereas in engineering systems, the inputs and outputs are real-valued variables. To solve this problem, Takagi, Sugeno and Kang (Takagi and Sugeno, 1985; Sugeno and Kang, 1988) proposed another fuzzy system whose inputs and outputs are real-valued variables. The main problems with the Takagi-Sugeno-Kang fuzzy system are: (i) its THEN part is a mathematical formula, and therefore, may not provide a natural framework to represent human knowledge, and (ii) there is not much freedom left to apply different principles in fuzzy logic. To elucidate these drawbacks, the third type of fuzzy systems has been proposed with fuzzifier and defuzzifier (Wang, 1996).

In general, a third type fuzzy system consists of four parts; the fuzzifier, the fuzzy rule base, the inference engine and the defuzzifier (Wang, 1996). The used fuzzy system in this work implements the singleton fuzzifier, the product inference engine and the centre average defuzzifier as the following form:

$$\Psi_i = \frac{\Sigma_{l=1}^{m} \overline{\psi_l} \left(\Pi_{i=1}^{n} \mu_{A_i^l}(x_i)\right)}{\Sigma_{l=1}^{m} \Pi_{i=1}^{n} \mu_{A_i^l}(x_i)} \quad (18)$$

where, $\mu_{A_i^l}(x_i)$ is the membership function of the input linguistic variable x_i for the rule L-th. Because the calculations with triangular memberships are easy, this kind of functions are used here. The variable x_i is the normalized form of the state variable y_i. $\overline{\psi_l}$ presents the center of the output membership function $\mu_{B_i^l}$ for the rule L-th.

The fuzzy rules are separately regulated for each input item as follow:

$$rule - l \quad \{R_i^l : IF \;\; x_i = \mu_{A_i^l} \;\; THEN \;\; \Psi_i = \mu_{B_i^l}\}_{l=1}^{m} \quad (19)$$

that, R_i^l is the rule L-th. The normalized variable x_i is considered as an input item corresponding to the output variable Ψ_i.

In this paper, the following equation is proposed to calculate the manipulated variable U as the summation of the multiplication of the deviation and priority variables.

$$U = \sum_{i=1}^{n} D_i \times P_i \quad (20)$$

where, n is the number of the system states. D_i denotes the i-th deviation variable and P_i represents the priority variable.

Deviation fuzzy variable shows the deviation of state i-th from the corresponding desired state. In order to calculate D_i, as the first fuzzy variable, based on the fuzzy system introduced in Equation (18), Table 1 and Fig. 2 are regarded. Table 1 mentions the fuzzy rule base for the input items corresponding to the deviation fuzzy variables. The related triangular membership functions have been determined in Fig. 2 as negative (N), zero (Z) and positive (P). Based on Table 1 and Fig. 2, if the joint variables are located near the desired values, the control torque will be zero. Moreover, if the joint variables are less than the desired values, then a negative torque will rotate the arm counter clockwise. Inversely, if the angles are more than the desired values, a positive torque will rotate the arm clockwise.

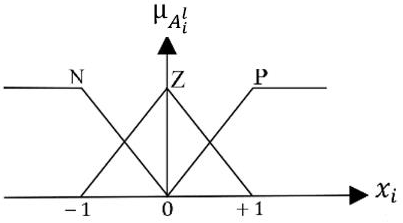

Fig. 2. Triangular membership functions for the input items corresponding to the deviation fuzzy variable D_i

Tab. 1. Fuzzy rule base corresponding to the deviation fuzzy variable D_i

x_i	$\bar{D}_l$
N	-1
Z	0
P	1

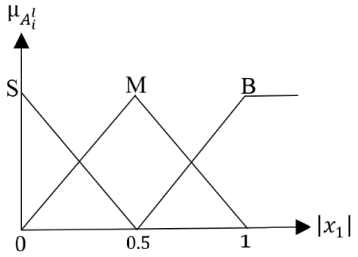

Fig. 3. Triangular membership functions for the input items corresponding to the second fuzzy variable S_i

Tab. 2. Fuzzy rule base corresponding to the second fuzzy variable S_i.

$\lvert x_1 \rvert$	$\bar{S}_l$
S	0
M	0.5
B	1

Priority variable represents the control priority of the considered joint. The priority variable P_i is proposed based on this fact that each state variable has its own effect on the control performance which may be different from others. For example, the stabilizing of the first joint angle and its angular velocity should be more important than those of the second joint when the first joint is not balanced. So, the first joint angular control takes more pri-

ority than the second joint. To express the role of each input item separately, the control priority P_i is defined as follows.

$$P_i = v_1^i + v_2^i \times S_i \; ; \; i = 1, 2, 3, 4. \tag{21}$$

where, v_1^i and v_2^i are the constant parameters. S_i, as the second fuzzy variable, is calculated based on the fuzzy system defined in Equation (18), Table 2 and Fig. 3. Table 2 shows the fuzzy rule base for the absolute of the normalized joint angles and the joint angular velocities. Based on Fig. 3 and Table 2, for example when the first angle is small, the control priority of this joint is zero but when this angle is big, it takes the maximum value.

Because the changes range of the inputs for the membership functions are $[-1; +1]$ or $[0; +1]$, the four state variables, i.e. the joint angles q_1 and q_2 and the joint angular velocities $\dot{q}_1$ and $\dot{q}_2$, have been normalized ($[x_1, x_2, x_3, x_4]$) with the scaling factors.

4. TEACHING-LEARNING-BASED OPTIMIZATION

For searching the optimum parameters of the fuzzy controller, the TLBO algorithm has been implemented. Teaching-learning-based optimization as a new nature-inspired optimization algorithm works based on the influence of a teacher on learners. It is also a population-based method and uses a population of solutions to find the global optimum solution. The wide application of TLBO in engineering fields is reflected in the improvement of the performance of distinguished systems, such as fatty acid methyl esters (Baghban et al., 2018), scheduling of projects (Kumar et al., 2018), plasma arc cutting (Patel et al., 2018) and power consumption optimization (Rao, 2019). The population is considered as a group of learners or a class of learners. The optimization process in TLBO is divided into two parts: the first part consists of the 'teacher phase' and the second part consists of the 'learner phase'. The first one means learning from the teacher and the second means learning from the interaction between learners (Rao et al., 2011 and 2012).

4.1. Teacher phase

In this phase, the teacher conveys information among the learners for the improvement of their mean result in the class. It is assumed that m and n are the number of subjects and students, respectively. Furthermore, Υ_m^{ji} denotes the mean result of the learners at subject $j = 1, 2, \ldots, m$ and teaching-learning sequence i. The supreme leaner of the entire population is assigned as the teacher because he/she is the most knowledgeable person (Υ_{best}).

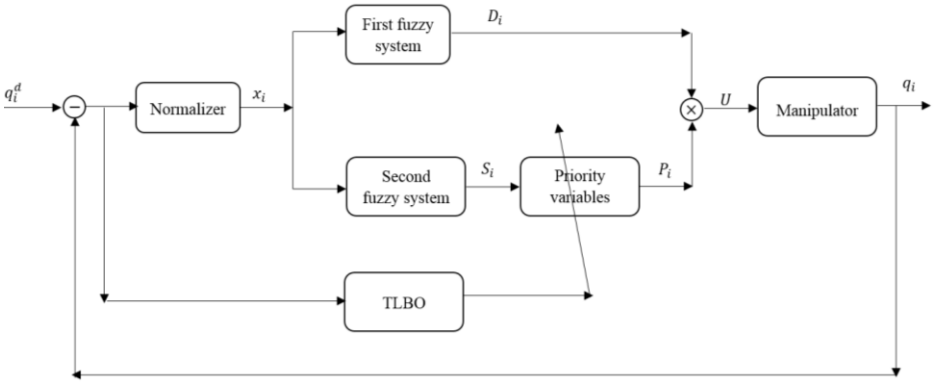

Fig. 4. Block diagram of the proposed optimal fuzzy controller of the under-actuated manipulator based on TLBO

A random weighted differential vector is formed in subject j for student k at sequence i as follows.

$$\Upsilon_{Dif}^{jki} = rand(\Upsilon_{best}^{jki} - \alpha \Upsilon_m^{ji}) \tag{22}$$

where, rand is a random number in range [0,1]. Moreover, α is the teaching factor and random takes the values of 1 or 2. A new learner is determined using the following equation.

$$\Upsilon_{new}^{jki} = \Upsilon_{old}^{jki} - \Upsilon_{Dif}^{jki} \tag{23}$$

where, Υ_{new}^{jki} represents the corresponding result of the improved learner and Υ_{old}^{jki} shows the grade achieved by each student in that class.

4.2. Learner phase

In this phase, the students might modify their knowledge via the mutual interaction. At first, two different student are selected, i.e. Υ_1^j and Υ_2^j. Then, based on the following conditions, the new situations would be obtained.

IF $\Upsilon_1^j < \Upsilon_2^j$ then $\Upsilon_{1_{new}}^j = \Upsilon_1^j + rand(\Upsilon_2^j - \Upsilon_1^j)$ (24)

IF $\Upsilon_2^j < \Upsilon_1^j$ then $\Upsilon_{1_{new}}^j = \Upsilon_1^j + rand(\Upsilon_1^j - \Upsilon_2^j)$ (25)

Moreover, $\Upsilon_{1_{new}}^j$ would be accepted in the condition that it has a more effective function value.

5. OPTIMAL FUZZY CONTROL OF THE UNDER-ACTUATED MANIPULATOR

Fig. 4 provides a graphical representation of the proposed strategy as a block diagram. This figure illustrates that the state variables (the joint angles and the joint angular velocities) relevant to the manipulator are compared with their desired values. Then, those are inputted into the normalizer block for normalization by the associated scaling factors. The fuzzy systems are utilizes to

produce deviation and priority variables. The summation of the production of these variables related to the joint angles and the joint angular velocities create the control effort. Finally, the TLBO algorithm described in the previous section is implemented for optimization of the constant parameters of the priority variables. The eight control parameters, i.e. $v_1^1, v_2^1, v_1^2, v_2^2, v_1^3, v_2^3, v_1^4, v_2^4$ have been regarded as the design variables and the summation of the integral of the absolute errors of the first and second joint angles has been considered as the cost function F as follows:

$$F = \int |q_1 - q_1^d| \, dt + \int |q_2 - q_2^d| dt \quad (26)$$

where, q_1^d and q_2^d respectively denote the desired values for the first and second joint angles.

6. RESULTS AND DISCUSSIONS

The manipulator parameters considered in this paper are as follows (Mahindrakar et al., 2006):
$z_1 = 0.725, \quad z_2 = 0.3179, z_3 = 0.3147, c_1 = 0.26,$
$c_2 = 0.116, b_1 = 0.6236, \; b_2 = 0.1223.$

Here, two cases with different initial values are considered; that for both, the desired values for the first and second joints are regarded as zero.

With considering an initial population 50 and maximum iterations 100, it is tried to optimize the cost function (26) and find the best parameters of the controller so that the system moves to the desired positions at a minimum possible time. Two different initial values:
$\left([q_1(0), \dot{q}_1(0), q_2(0), \dot{q}_2(0)] = \left[\frac{\pi}{5}, 0, \frac{\pi}{4}, 0\right] \; and \; \left[\frac{\pi}{2}, 0, 0, 0\right]\right)$
have been regarded, and their associate optimum values are listed Tables 4 and 5, respectively. The optimization graph of the first initial conditions illustrated in Fig. 5 shows that the population size and maximum iterations are well organized because the best cost has fixed after 42 iterations. The value of the best cost function in the first repetition equals 2.217 and in the last repetition, equals 2.061. The numerical values of the scaling factors obtained by a try and error process are as $[25°, 50°/s, 25°, 50°/s]$ for $[y_1, y_2, y_3, y_4] = [q_1, \dot{q_1}, q_2, \dot{q_2}]$, respectively.

It is obvious from Tables 4 and 5 that the summation of the two parameters for the first joint angle and the first joint angular velocity is larger than of those for the second joint. It is resulted that the first joint control takes more priority than the second joint control. The time responses of the first and second joint angles, joint angular velocities and control torque for the two initial values are depicted in Figs. 6–11. It is observable from these figures that all the state variables have converged to zero, and the complete stabilization have occurred.

Tab. 4. The optimum control parameters obtained by TLBO for the initial values $[q_1(0), \dot{q}_1(0), q_2(0), \dot{q}_2(0)] = \left[\frac{\pi}{5}, 0, \frac{\pi}{4}, 0\right]$

Input item	v_1^i	v_2^i
$i = 1$	0.2500	4.1000
$i = 2$	1.4000	3.0000
$i = 3$	0.5000	1.5044
$i = 4$	1.4000	0.9600

Tab. 5. The optimum control parameters obtained by TLBO for the initial values $[q_1(0), \dot{q}_1(0), q_2(0), \dot{q}_2(0)] = \left[\frac{\pi}{2}, 0, 0, 0\right]$

Input item	v_2^i	v_1^i
$i = 1$	0.10050	3.1002
$i = 2$	1.72820	1.9097
$i = 3$	0.19978	0.1299
$i = 4$	1.59450	0.9895

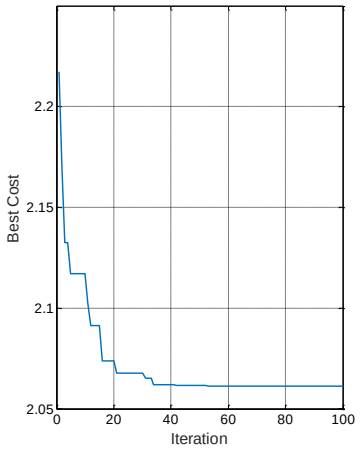

Fig. 5. The optimization trajectory for the fuzzy control of the under-actuated manipulator

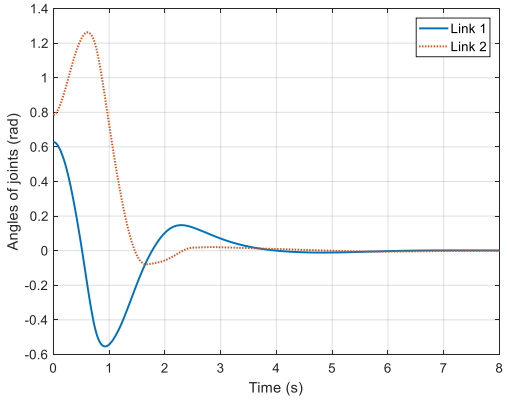

Fig. 6. Time trajectories of the first and second joint angles for initial values $[q_1(0), \dot{q}_1(0), q_2(0), \dot{q}_2(0)] = \left[\frac{\pi}{5}, 0, \frac{\pi}{4}, 0\right]$

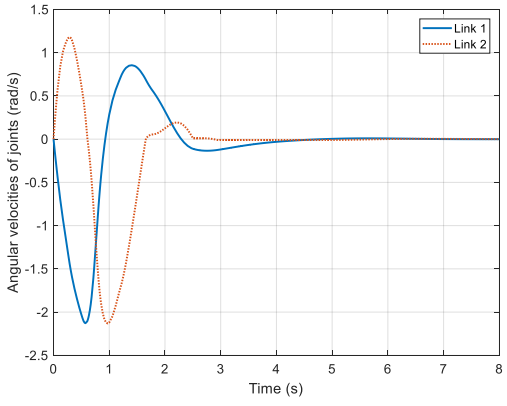

Fig. 7. Time trajectories of the first and second joint angular velocities for initial values $[q_1(0), \dot{q}_1(0), q_2(0), \dot{q}_2(0)] = \left[\frac{\pi}{5}, 0, \frac{\pi}{4}, 0\right]$

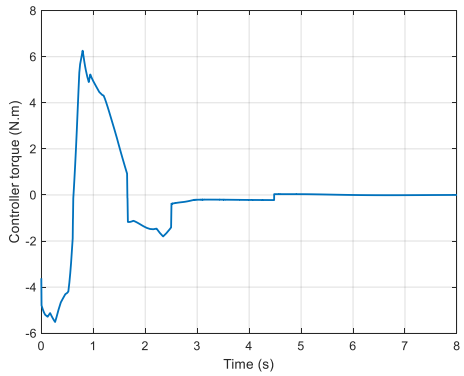

Fig. 8. Time trajectory of the actuator torque for initial values $[q_1(0), \dot{q}_1(0), q_2(0), \dot{q}_2(0)\ ] = \left[\frac{\pi}{5}, 0, \frac{\pi}{4}, 0\right]$

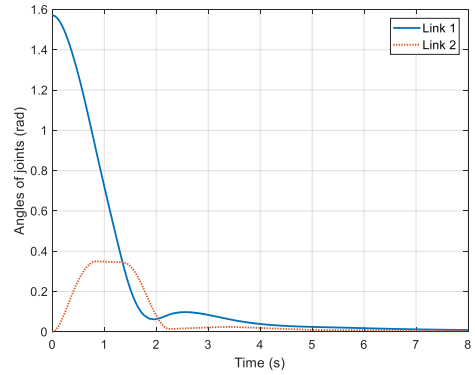

Fig. 9. Time trajectories of the first and second joint angles for initial values $[q_1(0), \dot{q}_1(0), q_2(0), \dot{q}_2(0)\ ] = \left[\frac{\pi}{2}, 0,0,0\right]$

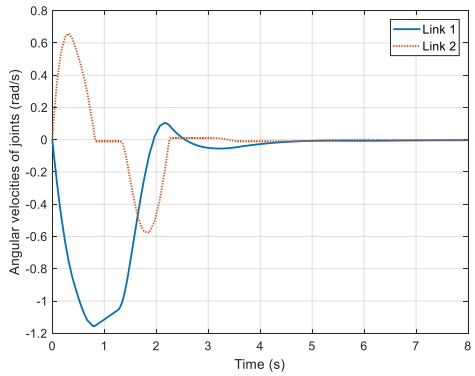

Fig. 10. Time trajectories of the first and second joint angular velocities for initial values $[q_1(0), \dot{q}_1(0), q_2(0), \dot{q}_2(0)\ ] = \left[\frac{\pi}{2}, 0,0,0\right]$

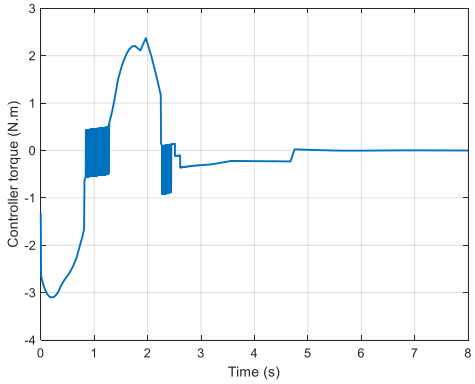

Fig. 11. Time trajectory of the actuator torque for initial values $[q_1(0), \dot{q}_1(0), q_2(0), \dot{q}_2(0)\ ] = \left[\frac{\pi}{2}, 0,0,0\right]$

7. CONCLUSION

In the present research, an optimal controller based on fuzzy rules was proposed as a general scheme to control a class of nonlinear underactuated systems. Teaching-Learning-Based Optimization (TLBO) was utilized to ascertain the optimal parameters of the proposed controller with regard to the design criteria. By utilizing the optimal design variables in the proposed controller, the performance of the controller was evaluated considering a two-link manipulator system. The results and analysis demonstrate the proper performance of the proposed controller in the aspects of stability and minimum tracking error. As a potential future study, making the controller online through using approaches, such as neural networks and moving least squares interpolation; ascertaining better optimal solutions for the parameters of the controller via other smart optimization algorithms; and considering different objective functions due to different design criteria can be regarded to extend this study in order to establish general approaches in the case of designing optimal fuzzy controllers.

REFERENCES

1. **Baghban A., Kardani M.N., Mohammadi A.H.** (2018), Improved estimation of Cetane number of fatty acid methyl esters (FAMEs) based biodiesels using TLBO-NN and PSO-NN models, *Fuel*, 232, 620–631.
2. **Craig J.J.** (1989), *Introduction to robotics. Mechanics and Control, Boston*, MA, USA, Addison-Wesley Longman Publishing Co, Inc.
3. **Deng Y., Zhang X., Im N., Zhang G., Zhang Q.** (2019), Event-triggered robust fuzzy path following control for underactuated ships with input saturation, *Ocean Engineering*, 186(1), 106122.
4. **He G.P., Wang Z.L., Zhang J., Geng Z.Y.** (2014), *Characteristics analysis and stabilization of a planar 2R underactuated manipulator*, Robotica, Cambridge University Press, 1–17.
5. **Ho H.F., Wong Y.K., Rad A.B.** (2007), Robust fuzzy tracking control for robotic manipulator, *IFSA World Congress and 20th NAFIPS International Conference*, 801–816.
6. **Karimi M., Safarinejadian B.** (2011), On-line control of the inverted pendulum with type-2 fuzzy logic controller, *2nd International Conference on Control, Instrumentation and Automation (ICCIA)*, 429–433.
7. **Khooban M.H.** (2014), Design an intelligent proportional-derivative (PD) feedback linearization control for nonholonomic-wheeled mobile robot, *Journal of Intelligent & Fuzzy Systems*, 26, 1833–1843.
8. **Kumar M., Mittal M.L., Soni G., Joshi D.** (2018), A hybrid TLBO-TS algorithm for integrated selection and scheduling of projects, *Computers & Industrial Engineering*, 119, 121–130.
9. **Lim C.M., Hiyama T.** (1991), Application of fuzzy logic control to a manipulator, *IEEE Transactions on Robotics and Automation* I, 5, 688–691.
10. **Lin X., Nie J., Jiao Y., Liang K., Li H.** (2018), Adaptive fuzzy output feedback stabilization control for the underactuated surface vessel, *Applied Ocean Research*, 74(1), 40–48.
11. **Ma X.J., Sun Z.Q., He Y.Y.** (1998), Analysis and design of fuzzy controller and fuzzy observer, *IEEE Transactions on Fuzzy Systems*, 6(1), 41–50.
12. **Mahindrakar A.D., Rao S., Banavar R.N.** (2006), Point-to-point control of a 2R planar horizontal underactuated manipulator, *Mechanism and Machine Theory*, 41, 838–844.
13. **Mahmoodabadi M.J., Danesh N.** (2017), Gravitational search algorithm based fuzzy control for a nonlinear ball and beam system, *Journal of Control and Decision*, 5(3), 229–240.
14. **Mahmoodabadi M.J., Mottaghi M.B.S., Mahmodinejad A.** (2016), Optimum design of fuzzy controllers for nonlinear systems using

multi-objective particle swarm optimization, *Journal of Vibration and Control*, 22(3), 769–783.
15. **Naghibi S.R., Pirmohamadi A.A., Moosavian S.A.A.** (2017), Fuzzy MTEJ controller with integrator for control of underactuated manipulators, *Robotics and Computer-Integrated Manufacturing*, 48(1), 93–101.
16. **Nguyen A.T., Sentouh C., Popieul J.C.** (2018), Fuzzy steering control for autonomous vehicles under actuator saturation: Design and experiments, *Journal of the Franklin Institute*, 355(18), 9374–9395.
17. **Patel P., Nakum B., Abhishek K., Kumar V.R., Kumar A.** (2018), Optimization of Surface Roughness in Plasma Arc Cutting of AISID2 Steel Using TLBO, *Materials Today: Proceedings*, 5 (9), 18927–18932.
18. **Rao K.V.** (2019), Power consumption optimization strategy in micro ball-end milling of D2 steel via TLBO coupled with 3D FEM simulation, *Measurement*, 132, 68–78.
19. **Rao R.V., Savsani V.J., Vakharia D.P.** (2011), Teaching-learning-based optimization: a novel method for constrained mechanical design optimization problems, *Computer-Aided Design*, 43, 303–315.
20. **Rao R.V., Savsani V.J., Vakharia D.P.** (2012), Teaching-learning-based optimization: an optimization method for continuous non-linear large scale problems, *Information Sciences*, 183(1), 1–12.
21. **Spong M.W., Hutchinson S., Vidyasagar M.** (2005), *Robot modeling and control*, John Wiley & Sons, Inc.
22. **Sugeno M., Kang G.T.** (1988), Structure identification of fuzzy model, *Fuzzy Sets and Systems*, 28(1), 15–33.
23. **Takagi T., Sugeno M.** (1985), Fuzzy identification of systems and its applications to modeling and control, *IEEE Transactions on Systems, Man and Cybernetics*, 15 (1), 116–132.
24. **Vahidi-Moghaddam A., Rajaei A., Ayati M.** (2019), Disturbance-observer-based fuzzy terminal sliding mode control for MIMO uncertain nonlinear systems, *Applied Mathematical Modelling*, 70(1), 109–127.
25. **Wang L.X.** (1996), *A Course in Fuzzy Systems and Control*, Upper Saddle River, United States Prentice-Hall International, Inc.
26. **Wang N., Sun Z., Yin J., Zou Z., Sud S.F.** (2019), Fuzzy unknown observer-based robust adaptive path following control of underactuated surface vehicles subject to multiple unknowns, *Ocean Engineering*, 176(1), 57–64.
27. **Yi J., Yubazaki N., Hirota K.** (2001), Stabilization control of ball and beam systems, *IFSA World Congress and 20th NAFIPS International Conference*, 2229–2234.
28. **Yoo B.K., Ham W.C.** (2000), Adaptive control of robot manipulator using fuzzy compensator, *IEEE Transactions on Fuzzy Systems*, 8(2), 186–199.
29. **Yu C., Xiang X., Lapierre L., Zhang Q.** (2017), Nonlinear guidance and fuzzy control for three-dimensional path following of an underactuated autonomous underwater vehicle, *Ocean Engineering*, 146(1), 457–467.
30. **Zakeri E., Moezi S.A., Eghtesad M.** (2019), Optimal interval type-2 fuzzy fractional order super twisting algorithm: A second order sliding mode controller for fully-actuated and under-actuated nonlinear systems, *ISA Transactions*, 85(1), 13–32.

sciendo

DOI 10.2478/ama-2019-0023

acta mechanica et automatica, vol.13 no.3 (2019)

SIMULATION AND ANALYSIS OF A TURBULENT FLOW AROUND A THREE-DIMENSIONAL OBSTACLE

Lamia BENAHMED*, Khaled ALIANE*

*Faculty of Technology, Department of Mechanical Engineering, University of Tlemcen, Bp 230, Chetouane Tlemcen, Algeria.

Benahmed_lamia91@yahoo.fr, kh_aliane@yahoo.fr

received 14 March 2019, revised 23 September, accepted 25 September

Abstract: The study of flow around obstacles is devised into three different positions: above the obstacle, upstream of the obstacle, and downstream of the latter. The behaviour of the fluid downstream of the obstacle is less known, and the physical and numerical modelling is being given the existence of recirculation zones with their complex behaviour. The purpose of the work presented below is to study the influence of the inclined form of the two upper peaks of a rectangular cube. A three-dimensional study was carried out using the ANSYS CFX calculation code. Turbulence models have been used to study the flow characteristics around the inclined obstacle. The time-averaged results of contours of velocity vectors <V>, cross-stream <v> and stream wise velocity <u> and streamlines were obtained by using K-ω shear -stress transport (SST), RANG K-ε and K-ε to model the turbulence, and the governing equations were solved using the finite volume method. The turbulence model K-ω SST has presented the best prediction of the flow characteristics for the obstacle among the investigated turbulence models in this work.

Key words: Turbulent flow, Obstacle, Finite volume, Turbulence models, ANSYS-CFX

1. INTRODUCTION

The generation of the turbulence within a channel was usually caused by the presence of baffles and obstacles. In the presence of obstacles, fluid flow, widely used in industry and application is extremely diverse. We can meet in the case of environmental problems related to the dispersion of pollutants through the cities and the effects of wind on buildings, ventilation road tunnel, the cooling fins of heat flares (Aliane et al., 2003), the baffles in heat exchangers or solar collectors, urban pipelines and so on. The study of the flow around obstacle may be the following two approaches. The digital approach is to discretise the governing equation of the flow by a digital method using different formulations (Hadjoui et al., 2003; Bitsuamiak et al., 2006). The experimental approach can be treated in two aspects; first is the qualitative where visualisation techniques are used to analyse the different nascent vortices within the flow (Sebbane et al., 2003). The second aspect is quantitative. For several years now, a large number of experimental and, more recently, numerical studies have concentrated on understanding complex flows around different profiled or not profiled obstacle models. This type of flow is generally found in many industrial applications, such as the cooling of electronic components (Saleha et al., 2015), atmospheric flows around buildings (Hainesa and Taylor, 2018), and fins of turbo machines. Several studies have been carried out on the application of flows around obstacles.

Hwang and Yang (2010) have carried out a numerical study on swirl (vortex) structures around a cube inside a canal. They found out that the number of vortices increased as the Reynolds number increased. Fillippini et al. (2005) investigated the case of the flow around cubes placed into a channel, using the large eddy simulation (LES) model. The results obtained showed that when the ratio S/H increases, the average drag coefficient augments for the second cube, while it remains approximately constant for the first one. Chang Lim et al. (2009) and Krajnovi'c and Davidson (2002) using the standard (LES) model provided a numerical simulation of the flow around a surface-mounted cube, placed in a turbulent boundary layer and comparing with experimentation. In the same approach, Yakhot et al. (2006) studied the turbulent flow around a bluff body. The immersed-boundary finite-volume method was introduced to carry out a direct numerical simulation. These same authors found out that the emergence of negative turbulence production in front of the cube can be used to explain the failure of some LES/RANS simulations in predicting the behaviour of flows around a surface-mounted cube. Becker et al. (2002) presented an experimental simulation using different aspect ratios in two different types of boundary layers to study the structure of the flow around three-dimensional obstacles. The experimental results showed that the flow structure around the obstacle depends on its aspect ratio, the angle of attack, Reynolds number and type of boundary layer. Aliane (2011) presented a numerical analysis of the turbulent flow of air inside a channel of rectangular section, with two types of obstacles: the first has a rectangular obstacle and another with a rounded upstream side having a radius of curvature equal to 0.2 times the height of the block. In the same approach, Rostane and Aliane (2015) conducted a three-dimensional study around two models of obstacles. The first one has a prismatic form, and the second one is prismatic and rounded downstream. The turbulence model k-ω shear-stress transport SST was used in this study. Hussein and Martinuzzi (1996) studied the effects of the flow field around a cube fixed on a wall. The authors focused on the velocity field, vortex, Reynolds stress, turbulent kinetic energy and turbulence dissipation in the backwash of the cube. Merahi et al. (2002) focused on the study of a three-dimensional and incompressible stationary

DOI 10.2478/ama-2019-0023

flow through a cascade of blades using a numerical simulation. The authors concluded that the losses because of the changes in the angle of incidence are the main cause of the decline in the performance of the turbomachines. Martinuzzi and Tropea (1993) used crystal violet, oil-film and laser-sheet visualisation techniques as well as static pressure measurements. The results have shown that the middle region of the wake is nominally two-dimensional for the width-to-height ratios greater than 6. Sarihassoun and Aliane (2016) studied the influence of the curved shape of the lover's edge of a rectangular obstacle. They compared two obstacle models using a qualitative approach, in which they analysed the dimensions of the recirculation zones, the velocity field and the kinetic energy and dissipation. Liao and Chen (2015) studied the velocity field of the flow beyond the obstacles using the particle image velocimetry technique using 8 μm Al_2O_3 powder as tracers. The flow field around the obstacles is obtained. The plots of the current lines and the average velocity field in the horizontal and vertical sections are drawn. The vortex characteristics of the wake flow in various flow fields are studied and compared. Basnet and Constantinescu (2017) conducted 3-D large-eddy simulations to study the physics of flow past 2-D solid and porous vertical plates of height H mounted on a horizontal surface with a fully developed, turbulent incoming flow. The simulation results are used to explain how the bleeding flow affects the dynamics of the larger billow eddies adverted in the separated shear layer (SSL) forming at the top of the plate and the wake structure. Sercan et al. (2017) investigated the flow characteristics around a surface-mounted cube at Re = 3,700 in terms of computational fluid dynamics (CFD) and then compared them with the experimental results using three different models of turbulence. Kanfoudi et al. (2017) used LES to present a numerical analysis of the turbulent flow structure induced by the cavitation shedding. Djeddi et al (2013), simulated a viscous fluid flow on an unconventional diamond-shaped obstacle in a confined channel that is simulated in low-to-moderate Reynolds numbers. The diamond-shaped obstacle is geometrically modified to represent different blocking coefficients depending on the height of the channel and different aspect ratios based on the length-to/height ratios of the obstacle. The simulations are divided into two stationary and unsteady flow groups. Liakos and Malamatris (2014) performed a direct numerical simulation (DNS) of steady-state laminar flow over a cube at Reynolds numbers ranging from 1 to 2,000 based on the cube height. In the same work, Diaz-Daniel et al. (2017) presented a DNS of a wall-attached cube immersed in laminar and turbulent boundary layers at various Reynolds numbers ReH ranging from 500 to 3000. In addition, Sumner et al. (2015, 2017) assessed the effect of the aspect ratio and the incidence angle of the flow above the free end of a surface-mounted finite cylinder and finite-height square prism, and Vinuesa et al. (2017) performed a DNS of the flow around a wall-mounted square cylinder under various inflow conditions and provide the effect of inflow conditions by considering a fully turbulent zero pressure gradient boundary layer. Shinde et al. (2015) presented a LES of flow over a wall-mounted cube-shaped obstacle placed in a spatially evolving boundary layer to understanding how variations in the cube height h modify the flow dynamics for the situation where the cube is within the boundary layer. Amraoui and Aliane (2018) presented the study of fluid flow and heat transfer in solar flat plate collectors by using CFD reduces time and cost. Ennouri et al. (2019) studied the modelling and simulation of the flow inside a centrifugal pump through non-cavitating and cavitating conditions using an SST-(SAS) turbulence model.

2. PROBLEMATIC

The present work contributes to the study of turbulent, stationary, three-dimensional, incompressible flow around a cube that has inclined upstream and downstream edges, mounted inside a horizontal channel. The ANSYS CFX-13 calculation code is used to simulate our configuration. The turbulence models (K-ω SST RANG K-ε and, K-ε) were used, and the governing equations were solved using the finite volume method.

3. MATHEMATICAL FORMULAS

The averaged equations of conservation of mass, momentum and energy are

- The mass conservation equation:

$$\frac{\partial \rho}{\partial t} + \frac{\partial (\rho U_i)}{\partial x_i} = 0 \tag{1}$$

- Momentum conservation:

$$\frac{\partial U_i}{\partial t} + U_j \frac{\partial U_i}{\partial x_j} = -\frac{1}{\rho}\frac{\partial P}{\partial x_i} + \upsilon \frac{\partial^2 U_i}{\partial x_j \partial x_j} \tag{2}$$

- Energy equations:

$$\frac{\partial \overline{T}}{\partial t} + \overline{U}_j \frac{\partial \overline{T}}{\partial x_j} = \frac{\partial}{\partial x_j}\left[\left(\frac{\mu}{\mathrm{Pr}} + \frac{\mu_t}{\mathrm{Pr}_t}\right)\frac{\partial \overline{T}}{\partial x_j}\right] + \frac{1}{\rho C_P}\Phi \tag{3}$$

- Reynolds equations:

$$\rho \frac{\partial \overline{U}_i}{\partial t} + \rho \overline{U}_j \frac{\partial \overline{U}_i}{\partial x_j} = -\frac{\partial \overline{P}}{\partial x_i} + \frac{\partial}{\partial x_j}\left(\mu \frac{\partial \overline{U_i}}{\partial x_j} - \rho \overline{u'_i u'_j}\right) \tag{4}$$

3.1. Model K-ω SST

The model SST is derived from the standard k-ω model. This model combines the robustness and accuracy of the formulation of the k-ω model in the near-wall region with the k-ε model and all its types for the free flow away from the wall. The definition of the turbulent viscosity is modified to take into account the transport of turbulent shear stresses. The formulation of the two-equation model is

$$\rho \frac{\partial k}{\partial t} + \rho \overline{U}_j \frac{\partial k}{\partial x_j} = \tilde{P}_k - \rho C_\mu \omega k + \frac{\partial}{\partial x_j}\left[(\mu + \mu_t/\sigma_k)\frac{\partial k}{\partial x_j}\right] \tag{5}$$

Specific dissipation rate:

$$\rho \frac{\partial \omega}{\partial t} + \rho \overline{U}_j \frac{\partial \omega}{\partial x_i} = 2\alpha\rho S_{ij} S_{ij} - \beta\rho\omega^2 + \frac{\partial}{\partial x_j}\left[\left(\mu_t + \sigma_\omega \mu_t\right)\frac{\partial \omega}{\partial x_j}\right] + 2(1 - F_1)\rho\sigma_{\omega 2}\frac{1}{\omega}\frac{\partial k}{\partial x_j}.\frac{\partial \omega}{\partial x_j} \tag{6}$$

The blend function F_1 is defined using the following equation:

$$F_1 = \tanh\left\{\left\{\min\left[\max\left(\frac{\sqrt{k}}{C_\mu \omega L}, \frac{500\upsilon}{L^2\omega}\right), \frac{4\rho\sigma_{\omega 2} k}{CD_{k\omega} L^2}\right]\right\}^4\right\} \tag{7}$$

Eddy viscosity is given by the following equation:

$$\upsilon_t = \frac{\alpha_1 k}{max(\alpha_1 \omega, \sqrt{2} S_{ij} F_2)} \quad (8)$$

The second blending function is defined using the following equation:

$$F_2 = \tanh\left[\left[\max\left(\frac{2\sqrt{k}}{C_\mu \omega L}, \frac{500\upsilon}{L\omega^2}\right)\right]^2\right] \quad (9)$$

To prevent the accumulation of turbulence stagnation regions, limited production was used:

$$\tilde{P}_k = \min\left(P_k, 10.\, C_\mu \rho k \omega\right) \quad (10)$$

$$P_k = \mu_t \frac{\partial U_i}{\partial x_j}\left(\frac{\partial U_i}{\partial x_j} + \frac{\partial U_j}{\partial x_i}\right) \quad (11)$$

The model constants are calculated using the mixing function

$$\text{F1:} \quad \phi = F_1 \phi_1 + (1 - F_1)\phi_2 \quad (12)$$

The values of the model constants are C_μ=0.09, α_1=5/9, α_2=0.44, β_2 =0.0828, σ_{k_1}=0.85, σ_{k_2}=1.0, σ_{ω_1}=0.5 and σ_{ω_2}=0.856.

3.2. Turbulence model k-ε

To close the system of equations of the problem to be solved and for a much more practical approach, we used the standard k-ε turbulence model (Jones and Launder, 1972); this model is a semi-empirical model with two transport equations based on the concept of Boussinesq linking the constraints of Reynolds to the average deformation rates:

- Turbulent kinetic energy *k*:

$$\frac{\partial}{\partial t}(\rho\kappa) + \frac{\partial}{\partial x_i}(\rho\kappa u_i) = \frac{\partial}{\partial x_i}\left[\frac{\left(\frac{\mu+\mu_t}{\sigma_\kappa}\right)\partial\kappa}{\partial x_i}\right] + P_\kappa + P_b - \rho\varepsilon - Y_M + S_\kappa \quad (13)$$

- Energy dissipation ε:

$$\frac{\partial}{\partial t}(\rho\varepsilon) + \frac{\partial}{\partial x_i}(\rho\varepsilon u_i) = \frac{\partial}{\partial x_i}\left[\left(\mu + \frac{\mu_t}{\sigma_\varepsilon}\right)\frac{\partial\varepsilon}{\partial x_i}\right] + C_{1\varepsilon}\frac{\varepsilon}{\kappa}(P_\kappa + C_{3\varepsilon}P_b) - C_{2\varepsilon}\rho\frac{\varepsilon^2}{k} + S_\kappa \quad (14)$$

P_k represents the term kinetic energy production:

$$P_\kappa = -\rho u_i u_j \frac{\partial u_j}{\partial x_i} \quad (15)$$

The turbulent viscosity is calculated by using the following equation:

$$\mu_t = \rho c_\mu \frac{\kappa^2}{\varepsilon} \quad (16)$$

The five empirical constants of the standard model of turbulence k-ε are

- σ_ε dissipation energy: ∂ε=1.3
- σ_k the Prandtl number of the turbulent kinetic energy: σ_k=1.0
- $C_\mu = 0.09 \quad C_{\varepsilon 1} = 1.44 \quad C_{\varepsilon 2} = 1.92$

4. MODEL DESCRIPTION AND COMPUTATIONAL DOMAIN

The obstacle used in our problem studied (Fig. 1) represents a cube that has inclined upstream and downstream edges, mounted inside a horizontal channel of length (L) and height (h) (Fig. 2)

4.1. Boundary conditions

As the flow is turbulent, three models of turbulence were chosen to analyse the problem more precisely. All "walls" are adiabatic and have no slip conditions.

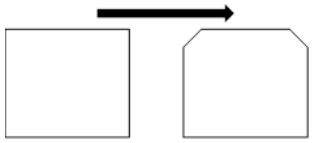

Fig. 1. Model of the body (plan view)

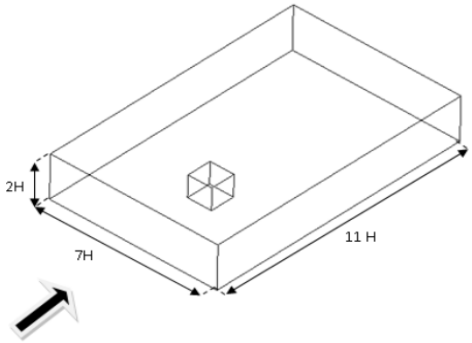

Fig. 2. 3D view of the computational domain of the cube (Rostane and Aliane, 2015)

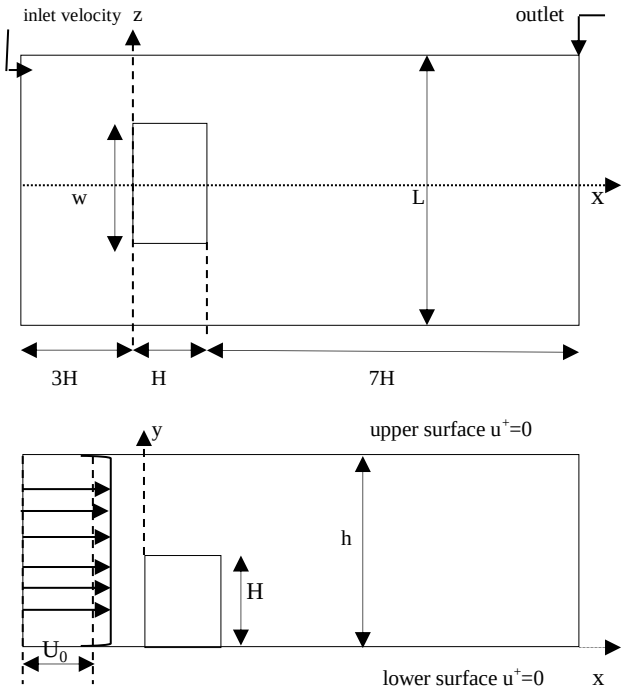

Fig. 3. Geometry of computational domain

DOI 10.2478/ama-2019-0023

According to the models selected previously, equations had to be solved using the following factors:

- The incoming flow velocity U_0 corresponds to the Reynolds number 8.10^4 ($Re=U_0.h/\nu$) and the channel height (h). The height of the obstacle is H=25 mm, and the channel height is h=2H.
- The velocity is zero u=0m/s near the lower and upper walls of the channel and above the obstacle. At the outflow, constant pressure imposed $P_{out}= 0$.

The boundary conditions of the problem treated are given in Figure 3.

To obtain a better precision of the results, it is necessary to generate a well refined mesh. It opted for a structured hexahedral mesh in our case. The meshing of the domain was performed using ANSYS CFX. The general practice is to use fine mesh size in areas of small changes in domain geometry. Figure 4 shows the grid of the mesh used.

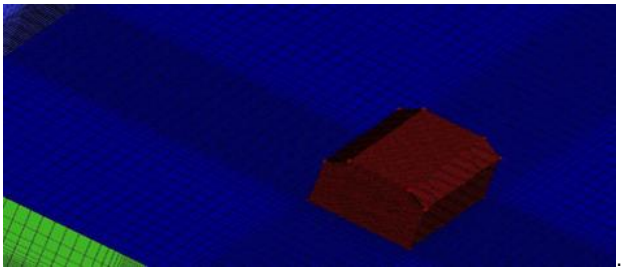

Fig. 4. The mesh grid configuration.

5. FLOW STRUCTURES

The flow above the wall-mounted cube presents a complex phenomenon such as the horseshoe tourbillon, the recirculation zones on the top and the back of the cube, illustrated in Figures 4 and 5. The presence of the obstacle causes the separation of the flow of fluid and the cube in these faces. The flow forms a recirculation zone near these faces, which increases the intensity of the turbulence. With the separation of the fluid flow in the mentioned areas, the fluid velocity increases progressively until it is attached to the near-back edge on the lateral and upper faces. The length of the recirculation zone on the upper face was indicated by L3 in Figure 5. The reinsertion of the flow on the cube takes place at the downstream corners of the upper face and the downstream corner on both sides of the face higher. A large region of separation develops behind the cube, which interacts with the horseshoe vortex. The length of this region was shown with L1. In Figure 6, three-dimensional, unstable and complex circulations in this region increase the intensity of the turbulence.

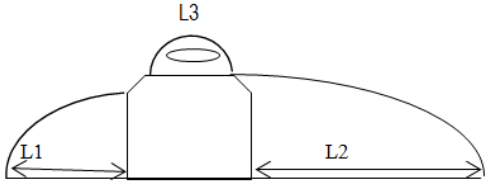

Fig. 5. Flow pattern around an inclined cube attached to the wall with three vortex lengths

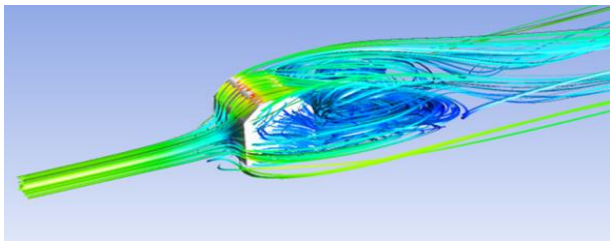

Fig. 6. Time-averaged streamlines around a wall-mounted inclined cube

6. RESULTS AND DISCUSSION

In this study, the flow domain carried out experimentally by Martinuzzi and Tropea (1993) has been prepared to validate the flow characteristics of the surface-mounted cube with a height of H=25mm placed in a channel height of h=2H. The structure of the flow around the obstacle has been validated by the work of Hussein and Martinuzzi (1995) for a Reynolds number of $Re=8{,}0\times10^4$ (Fig.7a). Upstream of the obstacle, a portion of the fluid remains blocked and we observed a small recirculation zone (point (a) to the result of Hussein and Martinuzzi (1995) and point (a') in our results Fig.7b), downstream of the obstacle appears as a large vortex as clearly seen by the two figures (point (b) to the result of Martunizzi and Hussein and point (b') in our results) and above the obstacle, the separation is triggered; it was caused by the upstream stopping point of the obstacle (point of reattachement) (point (c) to the result of Martinuzzi and Hussein and point (c') in our results). The comparison between the two simulations shows that the results are satisfactory and encouraging.

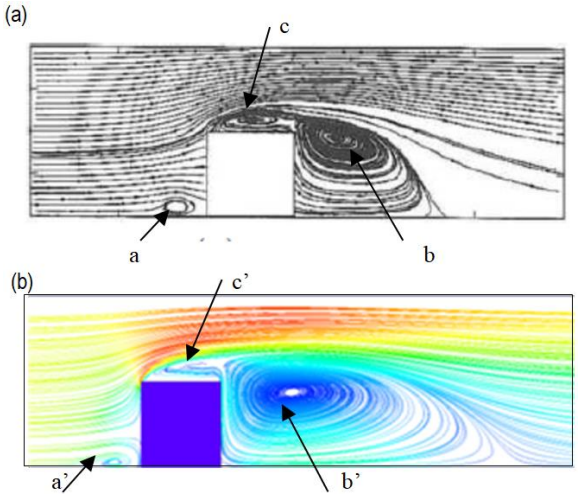

Fig. 7. Streamlines velocity on the symmetry plane at $Re= 8.10^4$ (a): Exp Hussein and Martinuzzi (1995), (b): k- ω SST

The study of the influence of the inclined form of the two upper peaks of a rectangular cube has been examined. A three-dimensional study was carried out using the ANSYS CFX calculation code. Three turbulence models have been used to study the flow characteristics around the inclined cube (K-ω SST, RANG K-ε and K-ε) at the Reynolds number of $Re=8.10^4$. The time-averaged and normalised results of velocity vectors fields <V>, transversal velocity <v> and longitudinal velocity <u> on the symmetry plane (z=0) around the obstacle have been presented in Figure 8.

The velocity vector fields <V> around the surface-mounted body have been illustrated in Figure 8 on the XY plane of the flow

DOI 10.2478/ama-2019-0023

domain and exactly on the plane of symmetry. From Figure 8, the flow has been triggered above the cube and more precisely on the inclined side. We clearly show that the flow was strongly accelerated in the zone above the obstacle. Visibly, the presence of a block inside the channel reduces the flow area causing a strong acceleration of the flow. However, the flow zone was formed for each turbulence model used in our study.

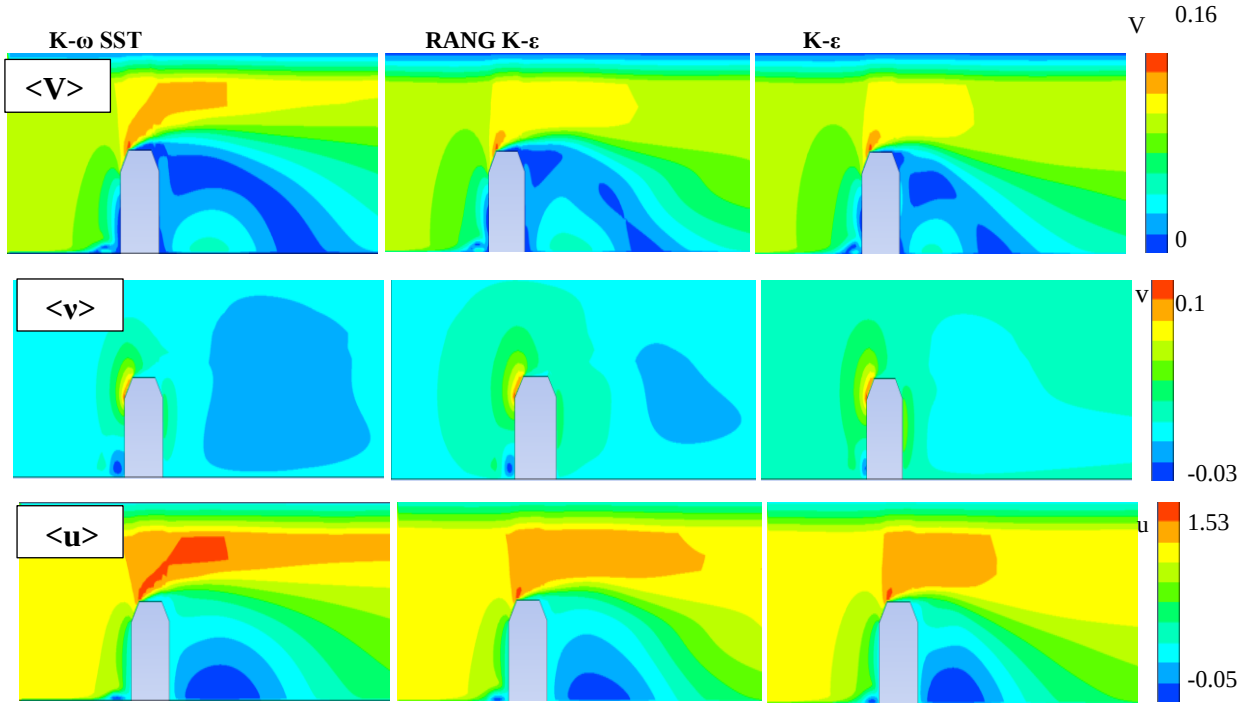

Fig. 8. Comparison of time-averaged results of contours of velocity vectors <V>, cross-stream velocity <v> and streamwise velocity <u> on the symmetry plane (z=0) at Reynolds number (Re=8.10^4)

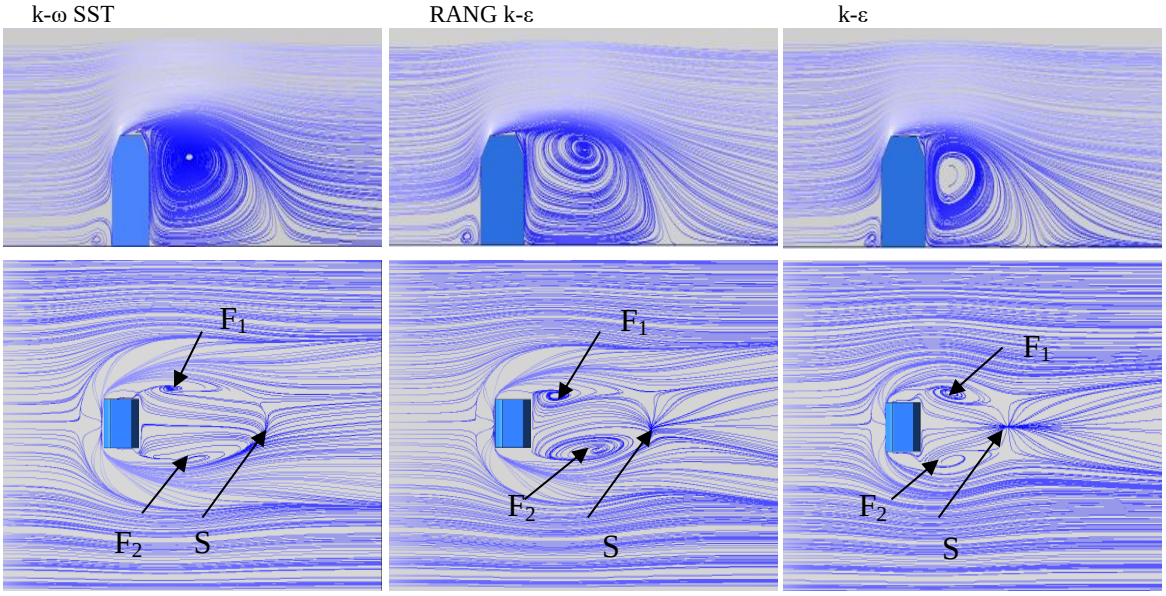

Fig. 9. Time-averaged streamlines on the symmetry plane and at the floor of the channel at the Reynolds number of Re=8.10^4

According to Figure 8, the largest flow area was obtained by the k-w SST method, while the turbulence model k-ε remained limited compared to the other methods.

The contours of the time-averaged streamwise velocity components <u> are presented in the range of -0.05 ≤ <u > ≤ 1.53 for the flow beyond the cube. We saw that the flow accelerated when arriving at the inclined part of the top of the cube and reaches a maximum value. The flux acceleration zone was superior in the case of the k-w SST method, whereas the turbulence model k-ε showed the narrowest. Also, the negative values of velocity components were observed after the cube with different cluster sizes.

The cross-stream velocity components <v > are presented in Figure 8 as 0.03 ≤ <v > ≤ 0.1 to Re = 8.10^4. The positive maximum values of the cross-stream velocity components are achieved above the obstacle and correctly on the inclination. The negative maximum values were dominant behind and upstream of the bottom of the cube.

DOI 10.2478/ama-2019-0023

For accurate flow analysis and for a good vision of separations and reattachments on the top of, at the lateral sides of and behind the obstacle, the time-averaged streamlines on the symmetry plane and at the floor of the channel at the Reynolds number of $Re=8.10^4$ for various turbulence models (K-ω SST, RANG K-ε and K-ε) were presented in Figure 9.

Streamlines on the symmetry plane was illustrated in Figure 8; upstream of the obstacle, a portion of the fluid remains blocked in the region between the inclined upstream edge and the bottom wall of the channel; we observe the formation of a large vortex downstream of the obstacle and above it and the separation is triggered; it is caused by the upstream stopping point of the obstacle, which is achieved for the three models of turbulence but the zone of recirculation was major in the case of the k-ω SST method, whilst the turbulence model k-ε showed the narrowest.

Figure 9 shows the streamlines at the floor of the channel; the blocking effect of the obstacle creates an unfavourable pressure gradient that separates the flow and moves away from the cube, forming a horseshoe vortex. For all models of turbulence, the horseshoe tourbillon appears upstream and bypasses the obstacle. On the other hand, there are two focus (F) points and one saddle (S) point achieved for all methods of turbulence.

In conclusion, it is stated that the turbulence model k-ε did not provide satisfactory results. Although the turbulence model RANG k-ε showed better results than the k-ε method, it remained behind the K-ω SST turbulence model with a narrow margin concerning the flow structure around the surface-mounted cube at $Re=8.10^4$.

6.1. Tracelines

In Figure 10, tracelines on the surface of the cube presented a steady flow in the high face and lateral sides. A separation of flux is observed in the middle of the front face forming a node. On the top of the cube and the high side, the flow is stable until the arrival of the inclined part of the cube; one sees a region of recirculation.

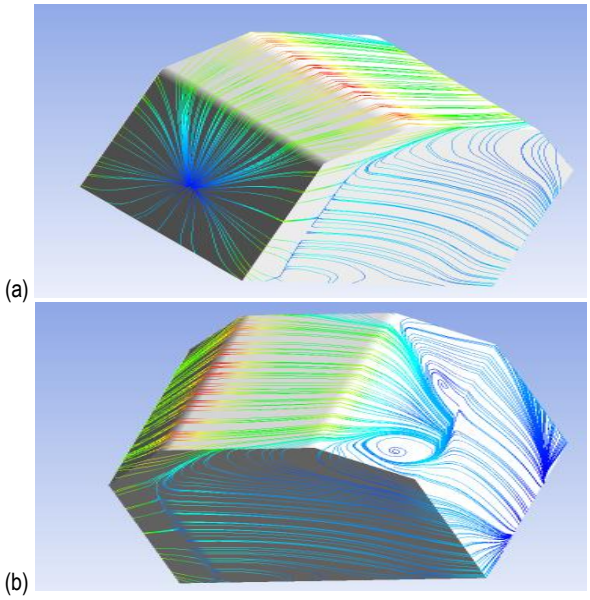

(a)

(b)

Fig. 10. Trace-lines on the surface of the cube: (a) front and side faces; (b) top and side faces

6.2. Streamribbons

Streamribbons are shown in Figure 11 and 12, where an exchange of fluid between the separation regions was observed. From these pictures, it can be concluded that the separation region around a three-dimensional bluff-body cannot be closed.

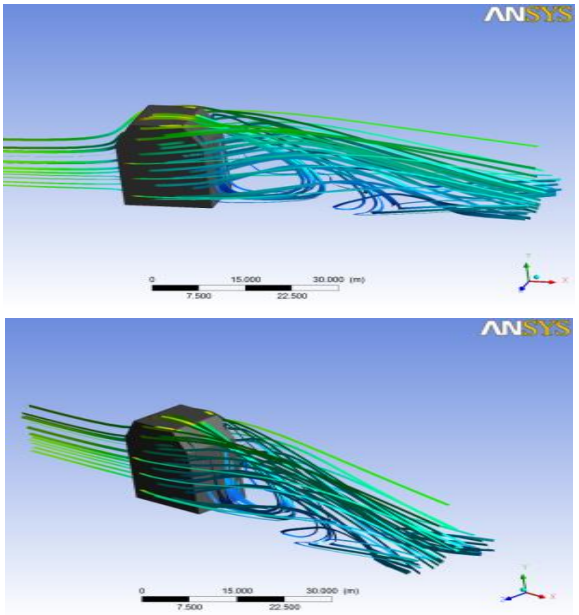

Fig. 11. Streamribbons: lateral and rear view

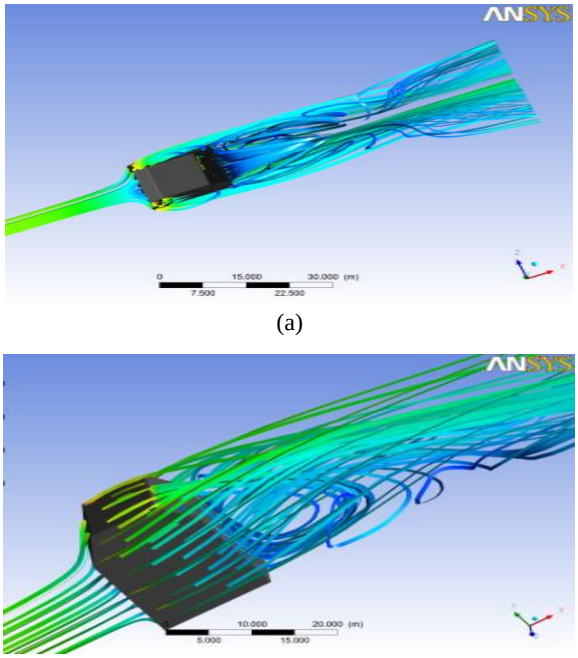

(a)

(b)

Fig. 12. Streamribbons: (a) lower view and (b) the lateral to the backward vortices

6.4. Iso-outline of mean Q-criterion

An overview of the mean flow is illustrated in Figure 13 and represents the isocontour of the mean dimensionless Q-criterion, Qi = 0.15. This criterion is a scalar invariant defined by the equation $Q=-\frac{1}{2} U_{i,j} U_{j,i}=-(\|S^2\| - \|\Omega^2\|)$ (Hunt et al. 1988). We can dimension the Q criterion using the equation $\bar{Q}= Q /(U_b/H)^2$.

Figure 13 shows the presence of a horseshoe vortex denoted by TFC, marginal vortices, denoted TM and wake vortices denoted TV. A sudden reflexion of the fluid is observed immediately after the obstacle. It is clear to see the nascent horseshoe vortex upstream of the obstacle and then the spacing of its legs when the inclined cube is exceeded.

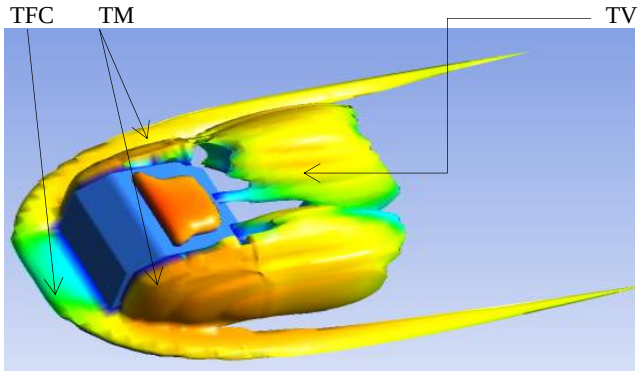

Fig. 13. Iso-outline of mean Q-criterion (Qi = 0.15).

7. CONCLUSION

The problem treated in this work is a three-dimensional simulation using the ANSYS CFX calculation code to carry out a three-dimensional numerical simulation of turbulent flow around an obstacle with inclined upstream and downstream edges. The flow characteristics of the surface-mounted cube as a function of the Reynolds number of Re = 8.10^4 has been studied with three different turbulence models. It has been explained that the satisfactory results have not been obtained using the k-ε and RNG k-ε methods and that the turbulence model k-ω SST gave better results after analyses as a function of time.

This study allowed a 3D simulation to analyse and understand some important physical aspects. In this type of flow, we especially tried to emphasise the role of the presence of obstacles in the channel, the distribution of dynamic and thermal exchanges. The analysis of simulation results confirms the following:

The presence of a block in the flow leads to an increase in the dynamic reciprocity and thus allows the improvement of heat transfer.

- An interaction between recirculation and main flow generates high turbulence; it has been marked in the strong velocity gradients and areas of high curvature trajectories upstream of the disturbance.

REFERENCES

1. **Aliane K**. (2011), Passive control of the turbulent flow over a surface mounted rectangular block obstacle and a rounded rectangular obstacle, International Review of Mechanical Engineering (IREME), 5(2), 305-314.
2. **Aliane K., Sebbane O., Hadjoui A.** (2003), Dynamic study of turbomachine blade cooling models, *Proceedings of the 11th International Day of Thermomics*, Algiers (Algeria), 315-320.
3. **Amraoui M.A., Aliane K. (2018),** Three-dimensional Analysis of Air Flow in a Flat Plate Solar Collector, *Periodica Polytechnica Mechanical Engineering*, 62(2), 126-135.
4. **Basnet K., Constantinescu G.** (2017), The structure of turbulent flow around vertical plates containing holes and attached to a channel bed, *Journal of Physics of Fluids*, 29, 115101.
5. **Becker H. Lienhart F.D.** (2002), Flow around three-dimensional obstacles in boundary layers, *J. Wind Eng. Ind. Aerodyn.*, 90, 265-279.
6. **Bitsuamlak G., Stathopoulos T., Bedard C.** (2006), Effects of upstream two-dimensional hills on design wind loads a computational approach, *Wind and Structures*, 9(1), 37–58.
7. **Diaz-Daniel C., Laizet S., Vassilicos J.** (2017), Direct Numerical Simulations of a wall-attached cube immersed in laminar and turbulent boundary layers, *International Journal of Heat and Fluid Flow (*Preprint submitted).
8. **Djeddi S.R., Masoudi A., Ghadimi P.** (2013), Numerical Simulation of Flow around Diamond-Shaped Obstacles at Low to Moderate Reynolds Numbers, *American Journal of Applied Mathematics and Statistics*, 1(1), 11-20.
9. **Dogan S., Yagmur S., Goktepeli I, Ozgoren M.** (2017), Assessment of Turbulence Models for Flow around a Surface-Mounted Cube, *International Journal of Mechanical Engineering and Robotics Research*, 6(3), 237-241.
10. **Ennouri M., Kanfoudi H., Bel Hadj Taher A., Zgolli R.** (2019), Numerical Flow Simulation and Cavitation Prediction in a Centrifugal Pump using an SST-SAS Turbulence Model, *Journal of Applied Fluid Mechanics*, 12(1), 25-39.
11. **Filippini G., Franck G., Nigro N.** (2005), Large Eddy Simulations of the flow around a square cylinder, *Mecanica Computacional*, XXIV A. Larreteguy (Editor), Buenos Aires, Argentina.
12. **Hadjoui A., Sebbane O., Aliane K., Azzi A.** (2003), Study of the appearance of swirling zones in a flow confronted with obstacles located at the entrance of a canal, *Proceedings of the 9th Congress of the French Society of Process Engineering*, Saint-Nazaire, (France), 224-229.
13. **Hainesa M., Taylor I.** (2018), Numerical investigation of the flow field around low rise buildings due to a downburst event using large eddy simulation, *Journal of Wind Engineering & Industrial Aerodynamics*, 172, 12-30.
14. **Hunt J.C.R., Wray A. A., Moin P.** (1988), *Eddies, stream and convergence zones in turbulent flows*, Technical report, Center of Turbulence Research.
15. **Hussein H.J., Martinuzzi R.J.** (1996), Energy balance for the turbulent flow around a surface mounted cube placed in a channel, *Phys. Fluids*, Vol. 8, No. 3, 764-780.
16. **Hwang J-Y, Yang K-S.** (2010), Numerical study of vertical structures around a wall-mounted cubic obstacle in channel flow, Physics of Fluids, 16(7), 2382-2394.
17. **Jones W.P., Launder B.E.** (1972), The prediction of laminarization with a two-equation model of turbulence, *International Journal of Heat and Mass Transfer*, 15, 301-14.
18. **Kanfoudi H., Bellakhall G., Ennouri M., Bel Hadj Taher A., Zgolli R.** (2017), Numerical Analysis of the Turbulent Flow Structure Induced by the Cavitation Shedding Using LES, *Journal of Applied Fluid Mechanics*, 10(3), 933–46.
19. **Krajnovi'c S., Davidson L.** (2002), Large-eddy simulation of the flow around a bluff body, *AIAA Journal*, 40(5), 927-936.
20. **Liakos A., Malamataris N.A**. (2014), Direct numerical simulation of steady state, three dimensional, laminar flow around a wall mounted cube, *Physics of Fluids*, 26(5), 053603.
21. **Liao B., Shan-Qun C.** (2015), Experimental study of flow past obstacles by PIV, *7th International Conference on Fluid Mechanics*, ICFM7, Procedia Engineering, 126, 537 – 541.

DOI 10.2478/ama-2019-0023

22. **Lim H.C., Thomas T.G., Castro I. P.** (2009), Flow around a cube in a turbulent boundary layer: LES and experiment, *Journal of Wind Engineering and Industrial Aerodynamics*, 97(2), 96–109.
23. **Martinuzzi R., Tropea C.** (1993), The flow around a surface-mounted prismatic obstacle placed in a fully developed channel flow, *J. Fluids Eng.*, 115, 85-92.
24. **Merahi.l , Abidat .M, Azzi.A, Hireche.O** (2002), Numerical assessment of incidence losses in an annular blade cascade, *Séminaire international de Génie Mécanique*, Sigma'02 ENSET, Oran.
25. **Nemdili S., Nemdili F., Azzi A.** (2015), Improving cooling effecti veness by use of chamfers on the top of electronic components, Microelectronics Reliability, 55(7), 1067-1076.
26. **Rostane B. , Aliane K.** (2015), Three Dimensional Simulation for Turbulent Flow Around Prismatic Obstacle with Rounded Downstream Edge Using the k-ω SST Model, *International Review of Mechanical Engineering* (I.RE.M.E.), 9(3), 266.277.
27. **Sari-Hassoun Z., Aliane K..** (2016), Numerical simulation of turbulent flow around obstacles with a curved upstream edge, International *Journal of Scientific Research & Engineering Technology* (IJSET), 196-201.
28. **Sebbane O., Hadjoui A., Aliane K., Azzi A.** (2003), New method of visualization of flows with very large Reynolds number, *Proceedings of the 9th Congress of the French Society of Process Engineering*, Saint -Nazaire, France, 259-264.
29. **Shinde S., Johnseny E., Makiz K.** (2017), Understanding the effect of cube size on the near wake characteristics in a turbulent boundary layer, *47th AIAA Fluid Dynamics Conference*, Denver, Colorado.
30. **Sumner D., Rostamy N., Bergstrom D., Bugg J**. (2015), Influence of aspect ratio on the flow above the free end of a surface-mounted finite cylinder, *International Journal of Heat and Fluid Flow*, 56, 290-304.
31. **Sumner D., Rostamy N., Bergstrom D., Bugg J.D.** (2017), Influence of aspect ratio on the mean flow field of a surface-mounted finite-height square prism, *International Journal of Heat and Fluid Flow*, 65, 1-20.
32. **Vinuesa R., Schlatter P., Malm J., Mavriplis C., Henningson, D.S.** (2015), Direct numerical simulation of the flow around a wall-mounted square cylinder under various inflow conditions, J*ournal of Turbulence*, 16, 555-587.
33. **Yakhot A., Liu H., Nikitin N.** (2006), Turbulent flow around a wall-mounted cube: A direct numerical simulation, *International Journal of Heat and Fluid Flow*, 27(6), 994-1009.

sciendo

DOI 10.2478/ama-2019-0024

acta mechanica et automatica, vol.13 no.3 (2019)

COMPARATIVE STUDY OF STABILIZATION CONTROLS OF A FORKLIFT VEHICLE

Augie WIDYOTRIATMO*

*Faculty of Industrial Technology, Instrumentation and Control Research Group,
Insititut Teknologi Bandung, Ganesa 10, Bandung 40132, Indonesia

augie@tf.itb.ac.id

received 7 January 2019, revised 26 September, accepted 30 September

Abstract: This paper presents the control designs for an autonomous forklift vehicle that drive the vehicle from an initial configuration to a final one. Three stabilization controls, which are chained-form time-varying control, sigma-transformed discontinuous control, and navigation-variables-based discontinuous control, for a forklift vehicle are compared by simulations. The sigma-transformed and navigation-variables-based discontinuous controls provide fast convergence motions from an initial to a final configuration, while the time-varying-based control provides oscillatory motion and slow convergence. The sigma-transformed discontinuous control has a set of discontinuous points in which, from a practical point of view, the control signals can blow up if a vehicle enters the set. The navigation-variables-based control, which also has a discontinuous point at the final configuration, does not produce blown up control signals since its boundedness nature. Discussion on the implementation of control algorithm is elucidated for the three stabilization controls for the forklift vehicle.

Key words: Autonomous vehicle, stabilization control, time-varying-based control, discontinuous control, navigation-variables-based control

1. INTRODUCTION

Control design of autonomous vehicle is still of interest to many researchers, especially in dealing with implementation (Kłosiński et al., 2015; Virgalaivan et al., 2018; Widyotriatmo and Hong, 2015; Baranowski and Siwek, 2018). One of the applications is the stabilization control, which is the design of control algorithm to drive an autonomous vehicle from an initial configuration to a final configuration. The configuration is not only the position but also the orientation of the vehicle.

A wheeled vehicle is a nonholonomic system (i.e., a system with nonholonomic constraints). Brockett (1983) showed that there is no continuously differentiable time-invariant control law that stabilizes a nonholonomic system asymptotically. Two control strategies for nonholonomic systems are found in the literature: open loop and closed loop strategies. In open loop strategies (Murray and Sastry, 1993; Soueres and Laumond, 1996; Widyotriatmo and Hong, 2008), the control signals are calculated off-line using the information of the initial and the goal configurations. Using this strategy, the vehicle may not reach the goal configuration due to disturbances, modelling errors, and sensor uncertainties. In closed loop strategies, the control signals are computed online based on the current and goal configurations. A coordinate transformation is used. Examples of coordinate transformation are the chained form (Murray and Sastry, 1993), the power form (Pomet and Samson, 1994), the polar coordinates (Aicardi et al., 1995), the sigma process (Astolfi, 1996), the differential flatness approach (Lamiraux and Laumond, 2000; Tang et al., 2008; Ryu and Agarwal, 2010), and the transverse form (Morin and Samson, 2009). Several control algorithms proposed are the time-varying control (Samson, 1995; Tamba et al., 2009; Wang et al., 2015), discontinuous control (Lamiraux and Laumond, 2000), and the switching method (Hespanha and Morse, 1999). Control laws using polar coordinates are utilized (Widyotriatmo and Hong, 2015; Astolfi, 1996; Siegwart and Nourbakhsh, 2004). Unlike the previous studies, which considered unicycle-type vehicles, the stabilization control for forklift vehicle is focused.

In dealing with the stabilization of nonholonomic wheeled mobile robots system, the system needs to be transformed into a special structure as in Abbasi et al. (2019), the power form (Xie and Li, 2019), chained form (S'anchez-Torres et al., 2019), or the polar or navigation-variable form (Widyotriatmo and Hong, 2012). Then, the control designs are implemented in the forms of time-varying or discontinuous controls. In Widyotriatmo and Hong (2012), experimental results for the stabilization of forklift vehicle using the navigation-variable form transformation has been performed. Other experimental results of a car-like-vehicle using a discontinuous control has been shown in Hashimoto et al. (2019). A switched pivot and longitudinal motions are also performed for point stabilization for a differential wheel robot with inverted pendulum Yue et al. (2019). Lyapunov method is established for the stabilization of mobile robot with inverted pendulum in Muralidharan and Mahindrakar (2014). Simultaneous stabilization and tracking of a nonholonomic robot using Lyapunov based approach is proposed in Wand et al. (2015). In Muralidharan and Mahindrakar (2013), the stabilization of mobile robot with constraints of configuration is solved by sliding mode technique. Stabilization of a mobile robot using model predictive control is presented in Xiao et al. (2017), Wei et al. (2013).

Different transformations and control strategies claim the effectiveness of the stabilization result. The question leads to how the control performances of the individual strategies of transformed systems for the forklift vehicle are. In this paper, the performances of the three configuration control laws, which are the time-varying-based control in the chained-form, the discontinuous

DOI 10.2478/ama-2019-0024

control using sigma process, and the navigation-variables-based control, for asymptotically stabilizing the configuration error of the vehicle are compared. The trajectories calculated using the individual control laws are presented by simulations. From this simulation, the use of the three configuration control laws is analysed. The objective of this paper is to determine which transformation and control strategy are the most effective in stabilizing a forklift vehicle, focusing on the ease of implementation and on the resulted motion in driving the forklift from an initial configuration to a final one. By studying the comparisons of different transformation and control strategies, the engineer who applies the stabilization control of a forklift vehicle can understand the consequences in implementing a chosen control algorithm.

The equations of motion of the considered forklift are derived. The equations are represented kinematic and dynamic equations. The kinematic equations describe the velocity of the vehicle with the inputs of linear velocity and steering angle, and the dynamic equations provide the accelerations of the vehicle and the torques of the actuators of driving and steering. The control problem is divided into two stages. First, the linear velocity and the steering angle of the kinematic equations are designed and become the references for the dynamic model. And then, the input to two actuators (driving and steering) are calculated in such a way that the two actuators track the linear velocity and the steering angle.

The rest of this paper is organized as follows. The equations of motion of the vehicle are derived in Section II. The implementation of the PD control for the direct current (DC) motor control is discussed in Section III. Section IV presents the three configuration control laws for the forklift. Section V shows the simulation results and discussion. The conclusions are drawn in Section VI.

2. EQUATIONS OF MOTION OF FORKLIFT VEHICLE

Let the global coordinate frame $O-\hat{\imath}\hat{\jmath}$ be fixed in the workspace as in Fig. 1. The body coordinate is denoted as $O_{\mathrm{b}}-\hat{\imath}_{\mathrm{b}}\hat{\jmath}_{\mathrm{b}}$, l is the length from the rear wheel to O_{b}. The position of the vehicle is (x,y) located at O_{b} and the orientation θ. The linear velocity and steering angle are denoted by v and δ, respectively.

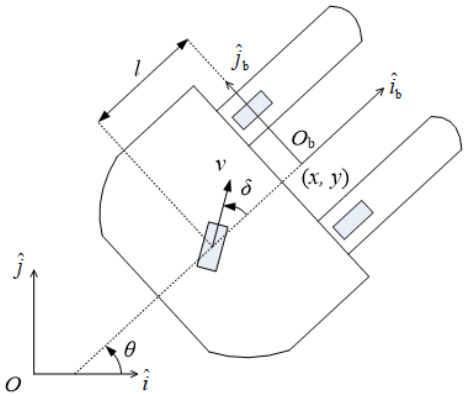

Fig. 1. The schematic of forklift vehicle

The angular positions of the front and rear wheels are denoted by φ_{f} and φ_{b}, respectively. Let q be the state vector $\mathrm{q}=\left[x,\ y,\ \theta,\delta,\varphi_f,\varphi_b\right]^T\in R^6$. The equations of motion of the forklift vehicle are:

$$\mathrm{M(q)\ddot{q}+C(q,\dot{q})\dot{q}+f}_s+\mathrm{g(q)=B(q)\tau+J(q)f}_C, \tag{1}$$

$$\mathrm{J}^T(\mathrm{q})\dot{\mathrm{q}}=0, \tag{2}$$

where: $\mathrm{M(q)}\in R^{6\times6}$ is the inertia matrix, $\mathrm{C(q,\dot{q})}\in R^{6\times6}$ is the centripetal and Coriolis matrix, $\mathrm{f}_s\in R^6$ is the surface friction vector, $\mathrm{g(q)}\in R^6$ is the gravitational vector, $\mathrm{B(q)}\in R^{6\times2}$ is the input matrix, $\tau=[\tau_{\mathrm{v}},\tau_\delta]^T\epsilon R^2$ is the torque inputs vector of the driving and steering motors, respectively, $\mathrm{f}_C\in R^4$ is the force vector denoting the constraint, and $\mathrm{J(q)}\in R^{6\times4}$ is the constraint. Since the vehicle moves on the flat surface $\mathrm{g(q)}=0$.

For non-slipping and pure rolling conditions, the constraint matrix $\mathrm{J(q)}$ is:

$$\mathrm{J(q)}=\begin{bmatrix}J_{11}&J_{12}&J_{13}&J_{14}\\J_{21}&J_{22}&J_{23}&J_{24}\\J_{31}&J_{32}&J_{33}&J_{34}\\J_{41}&J_{42}&J_{43}&J_{44}\\J_{51}&J_{52}&J_{53}&J_{54}\\J_{61}&J_{62}&J_{63}&J_{64}\end{bmatrix}, \tag{3}$$

where: $J_{11}=-\sin\theta$, $J_{12}=-(\cos\theta\sin\delta+\sin\theta\cos\delta)$, $J_{13}=\cos\theta$, $J_{14}=\cos\theta\cos\delta-\sin\theta\sin\delta$, $J_{21}=\cos\theta$, $J_{22}=\cos\theta\cos\delta-\sin\theta\sin\delta$, $J_{23}=\sin\theta$, $J_{24}=\cos\theta\sin\delta+\sin\theta\cos\delta$, $J_{32}=-l\cos\delta$, $J_{34}=-l\sin\delta$, $J_{53}=-r_f$, $J_{64}=-r_r$, and $J_{31}=J_{32}=J_{33}=J_{34}=J_{51}=J_{52}=J_{54}=J_{61}=J_{62}=J_{63}=0$, r_f and r_r are the radii of the wheels of the vehicle, at the front and rear. A matrix $\mathrm{S(q)}\in R^{6\times2}$ is defined as:

$$\mathrm{S(q)}=\begin{bmatrix}S_{11}&S_{12}&S_{13}&S_{14}&S_{15}&S_{16}\\S_{21}&S_{22}&S_{23}&S_{24}&S_{25}&S_{26}\end{bmatrix}^T, \tag{4}$$

where: $S_{11}=\cos\theta\cos\delta$, $S_{11}=\sin\theta\cos\delta$, $S_{13}=-(1/l)\sin\delta$, $S_{15}=(1/r_{\mathrm{f}})\cos\delta$, $S_{16}=1/r_r$, $S_{24}=1$, and $S_{21}=S_{22}=S_{23}=S_{25}=S_{26}=0$, such that $\mathrm{S(q)}^T\mathrm{J(q)}=0$. The velocity vector $\mathrm{v}=[v\quad\dot{\delta}]^T$ is defined where v is the linear velocity and the angular velocity $\dot{\delta}$. The derivative of q with respect to time is:

$$\dot{\mathrm{q}}=\mathrm{S(q)v}, \tag{5}$$

Lagrange method is used to obtain (1). The kinetic energy K is:

$$K=\frac{1}{2}\dot{\mathrm{q}}^{\mathrm{T}}\mathrm{M}\dot{\mathrm{q}}, \tag{6}$$

where:

$$\mathrm{M=diag}(m,m,I_{\mathrm{b}},I_\delta,I_{\mathrm{f}},I_{\mathrm{r}}), \tag{7}$$

m is the vehicle's mass, I_{b} is the moment of inertia around O_{b}, I_δ is the moment of inertia of the rear wheel towards its normal axis, and I_{f} and I_{r} are the front and rear wheels' moments of inertia. The centripetal and Coriolis matrix is:

$$\mathrm{C(q,\dot{q})}=\dot{\mathrm{M}}(\mathrm{q})\dot{\mathrm{q}}-\partial K/\partial\mathrm{q}=0, \tag{8}$$

and the input transformation $\mathrm{B(q)}$ is:

$$\mathrm{B(q)}=\begin{bmatrix}0&0&0&0&0&1\\0&0&0&1&0&0\end{bmatrix}^T. \tag{9}$$

The second derivative of vector q is:

$$\ddot{\mathrm{q}}=\mathrm{S(q)}\dot{\mathrm{v}}+\dot{\mathrm{S}}(\mathrm{q},\dot{\mathrm{q}})\mathrm{v}. \tag{10}$$

Substituting (10) into (1), and multiplying by $S^T(q)$ of both sides, it is obtained:

$$M_1(q)\dot{v} + C_1(q,\dot{q})v + f_1 = B_1(q)\tau, \quad (11)$$

where:

$$M_1(q) = S^T(q)M(q)S(q), \quad (12)$$

$$C_1(q,\dot{q}) = S^T(q)M(q)\dot{S}(q), \quad (13)$$

$$f_1 = S^T(q)f = [f_v \quad f_\delta]^T, \quad (14)$$

$$B_1(q) = \mathrm{diag}(1/r_r, 1), \quad (15)$$

f_v and f_δ are the surface frictions in the directions of linear velocity and steering angle of the rear wheel. Then, the equations of motion are:

$$\dot{x} = v\cos\theta\cos\delta, \quad (16)$$

$$\dot{y} = v\sin\theta\cos\delta, \quad (17)$$

$$\dot{\theta} = -(v/l)\sin\delta, \quad (18)$$

$$m_1\dot{v} + c_1 v + r_r f_v = \tau_v, \quad (19)$$

$$I_\delta\ddot{\delta} + f_\delta = \tau_\delta, \quad (20)$$

where:

$$m_1 = r_r\left((m + I_f)(\cos\delta)^2 + (I_b/l^2)(\sin\delta)^2 + I_r\right), \quad (21)$$

$$c_1 = r_r\left((I_b/l^2) - (I_f/r_f^2) - m\right)\dot{\delta}\cos\delta\sin\delta. \quad (22)$$

The equations (16)–(18) show the kinematic equations, (19) and (20) are the traction and steering dynamics, respectively.

3. MOTOR CONTROL

The rear wheel in (19)–(20) are controlled by the torques τ_v and τ_δ as:

$$\tau_v = \left(k_{m,v}/R_{m,v}\right)\left((u_v - \left(k_{emf,v}/r_r\right)v\right), \quad (23)$$

$$\tau_\delta = \left(k_{m,\delta}/R_{m,\delta}\right)\left(u_\delta - k_{emf,\delta}\dot{\delta}\right), \quad (24)$$

where: u_v and u_δ are the control signals for the driving and steering motors. $k_{m,i}$ is the motor torque constant, $k_{emf,i}$ is the back electromotive constant, and $R_{m,i}$ is the motor resistance, of the i -th motor, $i = v, \delta$.

The desired linear velocity v_d and steering angle δ_d is controlled by the PD with control signals u_v and u_δ are designed as:

$$u_v = k_{P,v}(v_d - v) - k_{D,v}\dot{v}, \quad (25)$$

$$u_\delta = k_{P,\delta}(\delta_d - \delta) - k_{D,\delta}\dot{\delta}, \quad (26)$$

where: $k_{P,i}$ is the proportional gain, $k_{D,i}$ is the derivative gain of the i -th motor, $i = v, \delta$. Using (23) and (25), (19) becomes

$$\left(\frac{R_{m,v}m_1}{k_{m,v}} + k_{D,v}\right)\dot{v} + \left(\frac{R_{m,v}c_1}{k_{m,v}} + \frac{k_{emf,v}}{r_r} + k_{P,v}\right)v = k_{P,v}v_d - \frac{R_{m,v}r_r}{k_{m,v}}f_v. \quad (27)$$

By choosing $k_{P,v} > \max\left((R_{m,v}/k_{m,v})c_1 - k_{emf,v}/r_r\right)$ and assuming f_v is constant, the solution of (27) is obtained as:

$$v(t) = \frac{k_{p,v}}{\frac{(c_1R_{m,v})}{k_{m,v}} + \frac{k_{emf,v}}{r_r} + k_{p,v}}\left(v_d - \frac{R_{m,v}r_r}{k_{m,v}k_{p,v}}f_v - \left(v_d - v(t_0) - \frac{R_{m,v}r_r}{k_{m,v}k_{p,v}}f_v\right)\exp(-\lambda_v t)\right), \quad (28)$$

where:

$$\lambda_v = \frac{\left(\frac{c_1R_{m,v}}{k_{m,v}} + \frac{k_{emf,v}}{r_r} + k_{P,v}\right)}{\left(\frac{m_1R_{m,v}}{k_{m,v}} + k_{D,v}\right)} > 0. \quad (29)$$

Using (24) and (26), (20) becomes:

$$\left(\frac{I_\delta R_{m,\delta}}{k_{m,\delta}k_{P,\delta}}\right)\ddot{\delta} + \left(\frac{k_{D,\delta} + k_{emf,\delta}}{k_{P,\delta}}\right)\dot{\delta} + \delta = \delta_d - \left(\frac{R_{m,\delta}}{k_{m,\delta}k_{P,\delta}}\right)f_\delta. \quad (30)$$

The parameters $k_{P,\delta}$ and $k_{D,\delta}$ are chosen such that:

$$\left(\left(k_{D,\delta} + k_{emf,\delta}\right)/k_{P,\delta}\right)^2 - 4\left(R_{m,\delta}I_\delta\right)/\left(k_{m,\delta}k_{P,\delta}\right) > 0. \quad (31)$$

The solution of (30) becomes

$$\delta(t) = \delta_d - \frac{R_{m,\delta}}{k_{m,\delta}k_{P,\delta}}f_\delta - \left(\delta_d - \delta(t_0) - \frac{R_{m,\delta}}{k_{m,\delta}k_{P,\delta}}f_\delta\right)\times\left(\frac{\lambda_{\delta,2}\exp(-\lambda_{\delta,1}t) - \lambda_{\delta,1}\exp(-\lambda_{\delta,2}t)}{\lambda_{\delta,2} - \lambda_{\delta,1}}\right), \quad (32)$$

where:

$$\lambda_{\delta,1} = \frac{\frac{k_{D,\delta}+k_{emf,\delta}}{k_{P,\delta}} + \left(\left(\frac{k_{D,\delta}-k_{emf,\delta}}{k_{P,\delta}}\right)^2 - \frac{4R_{m,\delta}I_\delta}{k_{m,\delta}k_{P,\delta}}\right)^{\frac{1}{2}}}{2\frac{R_{m,\delta}I_\delta}{k_{m,\delta}k_{P,\delta}}} > 0, \quad (33)$$

$$\lambda_{\delta,2} = \frac{\frac{k_{D,\delta}+k_{emf,\delta}}{k_{P,\delta}} - \left(\left(\frac{k_{D,\delta}-k_{emf,\delta}}{k_{P,\delta}}\right)^2 - \frac{4R_{m,\delta}I_\delta}{k_{m,\delta}k_{P,\delta}}\right)^{\frac{1}{2}}}{2\frac{R_{m,\delta}I_\delta}{k_{m,\delta}k_{P,\delta}}} > 0. \quad (34)$$

It can be seen that in (28) and (32), the PD control can make the linear velocity v and the steering angle δ to track the desired values v_d and δ_d with some errors caused by the frictions and the decaying exponential function. It is assumed that the friction is very small and so that the PD control can track the desired values.

4. STABILIZATION CONTROLS

By assuming the ideal linear velocity and steering angle as inputs ($v = v_d$, $\delta = \delta_d$), the configuration control algorithms for the forklift based on the time-varying-based control using chained-form with time-varying control, sigma-transformed discontinuous control, and navigation-variables-based control are investigated. Without loss of generality, the goal configuration is set to $(x_g, y_g, \theta_g) = (0, 0, 0)$.

Let $v_1 = v\cos\delta$ and $v_2 = v\sin\delta$. In terms of v_1 and v_2, The linear velocity and steering angle are calculated as follows:

$$v = \mathrm{sgn}(v_1)\sqrt{v_1^2 + v_2^2}, \quad (35)$$

$$\delta = arctan(v_2/v_1). \quad (36)$$

The kinematic equations in (16)–(18) becomes:

$$\dot{x} = v_1\cos\theta, \quad (37)$$

DOI 10.2478/ama-2019-0024

$$\dot{y} = v_1 \sin\theta, \tag{38}$$

$$\dot{\theta} = -v_2/l. \tag{39}$$

Let $\tilde{x} = x_g - x$, $\tilde{y} = y_g - y$, and $\tilde{\theta} = \theta_g - \theta$ be the errors between the current and final configurations. Using the kinematic equations in (37)–(39), the individual transformations, which are the chain form for deriving the time-varying-based control, the sigma process for calculating the discontinuous control, and the navigation-variables for obtaining the navigation-variables-based control are introduced in the following subsections.

4.1. Chained-form time-varying-based control

In deriving the time-varying-based control, the following chained-form space (χ_1',χ_2',χ_3') is introduced:

$$\chi_1' = \tilde{\theta}, \tag{40}$$

$$\chi_2' = \tilde{x}\sin\tilde{\theta} - \tilde{y}\cos\tilde{\theta}, \tag{41}$$

$$\chi_3' = \tilde{x}\cos\tilde{\theta} + \tilde{y}\sin\tilde{\theta}, \tag{42}$$

$$v_1' = -(v_2/l), \tag{43}$$

$$v_2' = v_1 - \chi_2' v_2/l. \tag{44}$$

From (40)–(42), the origins of the state of the chained-form space (χ_1',χ_2',χ_3') and the configuration error space ($\tilde{x}$,$\tilde{y}$,$\tilde{\theta}$) coincide. Thus, the asymptotical stabilization problem of the configuration error space becomes that of the chained-form space. The chained-form satisfies the following:

$$\dot{\chi}_1' = v_1', \tag{45}$$

$$\dot{\chi}_2' = \chi_3 v_1', \tag{46}$$

$$\dot{\chi}_3' = v_2'. \tag{47}$$

The control law for stabilizing the chained-form of (45)–(47) is declared in Theorem 1.

Theorem 1: Consider the chained form system (45)–(47). Let the control law v_1' and v_2' be designed as

$$v_1' = -k_{v,1}\chi_1' + (\chi'^2_2 + \chi'^2_3)\sin t, \tag{48}$$

$$v_2' = -\chi_2' v_1' - k_{v,2}\chi_3', \tag{49}$$

where $k_{v,1}$ and $k_{v,2}$ are positive constants. Then, the origin (χ_1', χ_2', χ_3') = (0, 0, 0) is asymptotically stable.

Proof: Using (48)–(49), (45)–(47) becomes:

$$\dot{\chi}_1' = -k_{v,1}\chi_1' + (\chi'^2_2 + \chi'^2_3)\sin t, \tag{50}$$

$$\dot{\chi}_2' = -k_{v,1}\chi_1'\chi_3' + (\chi'^2_2 + \chi'^2_3)\chi_3'\sin t, \tag{51}$$

$$\dot{\chi}_3' = -k_{v,2}\chi_3' + k_{v,1}\chi_1'\chi_2' - (\chi'^2_2 + \chi'^2_3)\chi_2'\sin t. \tag{52}$$

Note that $(\chi'^2_2 + \chi'^2_3)\sin t$ is a time-varying function that satisfies $(\chi'^2_2 + \chi'^2_3)\sin t = 0$ as χ_2', χ_3' = 0.

From (50), χ_1' is bounded, which implies that v_1' is also bounded. The Lyapunov function V_c is defined as:

$$V_c = \chi'^2_2 + \chi'^2_3. \tag{53}$$

Using (51)–(52), the time-derivative of the Lyapunov function (53) becomes:

$$\dot{V}_c = -k_{v,1}\chi'^2_3 \leq 0. \tag{54}$$

This implies that $\chi_3' \to 0$ as $t \to \infty$. Then, from (51) and (52), it can be concluded that $\chi_2' \to 0$ as $t \to \infty$. Since $(\chi'^2_2 + \chi'^2_3)\sin t$ = 0 as χ_2', χ_3' = 0, v_1' tends to zero. Then from (48), it can be concluded that $\chi_1' \to 0$ as $t \to \infty$. Thus, it is obtained that χ_1', χ_2', $\chi_3' \to 0$ as $t \to \infty$.

4.2. Sigma-transformed discontinuous-based control

The sigma-transformed discontinuous-based control is derived using the following transformation:

$$\chi_1'' = \tilde{x}, \tag{55}$$

$$\chi_2'' = \tilde{y}/\tilde{x}, \tag{56}$$

$$\chi_3'' = \tilde{\theta}, \tag{57}$$

$$v_1'' = v_1\cos\tilde{\theta}, \tag{58}$$

$$v_2'' = -v_2/l. \tag{59}$$

As in the chained form, the origins of the state of the sigma transformation space (χ_1'',χ_2'',χ_3'') and the configuration error space ($\tilde{x}$,$\tilde{y}$,$\tilde{\theta}$) also coincide. The transformed system is described by:

$$\dot{\chi}_1'' = v_1'', \tag{60}$$

$$\dot{\chi}_2'' = v_1''(tan\,\chi_3'' - \chi_2'')/\chi_1'', \tag{61}$$

$$\dot{\chi}_3'' = v_2''. \tag{62}$$

The control law of the sigma-transformed discontinuous-based control is expressed in Theorem 2.

Theorem 2: Consider the system in (60)–(62). Let the control law v_1'' and v_2'' be

$$v_1'' = -k_{v,1}\chi_1'', \tag{63}$$

$$v_2'' = k_{v,2}\chi_2'' + k_{v,3}\chi_3'', \tag{64}$$

where $k_{v,1}$, $k_{v,2}$, and $k_{v,3}$ are the control parameters that are chosen in such a way that the matrix of linearized system have negative eigen-values. Then the origin of (χ_1'',χ_2'',χ_3'') is asymptotically stable.

Proof: The substitution of (63)–(64) into (60)–(62) yields:

$$\dot{\chi}_1'' = -k_{v,1}\chi_1'', \tag{65}$$

$$\dot{\chi}_2'' = -k_{v,1}(tan\,\chi_3'' - \chi_2''), \tag{66}$$

$$\dot{\chi}_3'' = -k_{v,2}\chi_2'' - k_{v,3}\chi_3''. \tag{67}$$

By linearizing the system (66)–(67) around the origin, we obtain:

$$\begin{bmatrix}\dot{\chi}_2''\\ \dot{\chi}_3''\end{bmatrix} = A\begin{bmatrix}\chi_2''\\ \chi_3''\end{bmatrix},\ A = \begin{bmatrix}k_{v,1} & -k_{v,1}\\ -k_{v,2} & -k_{v,3}\end{bmatrix}. \tag{68}$$

From (65), it is obvious that χ_1'' goes to zero as time goes to infinity. If $k_{v,1} > 0$, $k_{v,2}$ and $k_{v,3}$ are designed such that the matrix A has all the eigenvalues with negative real part, χ_2'', χ_3'' go to zero as time goes to infinity. Thus, the origin of (χ_1'', χ_2'', χ_3'') = (0, 0, 0) is asymptotically stable.

□

4.3. Navigation-Variables-Based Control

The navigation-variables-based control is classified as the discontinuous control. The coordinate of the forklift is to be transformed to specific variables, called navigation variables, as the distance error (ρ), the orientation error component associated with the direction to the goal point (α), and the orientation error component associated with the direction of the goal frame (φ). Note that $\tilde{\theta} = \alpha + \varphi$. In Fig. 2, the navigation variables are obtained as follows:

$$\rho = \sqrt{\tilde{x}^2 + \tilde{y}^2}, \tag{69}$$

$$\alpha = arctan\,2\,(\tilde{y},\ \tilde{x}) - \tilde{\theta}, \tag{70}$$

$$\varphi = \theta_g - arctan\,2\,(\tilde{y},\ \tilde{x}). \tag{71}$$

The origin of navigation variables (ρ, α, φ) = (0, 0, 0) coincide with the origin of the error ($\tilde{x}$,$\tilde{y}$,$\tilde{\theta}$) = (0, 0, 0). Then, the kinematic equations in the introduced navigation variables become:

$$\dot{\rho} = -v_1 \cos\alpha, \tag{72}$$

$$\dot{\alpha} = (v_1/\rho)\sin\alpha + (v_2/l), \tag{73}$$

$$\dot{\varphi} = -(v_1/\rho)\sin\alpha. \tag{74}$$

The control law statement is established in Theorem 3.

Theorem 3: Consider the system (72)–(74). Let the control inputs v_1 and v_2 be designed as:

$$v_1 = k_{v,1}\rho\cos\alpha, \tag{75}$$

$$v_2 = tan^{-1}(-l(k_{v,2}\alpha - k_{v,2}(\varphi+\alpha)\tfrac{\cos\alpha\sin\alpha)}{\alpha}). \tag{76}$$

where $k_{v,1}$ and $k_{v,2}$ are the positive gain constants. Then, the origin of navigation variables (ρ, α, φ) = (0, 0, 0) is asymptotically stable.

Proof: Substituting (75)–(76) into (72)–(74) yields:

$$\dot{\rho} = -k_{v,1}\rho\cos^2\alpha, \tag{77}$$

$$\dot{\alpha} = -k_{v,2}\alpha - k_{v,1}(\varphi/\alpha)\cos\alpha\sin\alpha, \tag{78}$$

$$\dot{\varphi} = -k_{v,1}\cos\alpha\sin\alpha. \tag{79}$$

Let a Lyapunov function V_n be chosen as:

$$V_n = (1/2)(\rho^2 + \alpha^2 + \varphi^2). \tag{80}$$

Using (77)–(79), the time-derivative of V in (80) becomes:

$$\dot{V}_n = -k_{v,1}\rho^2\cos^2\alpha - k_{v,2}\alpha^2 \le 0. \tag{81}$$

By Barbalat's Lemma, $\dot{V}_n \to 0$ as $t \to \infty$. This implies that the state ρ,$\alpha \to 0$ as $t \to \infty$. Let the set S_{nav} = {(ρ, α, φ): $\dot{V}$ (ρ, α, φ)= 0}. It can be seen from (78) that $\alpha(t) \equiv 0$ implies $\dot{\alpha}(t) \equiv 0$ and leads to $\phi(t) \equiv 0$. Thus, there is no solution that can stay identically in S_{nav}, except the solutions ρ, α, φ = 0. Based on the LaSalle's Theorem, the origin (ρ, α, φ) = (0, 0, 0) is the largest invariant set and, thus, the origin is asymptotically stable.

5. SIMULATION RESULTS AND DISCUSSIONS

Here, the trajectories calculated by the three control laws, that is, time varying control, sigma-transformed discontinuous control, and navigation-variables-based control, for a forklift driven from an initial configuration (−3, 3, 0) to a goal configuration (0, 0, 0) are evaluated. The configuration of the vehicle is represented by (x, y, θ) (where the unit of x and y is meter and that of θ is radian). It is assumed that the linear velocity and the steering angle can follow their control commands. Small disturbances that are assumed to be the imperfect tracking control in the dynamic model and the slippage in high-speed movement are included in the simulation.

The motion of the forklift using the time-varying-based control law (47)–(48) is shown in Fig. 3 and its trajectories (x, y, θ) are in Fig. 4. The gains are set to $k_{v,1}$ = 3 s^{-1} and $k_{v,2}$ = 1 s^{-1}. The driving velocity v_d and steering angle δ_d are shown in Fig. 5. It is shown in Figs. 3–5 that the time-varying control produces oscillating movements. The convergence rate of the configuration from the initial to the goal is very slow. In this simulation, the goal configuration was reached in 20 s.

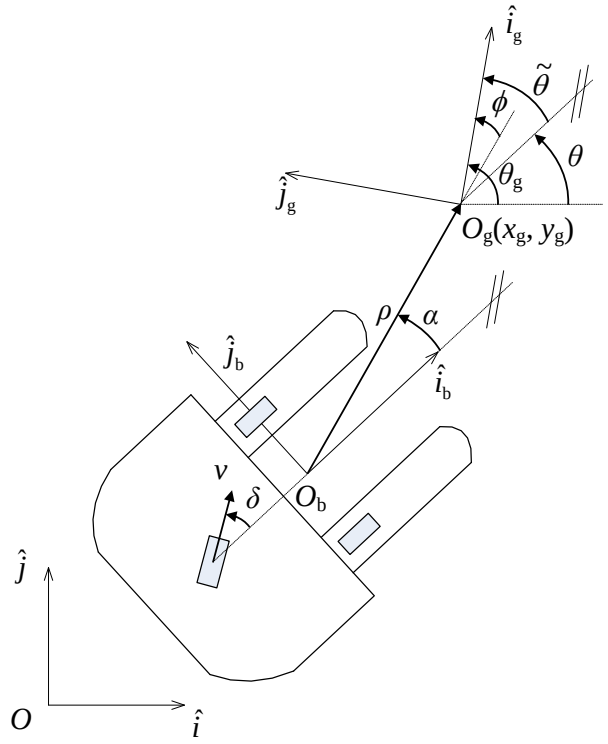

Fig. 2. The navigation variables (ρ, α, φ)

The motion of the forklift using the discontinuous control law (62)–(63) with the gains $k_{v,1}$ = 1 s^{-1} and $k_{v,2}$ = −4 s^{-1}, $k_{v,3}$ = 3 (the eigenvalues are all set to −1) that moves to the goal configuration is shown in Fig. 6. The configuration motion is depicted in Fig. 7. The driving velocity v_d and steering angle δ_d are depicted in Fig. 8. It is observed that the sigma-transformed discontinuous control produces a natural and no oscillations motion. The convergence rate of the configuration from the initial to the goal is also faster than that of the time-varying control law.

In the sigma-transformed discontinuous control, the control signals are discontinues for all points along x = 0. Therefore, the forklift is restricted to achieve the line x = 0 since the control signals are not defined at that line. However, the forklift may approach the goal point (x, y) = (0, 0). The problem in the implementation of discontinuous control, the uncertainties from the sensors or actuators may lead the forklift to the situation where any point along x = 0 is achieved by the forklift. Then, at this point, the control signals may not be determined since the sigma transfor-

DOI 10.2478/ama-2019-0024

mation of (56) is not defined. Moreover, the control signals may be blown up when the vehicle achieve the points where x is very close to zero. This can be seen from the transformation of χ_2'' in (56) the control law v_2'' in (64).

The trajectories of the system calculated using the navigation-variables-based control (74)–(75) are investigated. The gains are set to $k_{v,1}$ = 1 s^{-1} and $k_{v,2}$= 5 s^{-1}. The motion of the forklift, the configuration, and the control inputs (driving velocity v_d and steering angle δ_d) are depicted in Figs. 9–11, respectively. As in the sigma-transformed discontinuous control law, the trajectories generated by the navigation-variables-based control renders a natural and no oscillation motion. The goal configuration was achieved in 6 s.

The difference between the discontinuous control and the navigation-based control lies on the discontinuous points. The discontinuous points of the sigma-transformed discontinuous control are on all points along x = 0, whereas the discontinuous point of the navigation-variables-based control is on one point that is ρ = 0. In the navigation-variables-based control, the forklift may asymptotically converge to the goal point ρ = 0, and accordingly $(\tilde{x}, \tilde{y}) = (0, 0)$. The gains of $k_{v,1}$ and $k_{v,2}$ can be adjusted so that the forklift approaching forward, or in other words, the angles α and φ have already been zero. A switch control at the linear velocity v = 0 can be applied at ρ = 0, so that the forklift has arrived at the desired configuration and the movement is already completed.

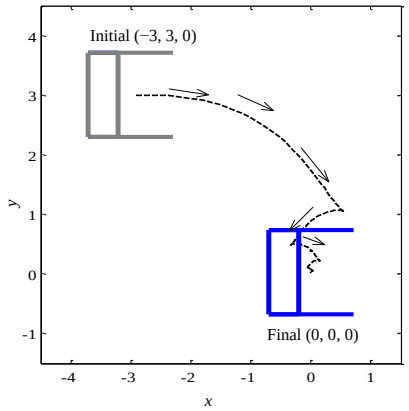

Fig. 3. Motion of the forklift using time-varying control law (48)–(49)

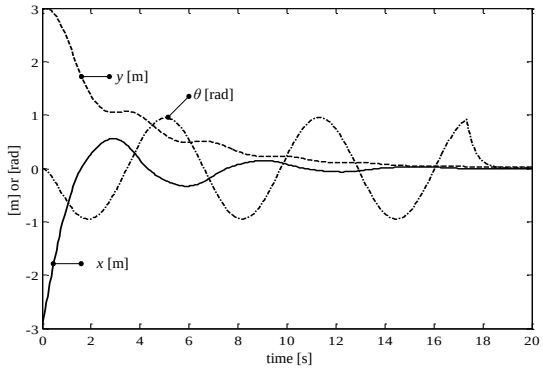

Fig. 4. Configuration motions (x, y, θ) using time-varying control law (48)–(49)

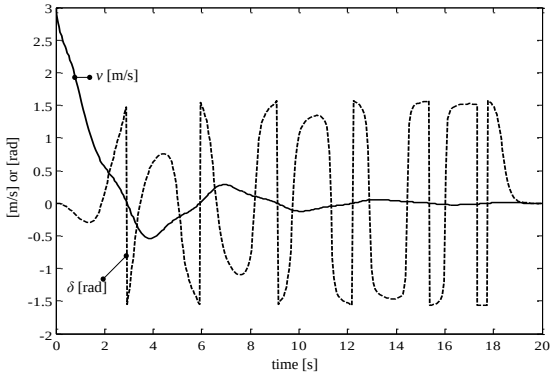

Fig. 5. Linear velocity v and steering angle δ through time-varying control law (48)–(49)

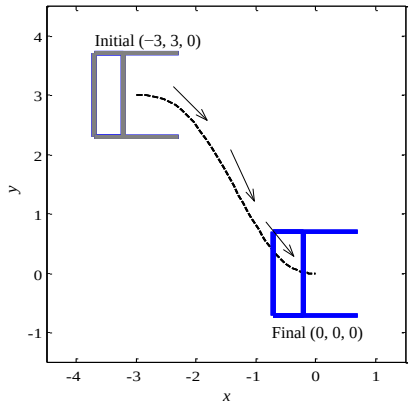

Fig. 6. Motion of the forklift using sigma transformed discontinuous control law (63)–(64)

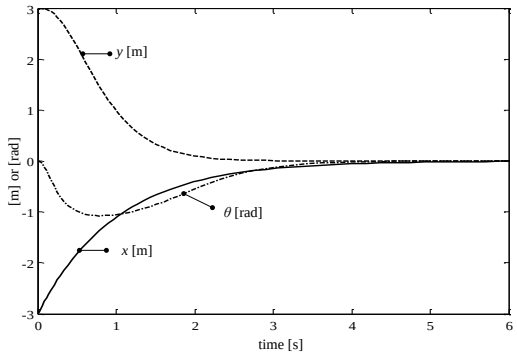

Fig. 7. Configuration motions (x, y, θ) using sigma transformed discontinuous control law (63)–(64)

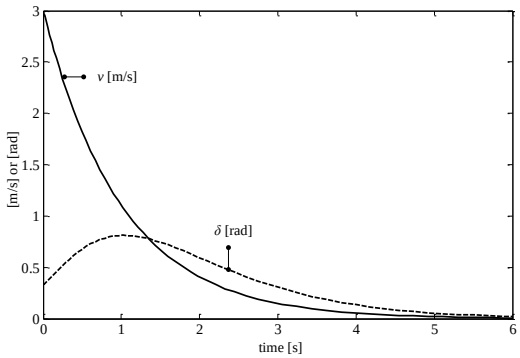

Fig. 8. Linear velocity v and steering angle δ through sigma transformed discontinuous control law (63)–(64)

sciendo
DOI 10.2478/ama-2019-0024

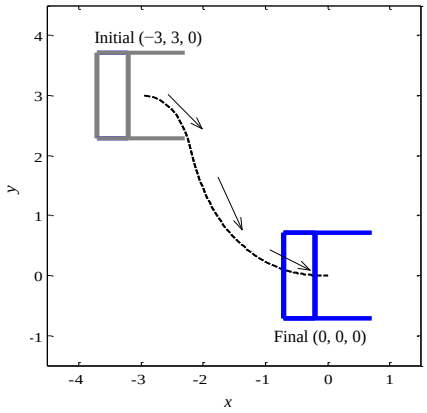

Fig. 9. Motion of the forklift using the navigation-variable-based control law (75)–(76)

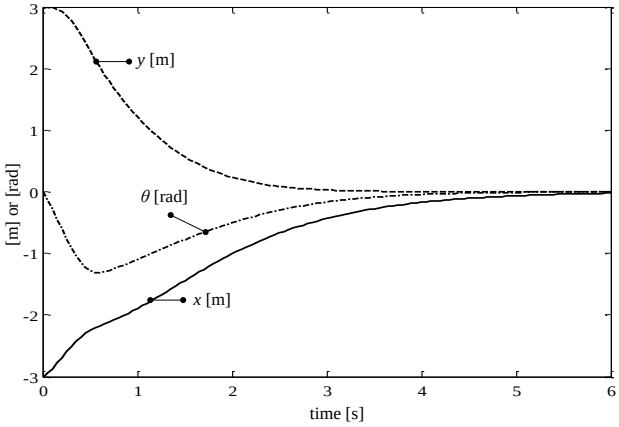

Fig. 10. The trajectories of (x, y, θ) using the navigation-variable-based control law (75)–(76)

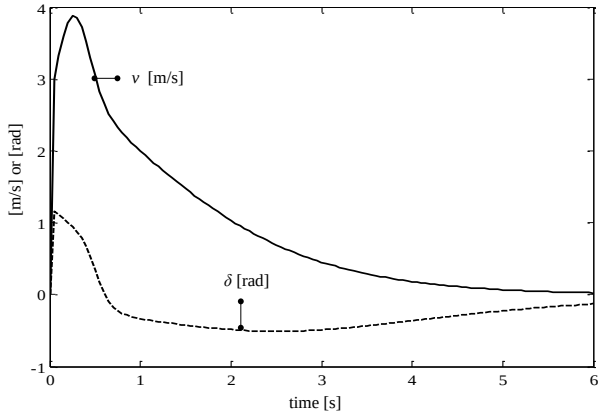

Fig. 11. Linear velocity v and steering angle δ through navigation-variable-based control law (75)–(76)

One problem may occurs when the forklift uses the navigation-variables-based control and starts from the initial point $\rho = 0$ or $(\tilde{x}, \tilde{y}) = (0, 0)$ but the orientation error $\tilde{\theta} \neq 0$. At this point, the navigation-variables-based control is not defined since (73) and (74) are no longer held. To cope with the problem, a check point where $\rho \neq 0$ should firstly be appointed, and the forklift shall be driven away from $\rho = 0$. Then, the initial position changes to the check point where $\rho \neq 0$.

Tab. 1. Comparison of stabilization control of the chained-form, sigma-transformed, and the navigation-based controls

Category	Control algorithms		
	Chained form time-varying control (48)–(49)	Sigma-transformed discontinuous control (63)–(64)	Navigation-variables-based discontinuous control (75)–(76)
Motion	Oscillation	No Oscillation	No Oscillation
Convergence	Slow	Fast	Fast
Control signals	Oscillation	Oscillation	No Oscillation
Discontinuity	No Discontinuity	Discontinue at $x = 0$	Discontinue at $(x, y) = (0, 0)$ or $\rho = 0$.

Moreover, unlike with the sigma-transformed discontinuous control in which the control signals can blow up when the states of the forklift are close to the discontinuous point, the navigation-variables-based control is bounded. This boundedness of the control signals is due to the function of tan^{-1} in (76), which makes the control signal v_2 bounded, $v_2(\rho, \varphi, \alpha) \in (-\pi/2, \pi/2)$ for any argument of $\rho \in [0, \infty)$, $\varphi, \alpha \in [-\pi, \pi)$.

The comparison results of the three control methods that are the chained form time varying, the sigma transformed discontinuous control, and the navigation-variables-based discontinuous controls are summarized in Tab. 1.

6. CONCLUSION

In this paper, the equations of motion of a forklift consisting of kinematic and dynamic equations were derived. The control design of a forklift vehicle was divided into two stages: The kinematic-based control generated the desired linear velocity and steering angle, then the PD control algorithm was used to track the control commands. Three configuration control algorithms that are time-varying, sigma-transformed discontinuous, and navigation-variables-based controls for the forklift were investigated by assuming that the control commands can be tracked perfectly. The time-varying control provided the global asymptotical convergence from an initial to a goal configuration, however, the vehicle exhibited oscillation motion and the convergence rate was extremely slow. On the other hand, the sigma-transformed discontinuous control and navigation-variables-based control provided a fast and smooth motion. The sigma-transformed discontinuous control had discontinuity at all points along $x = 0$. Using this method, the control signals can blow up if the vehicle reaches or is close to $x = 0$. The navigation-variables-based control used navigation variables were not defined at the goal point $\rho = 0$. However, the control signals do not blow up because of the use of the function $\tan^{-1}$. Problems of discontinuity of the navigation-variable-based control at the goal point can be solved by driving the forklift to a check point where $\rho \neq 0$, away from the goal point, and after the forklift achieves that point, the navigation-variable-based control can be implemented and the convergence of the configuration of the forklift is assured.

This conclusion expects that engineers who apply a stabilization control algorithm on a forklift vehicle should consider whether the motion resulted from the stabilization controls is suitable with an application, for instance parking of a car, docking of a forklift, or others. They should be aware of the calculated control signal,

DOI 10.2478/ama-2019-0024

especially in the discontinuous control, whether the control signals may be blown up if the feedback signals come close to the discontinuous point of the controller or not. They should also notice a condition where the designed controller cannot stabilize the concerned vehicle, and a solution that can handle the problem.

REFERENCES

1. **Abbasi W., Rehman F.U., Shah I., Rauf A.** (2019), Stabilizing control algorithm for nonholonomic wheeled mobile robots using adaptive integral sliding mode, *International Journal of Robotics and Automation*, 34(2), 1-8.
2. **Aicardi M., Casalino G., Bicchi A., Balestrino A.** (1995), Closed loop steering of unicycle-like vehicles via Lyapunov techniques, *IEEE Robotics and Automation Magazine*, 2(1), 27–35.
3. **Astolfi A.** (1996), Discontinuous control of nonholonomic systems, *Systems Control Letters*, 27, 37–45.
4. **Baranowski L.M., Siwek L.M.** (2018), Use of 3D simulation to design theoretical and real pipe inspection mobile robot model, *Acta Mechanica et Automatica*, 12(3), 232–236.
5. **Brockett R.W.** (1983), *Differential geometric control theory - asymptotic stability and feedback stabilization*, MA: Birkhäuser.
6. **Hashimoto W., Yamashita Y., Kobayashi K.** (2019), Asymptotic stabilization of nonholonomic four-wheeled vehicle with steering limitation, *IEICE Transactions on Fundamental Electronics, Communications, and Computer Sciences*, E102.A (1), 227–234.
7. **Hespanha J.P., Morse A.S.** (1999), Stabilization of nonholonomic integrators via logic-based switching, *Automatica*, 35(3), 385–393.
8. **Kłosiński J., Janusz J. J., Nycz R.** (2015), The impact of the FLC controller's settings on the precision of the positioning of a payload transferred by a mobile crane, *Acta Mechanica et Automatica*, 8(4), 181–184.
9. **Lamiraux F., Laumond J.P.** (2000), Flatness and small-time controllability of multibody mobile robots: Application to motion planning, *IEEE Transactions on Automatic Control*, 45(10), 1878–1881.
10. **Morin P.C., Samson C.** (2009), Control of nonholonomic mobile robots based on the transverse function approach, *IEEE Transactions on Robotics*, 25(5), 1058–1073.
11. **Muralidharan V., Mahindrakar, A.D.** (2014), Position stabilization and waypoint tracking control of mobile inverted pendulum robot, *IEEE Transactions on Control Systems Technology*, 22(6), 2360–2367.
12. **Murray R.M., Sastry S.S.** (1993), Nonholonomic motion Planning: Steering using Sinusoids, *IEEE Transactions on Automatic Control*, 38(5), 700–716.
13. **Pomet J.-B., Samson C.** (1994), Time-varying exponential stabilization of nonholonomic systems in power form, *Proceedings of the IFAC Symposium of Robust Control Design*, Rio de Janeiro, 447–452.
14. **Ryu J.C., Agrawal S.K.** (2010), Planning and control of under-actuated mobile manipulators using differential flatness, *Autonomous Robots*, 29(1), 35–52.
15. **S'anchez-Torres J.D., Defoort D.M., Muñoz-Vázquez A.J.** (2019), Predefined-time stabilization of a class of nonholonomic systems, *International Journal of Control*, DOI: 10.1080/00207179.2019.1569262.
16. **Samson C.** (1995). Control of chained systems application to path following and time-varying point stabilization of mobile robots, *IEEE Transactions on Automatic Control*, 40(1), 64–77.
17. **Sankaranarayanan V. Mahindrakar A.D.** (2013). Configuration constrained stabilization of a wheeled mobile robot-theory and experiment, *IEEE Transactions on Control Systems Technology*, 21(1), 275–280.
18. **Siegwart R., Nourbakhsh I. R.** (2004), *Introduction to Autonomous Mobile Robot*, Cambridge, MA: MIT Press.
19. **Soueres P., Laumond J.P.** (1996). Shortest paths synthesis for a car-like robot, *IEEE Transactions on Automatic Control*, 41(5), 672–688.
20. **Tamba T., Hong B., Hong K.-S.** (2009), A path following control of an unmanned autonomous forklift. International Journal of Control, Automation, and Systems, 7(1), 113–122.
21. **Tang C. P., Miller P.T., Krovi V.N., Ryu J.-C., Agrawal S.K.** (2008), Kinematic control of a nonholonomic wheeled mobile manipulator - a differential flatness approach, *Proceedings of the ASME Dynamic Syst. Control Conference*, Ann Arbor, Michigan, USA, 2008–2253.
22. **Virgalaivan I., Lipták T., Miková, Ľ.** (2018), Snake robot locomotion patterns for straight and curved pipe, *Journal of Mechanical Engineering*, 68(2), 91–104.
23. **Wang Y., Miao Z., Zhong H., Pan Q.** (2015), Simultaneous stabilization and tracking of nonholonomic mobile robots: A Lyapunov-based approach, *IEEE Transactions on Control Systems Technology*, 23(4), 1440–1450.
24. **Wei S., Uthaichana K., Žefran M. DeCarlo R.** (2013), Hybrid model predictive control for the stabilization of wheeled mobile robots subject to wheel slippage, *IEEE Transactions on Control Systems Technology*, 21(6), 2181–2193.
25. **Widyotriatmo A., Hong K.-S.** (2008). Decision making framework for autonomous vehicle navigation, *Proceedings of the SICE Annual Conference-International Conference on Instrumentation, Control and Information Technology*, Tokyo, Japan, 20-22 August, 1002–1007.
26. **Widyotriatmo A., Hong K.-S.** (2012), Switching algorithm for robust configuration control of a wheeled vehicle, *Control Engineering Practice*, 20(3), 315–325.
27. **Widyotriatmo A., Hong K.-S.** (2015), Configuration control of an autonomous vehicle under nonholonomic and field-of-view constraints, *International Journal of Imaging and Robotics*, 15(3), 126–139.
28. **Xiao H., Li Z., Yang C., Zhang L., Yuan P., Ding, L., Wang T.** (2017), Robust stabilization of a wheeled mobile robot using model predictive control based on neurodynamics optimization, *IEEE Transactions on Industrial Electronics*, 65(4), 3437–3446.
29. **Xie X.-J., Li G.-J.** (2019), Finite-time output-feedback stabilization of high-order nonholonomic systems, *International Journal of Robust and Nonlinear Control*, 29(9), 2695–2711.
30. **Yue M.Y., Ning M. Y., Zhao X., Zong G.** (2019), Point stabilization control method for WIP vehicles based on motion planning, *IEEE Transactions on Industrial Informatics*, 25(6), 3368–3378.

Acknowledgment: This work was supported by Indonesian Ministry of Research, Technology and Higher Education and Institut Teknologi Bandung.

sciendo

DOI 10.2478/ama-2019-0025

acta mechanica et automatica, vol.13 no.3 (2019)

COMMON METHODS IN ANALYSING THE TRIBOLOGICAL PROPERTIES OF BRAKE PADS AND DISCS – A REVIEW

Andrzej BORAWSKI*

*Faculty of Mechanical Engineering,
Bialystok University of Technology, ul. Wiejska 45 C, 15-351 Bialystok, Poland

a.borawski@pb.edu.pl

received 10 May, revised 28 September 2019, accepted 30 September 2019

Abstract: Disc brakes in passenger cars are extremely important due to safety concerns. Their operational quality largely rests on the conditions of contact between the working elements, which mainly consists offlat and dry sliding. The tribological phenomena thatoccur during braking are, unfortunately, extremely complex and difficult to recreate in laboratory settings. Many scientific institutes conduct research to improve our understanding of these phenomena. The results they present make it possible to continuously simplify the procedures for selecting friction materials and reducing the costs of identifying the properties of new products. This article analyses the methods commonly used by researchers. It also presents different set-ups of research stations, as well as the advantages and drawbacks of each method.

Key words: Ball-cratering, pin-on-disc, inertia dynamometer, FE method, brakes

1. INTRODUCTION

The brakes are the most important components of any vehicle as they are responsible for reducing its speed or stopping it completely. This is particularly important in hazardous situations in which the proper action of the braking system may save the health and lives of many road users. The issue is deepened by a continuing tendency to increase the power and torque generated by contemporary automobile engines, which directly corresponds to higher commuting speeds (Szpica, 2015a). This motivates many researchers to conduct studies aimed at improving our understanding of the complicated phenomena, which occur during braking.

Automobiles today primarily use disc brakes. The friction pair in this solution comprises in the brake disc and brake pads (Fig. 1).

Fig. 1. Disc brake friction pair: 1 – brakepads
2 – correspondingbrake disc

During braking, as the pad is pressed against the disc, friction occurs, which transforms kinetic energy into heat. Part of the heat initiates chemical reactions, which may transform or degrade some of the components of the brake pad (such as resin) (Česnavičius et al., 2016; Kilikevičius et al., 2016). Most of the remaining energy, in the form of heat, is then released into the atmosphere (Blau and McLaughilin, 2003; Borawski, 2016). A wide range of research, mainly simulations, is being conducted in order to determine the amount of energy involved in the process, as well as its displacement among different parts of the system (Adamowicz, 2016; Yevtushenko and Grześ, 2015b). This is mainly because the design of the braking system makes direct measurements considerably difficult.

The process of braking is largely affected by the tribological properties of discs and pads. The former are commonly made from grey cast iron, as it is characterised by good thermal conductivity and anti-vibration capacity (Maluf et al., 2007). Newest disc solutions, especially in sports cars, utilise composite materials based on ceramics (Schmidt et al., 1999). Matters are different for brake pads. Their structure is far more complicated. Brake pad makers use approximately 2000 different materials (Blau, 2001), which have various effects on the final product. An average brake pad is made from 10 to 20 different substances. Selecting the right composition for the brake pad and predicting its impact on the final products is a difficult task. It requires prototypes and tremendous amounts of research and abundant experience (Nagesh et al., 2014). The decision must also take into account the intended use of the brake pad, and their operating conditions. The final properties of the brake pad are also shaped by production technology, which is usually the best kept trade secret of every manufacturer. Effective production technology may improve the tribological properties of the brake pad by 100% (Nicholson, 1995; Patel and Jain, 2014).

2. CLASSIFICATION OF RESEARCH METHODS

Contemporary technological advancement makes it possible to use various research techniques in many different ways producing more or less accurate results (Walliman, 2010). Also,

DOI 10.2478/ama-2019-0025

every method consumes certain costs and time necessary to conduct the tests (Dundulis et al., 2012; Mieczkowski, 2019). In terms of passenger cars and their parts and components, based on the above mentioned criteria, the main types of research consist of(Axén et al., 2001; Sikder, 2014):

- road tests – thetest involves a vehicle in its entirety (which is why the test is expensive, time-consuming, and difficult to perform) moving in a natural setting, producing the best quality results;
- bench tests – slightly less expensive, but also involving a complete vehicle. The research conditions are set artificially by, for example, regulating temperature, humidity, or air flow;
- complete component tests – the test involves a single component of the car in a controller, repeatable setting (such engine tests in a dynamometer);
- parts tests – focusing on selected properties of individual parts, such as the brake disc or pad;
- model tests – a process aimed at fast and inexpensive research, for example, for comparative purposes; model tests are used when there is no possibility of testing a complete part, or when the research is restricted by cost or time limitations, or requires a fully controllable test setting.

The friction elements in brakes are susceptible to different types of wear. The most common type of wear is abrasion, the deterioration of the surface layer of friction elements moving against each other (Varinauskas et al., 2013). The loss of the pad's material is caused by separation of particles due to scratching, micro grinding, and the formation of grooves (Zmitrowicz, 2006). This type of wear is the main focus of this work. The most important criterion for categorising the research methods used in determining the abrasive wear parameters is the macrogeometry of the contact between the sample and the counter-sample. This is an important design feature in equipment used in measuring the coefficient of friction and wear rate.The following solutions are most common (Bhushan, 2002; Hoehn et al., 2008; Hussein, 2015):

a) point contact (ball-disc, Fig. 2a), used in ball-cratering
b) line contact (cylinder-disc, Fig. 2b), used in pin-on-disc,
c) surface contact (surface to surface, Fig. 2c), used in inertia testbeds.

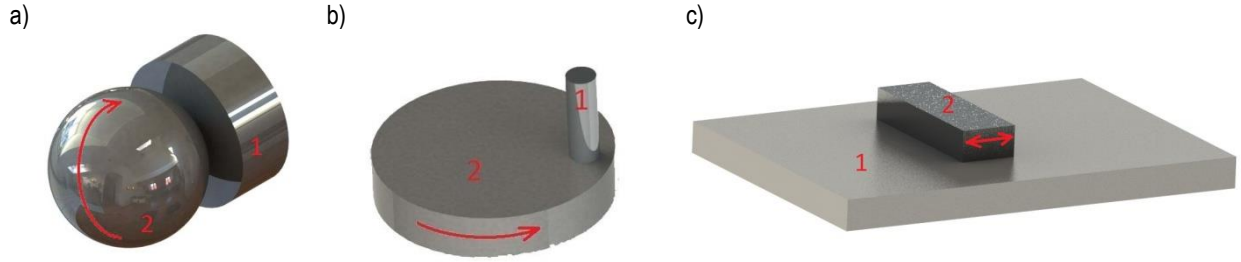

Fig. 2. Commonly used macrogeometric friction pair contact sites: a– point contact, b– line contact, c– surface contact, 1– stationary element, 2– moving element

Finding the appropriate test method is difficult. Each method presented above makes it possible to measure the force of friction (or the coefficient of friction) and the wear rate. Different types of contact, however, produce significantly varying results, which are also far from reality (Adachi and Hutchings, 2003 and 2005). The issue is partially solved by standardising the test samples and conditions (Dumbleton, 1981). Still, a decent knowledge of tribometers is necessary to select the most appropriate measuring system. It is also necessary to fully analyse the actual process to be recreated in the test station. This allows for a proper representation of the necessary real-life conditions, as only then does test make sense (Stachowiak et al., 2004).

The main aim of the article is review and comparison of friction materials' test methods.

3. RESEARCH METHODS AND THEIR MAIN FEATURES

Ball-cratering is a test thatthe friction pair consists of in a cylindrical sample (1" in diameter, 10 mm high) and ball (also 1" diameter) (Osuch-Słomka, 2012). The method was designed to study micro-wear of ceramic coatings, but as the conducted research demonstrates – it may be successfully applied to other industries for testing metals and non-metals (Priyana and Hariharan, 2014; Mergler and Huis't Veld, 2003; Bello and Wood, 2005). This is made possible by the numerous advantages of this method, including a decent result reproducibility and short time of individual tests. Depending on the researchers' requirements, it is possible to run the test with a lubricating or cooling agent, or any other liquid occurring in natural conditions (Cozza, 2014).

Many companies manufacture work stations for ball-cratering, with all sharing certain elements. Fig. 3 presents a diagram of a ball-cratering station, a T-20 model made in Poland. This equipment places the sample (1) in the holder of a vertical arm on a rotating lever and its weight is equated by a counterweight (7) placed on the other side of the horizontal lever arm. The other side of the lever has a scale for placing the load (5) in order to press the sample against the counter-sample. The lengths of the arms of the rotating levers are equal, meaning that the downforce is equal to the set pressure of weights on the scale. The counter-sample is mounted on a shaft of an electrical motor (8) (with regulated speed). The strain gauge (4) located above the sample holder makes it possible to monitor the force of friction directly during the test.

The rotating ball grinds against the sample. Its vertical position allows the removed material to drop freely, preventing it from interfering with the test (Cozza et al., 2009). The friction creates a crater, which is measured in two dimensions to determine a mean diameter, and then to determine the abrasive wear rate coefficient (K_c) using the Archard equation (Osuch-Słomka, 2011) (Fig. 4 presents examples of craters and methods for measuring the diameter). The station measures friction in real-time, making it possible to easily calculate the coefficient of friction for the pair.

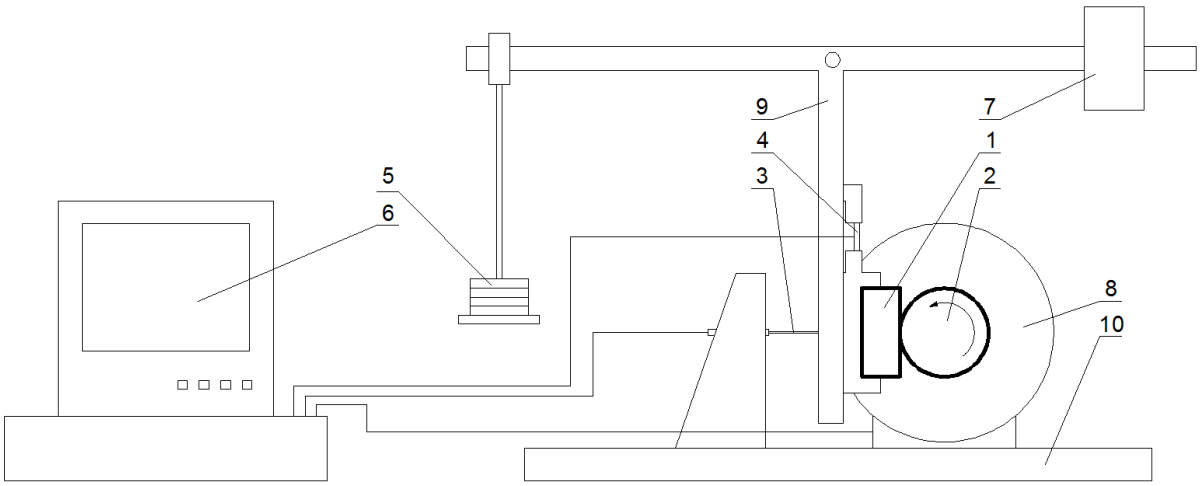

Fig. 3. T-20 test station diagram: 1 – sample, 2 – counter-sample (ball), 3 – displacement sensor, 4 – strain gauge for measuring friction, 5 – weights, 6 – computer, 7 – counterweight, 8 – electrical motor, 9 – rotary arm, 10 – base

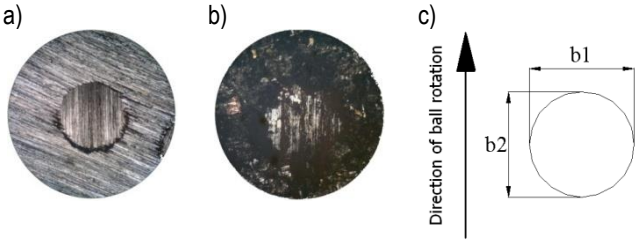

Fig. 4. Craters formed during tests on: a– brake disc, b– brake pad, c– diameter measurement method

Unfortunately, the structure of a brake pad and the actual nature of the contact between the pad and the disc (Eriksson et al., 2002; Bouchetara and Belhocine, 2014) make the ball-cratering test not the best-suited method in the discussed example. Point contact produces the risk of studying not the tribological properties of a complete brake pad, but rather focusing on the properties of one of the pad's many components. That is why every test could yield different results. Some researchers suggest applying unusual methods, such as using rubber balls (counter sample) and pressing the two test samples against the ball (Fildes et al., 2012) or submerging the friction pair in an abrasive slurry (Shipway and Hogg, 2007). Although it was demonstrated that these methods improve the reproducibility of results, this type of tests do not reflect the actual operating conditions of the braking pair and have no application in their research. The crux in obtaining quality test results may lie in planning the experiment properly. This, unfortunately, is very time consuming (Szpica, 2016, 2018, Mieczkowski, 2017). Although many experiment planning methods have been developed, the one most frequently used for these types of measurements is the Taguchi method for process optimisation (Gee et al., 2003; Osuch-Słomka et al., 2013). This method makes it possible to determine the boundary conditions for a specific experiment, that is, the load, speed, and friction distance. The operation, coupled with an appropriately high number of samples, produces correct results corresponding to actual conditions.

Tab. 1. Main advantagesand disadvantages of Ball-cratering

Advantages	– good reproducibility of results – short time of individual experiments – tests can be performed in the presence of, for example, lubricating agents – low costs of experiments
Disadvantages	– necessity of using additional equipment to measure the craters – complicated experiment planning process – point contact between the friction pair, which in the case of brake pads requires the performance of numerous tests – the type of contact does not reflect the actual operating conditions of brakes – no possibility of observing the complex mechanisms of braking

Pin-on-disc is a test that studies friction and wear in sliding conditions. It is used for recreating the linear contact macrogeometry of the sample and counter-sample. The method may be applied in tests on dry fiction and with the use of lubricants (Kaleli, 2016; Nuraliza et al., 2016). With the use of an environmental chamber, the experiments can be conducted in the presence of various gasses or changing humidity (Tamboli and Sheth, 2008). The pin-on-disc method makes it possible to determine the average coefficient of friction between a friction pair, and evaluating the wear rate of the friction surfaces. The first parameter is measured directly during the experiment as a function of time or number of disc rotations, while the second parameter is determined on the basis of the change (loss) of weight of the sample. The necessary data is obtained by weighing the sample before and after the test. Of course, the sample has to be carefully cleaned before weighing using products like acetone or washing benzene. Otherwise the results may be seriously flawed (Li et al., 2016; ASTM G99-17, 2017; Ramesh et al., 2015; Nair et al., 2009).

In most stations, the disc revolves on a vertical surface (Fig.5a), although there are instruments in which the disc is

DOI 10.2478/ama-2019-0025

placed vertically (Kucera and Prsan, 2008) (Fig. 5b). Due to similarities to a disc brake, the stations with a vertical rotation axis are well suited for testing brake discs and pads. As with ball-cratering, placing disc horizontally makes the pin slide on loose sample fragments torn away during the experiment. That is why, the same material may yield different end results in several experiments (Trzos, 2010). Despite all this, this setting of the pin-on-disc method is frequently used in testing samples of brake pads (Surojo et al., 2015; Gopal et al., 1994; Elakhame et al., 2017; Sugözü and Dağhan, 2016; Nosko et al., 2017).

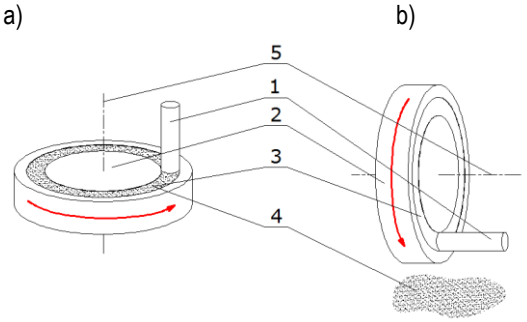

Fig. 5. Different pin and disc settings: a– vertical disc rotation axis, b– horizontal disc rotation axis, 1– pin, 2– disc, 3– sign of wear, 4– fragments loosened during abrasive wear, 5– disc rotation axis

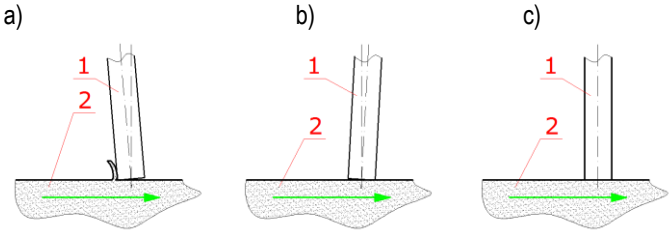

Fig. 6. Friction pair operation in the pin-on-disc method: a– positive pin pitch resulting in grinding, b– negative pin pitch resulting in sliding against the sample surface, c– correct contact, 1– stationary pin, 2– spinning disc

It is essential to position the pin correctly against the disc (at a right angle - Fig. 6c). Even slight variation may interfere with the experiment, as it is easy to grind the surface of the sample (Fig. 6a), or slide against it (fig. 6b) (Blau, 2014; Pauschitz et al., 2005). The problem may be avoided by preparing the pin properly. One way to do it is to set up the station and initially cover the contact surface with sanding paper. The disc then rotates until the contact surface with the pin is evened out. Any possible irregularities become levelled, providing correct contact between the friction pair (Uyyuru et al., 2007). Another solution is to use pins without a flat tip, such as ball-ended pins, or using balls instead of pins (using the ball-on-disc method) (Li et al., 2013). These methods differ greatly from the real-life contact between disc and pad, and therefore, are not recommended for testing the working elements of braking systems.

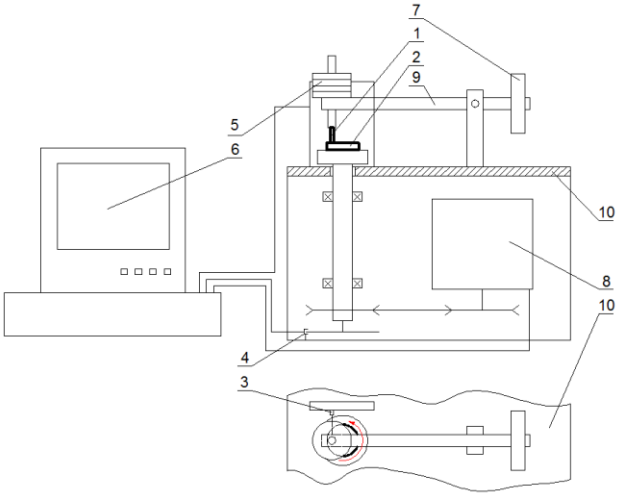

Fig. 7. Pin-on-disc test station diagram: 1 – stationary pin, 2 – spinning disc, 3 – strain gauge for measuring friction, 4 – rpm sensor, 5 – load, 6 – computer, 7 – counterweight, 8 – electrical motor, 9 – rotary arm, 10 – body

Figure 7 presents a diagram of a T-11 pin-on-disc test station made in Poland. The stations may differ slightly among manufacturers, general operating principle remains the same. The pin (1) is placed on a lever (9) preventing it from moving. The lever is fastened to the body of the station, but may rotate (10). The body holds an electrical motor (8), which uses a gear to spin the shaft with an rpm sensor (4). The second element of the friction pair, the disc (2), is attached to the shaft. Due to friction, the lever (9) tilts and deforms the strain gauge (3), which registers the friction. Some stations have the strain gage installed directly on the rotary arm (9). Appropriate downforce is provided by weights (5) placed directly above the pin. Rotation speed is regulated manually or using the computer (6), which also records the experiment. If necessary, the station can be furnished with an infrared sensor (e.g., thermo-vision camera (Zdravecká et al., 2013; Rowe et al, 2013) or a thermocouple with a probe located in the pin (Dwivedi, 2002) for temperature monitoring.

Tab. 2. Main advantages and disadvantages of pin-on-disc

Advantages	– contact geometry of friction pair close to the actual cooperation between brake disc and pad – tests can be carried out in the presence of, for example, lubricating agents – low cost – short time of experiment
Disadvantages	– additional equipment required for measuring loss of mass – in the case of horizontal rotation axis, the fragmented material remains on the friction surface, impairing test results – the pin must be placed very carefully against the disc – no possibility of observing the complex mechanisms of braking

Inertia dynamometry used for testing the working components of braking systems, the discs and pads. Thanks to their special designs, a complete disc and two pads can be installed in the station (in a factory made calliper, from a specific car model). This is a test method allowing macrogeometry tests in surface-to-surface settings (Hagino et al., 2016). Thanks to the measurements made in a setting closely resembling real (road) conditions, this is the best method presented so far, as it allows obtaining real results (Telang et al., 2016), and is cheaper and less time-consuming than road tests with an entire vehicle (Sarkar and Hirani, 2015). That is why this method is commonly used in the development of new friction materials for brake systems (Tsang et al., 1985). Extensive procedures were developed to determine the course and boundary conditions of experiments in order to standardise testing. Unfortunately, they only take into account emergency situations and do not reflect the every-day of a brake system (Min-Soo, 2011; Grochowicz et al., 2014; Czaban and Szpica, 2013). Recreating the changing conditions of braking is also an issue. There have been attempts at using sufficiently powerful motors with adjustable speed, but this brought about the problem with measurement accuracy (Wu et al., 2009).

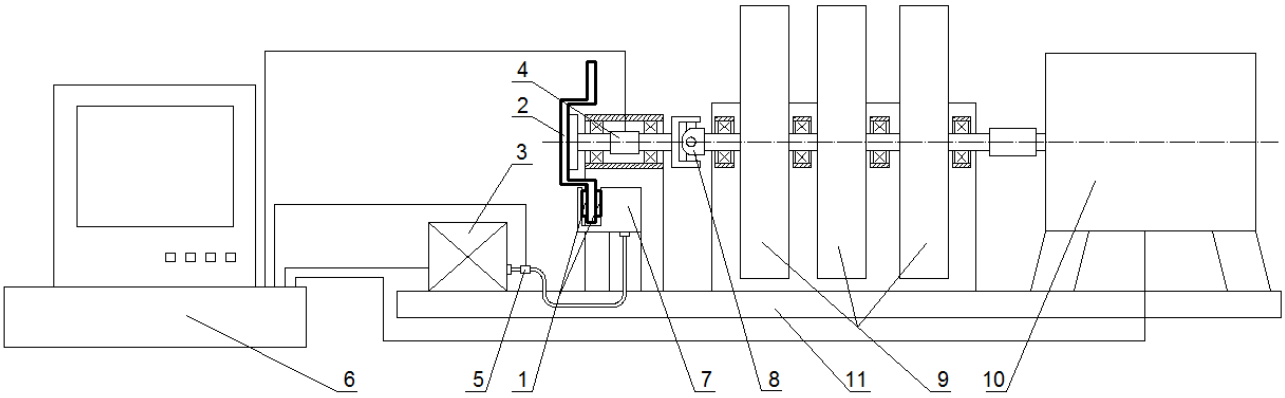

Fig. 8. Diagram of an inertia dynamometry station: 1– brake pads, 2– brake disc, 3– hydraulic piston, 4– torque and speed monitor, 5– pressure sensor, 6 – computer, 7 – brake calliper, 8 – cardan joint, 9 – rotational mass, 10 – electric motor, 11 – base

Figure 8 presents a diagram of a typical test station. Here, the disc (2) is attached to the hub. Rotation is provided via the electric motor (10), which also propels the rotational mass (9). Depending on the manufacturer and intended use, the station may be equipped with one or more rotational masses. These serve as energy accumulators stimulating the inertia of a vehicle during braking. Depending on the properties of the simulated vehicle, the mass is adjusted by adding or removing weights (Min-Soo et al., 2010). The speed can also be adjusted in order to simulate different braking scenarios. When the desired speed is reached, the motor is disconnected and the measurement begins. Braking is provided by the calliper (7) to which the brake pads are attached (1). The calliper is powered by a hydraulic pump (3). Pressure is monitored throughout the experiment (5), which can be used for calculating the normal force in the friction pair. The braking torque is measured by the torque sensor (4) located on the shaft connecting the disc hub and rotational mass. Everything is controlled by a computer (6), which also records the course of the experiment. Similar to the pin-on-disc method, the station can be furnished with temperature measuring sensors. Usually,thisfunction is performed usinga thermal camera, sometimes – using a thermocouple (Balotin and Neis, 2010). Sometimes inertia stations are used to study the chemical compounds released to the environment during brake pad wear. Clearly, this type of testing requires additional instruments such as a sealed body, fan forcing air movement, and set of filters for air exhausted from the test station during the experiment (Matejka et al., 2017).

Tab. 3. Main advantages and disadvantages of inertia dynamometers

Advantages	– thanks to the possibility of testing complete sets of discs and pads, this method best reflects the real conditions of braking – allows (to a degree) testing of complex processes recreating the braking process, such as change of contact pressure throughout the experiment
Disadvantages	– the method is standardised, accounting for only extreme situations – recreating complicated, changing conditions of braking is problematic – significant cost purchasing or building the test station, resulting in high total cost of research in comparison to the methods described above – lack of linear regulation of rotational mass – the mass is increased by adding weights with a specified mass, therefore, the change is non-gradual

Simulations of braking systems or their components are currently a very popular research method. Their popularity stems from low costs in comparison to the other tests, as the only requirement is a computer with some specific software. Unfortunately, while the other methods do not require precise knowledge of phenomena occurring in the studied process, in simulations, this is a necessity(Mieczkowski et al., 2007; Szpica, 2015b). Without detailed knowledge of the phenomena and their relationships, all described mathematically, and without abundant material data (such as density, thermal conductivity, heat capacity, etc.), it is impossible to conduct a simulation, and even the smallest error may flaw the end results (Borawski, 2018; Yevtushenko, 2014). It

DOI 10.2478/ama-2019-0025

is also difficult to simulate the workmanship imperfections or the heterogeneous structure of the brake pad material, resulting from sintering. Still, many researchers conduct simulations not only for brake discs and pads, but also in terms of other brake components such as valves (Kamiński and Kulikowski, 2017), hoses (Kaminski, 2017), pumps (Geromel, 2014), and complete braking systems (Khot and Borah, 2015), or even entire engines (Puławski and Szpica, 2015).

An interesting alternative to simulations is constructing mathematical models and using them to simulate the test stations described above. These models are most commonly used for the pin-on-disc method. One of the biggest advantage of such an approach is the possibility of verifying the results obtained in the model against a real working station. Authors of such models claim that upon a successful verification, the model can completely replace experiments conducted on the test station, which significantly reduces the time of research and lowers the cost to a minimum. Additionally, such models provide the possibility of examining values, which are either difficult or impossible to measure on a real test station, such as pressure distribution on the contact surface between the friction pair (Chmiel, 2008; Perez et al., 2011; Yan et al., 2002; Abdullah and Schlattmann, 2016). This methodology can be used successfully in the development of new brake pad compositions.

There is a large group of researchers analysing temperature distribution in the working elements of brakes using FEM. This type of research is important because conventional measurements are extremely difficult or quite impossible in some cases (e.g., in the friction pair). Using a computer, researchers are able to determine exactly how the temperature is distributed both in the disc and in the brake pad (Adamowicz, 2017; Grzes, 2017; Talati and Jalalifar, 2009), and they can also change the starting conditions of the test, such as the car's speed during braking, or the clamping force between the friction surfaces (Yevtushenko et al., 2017; Yevtushenko and Grześ, 2015a; Yevtushenko and Grześ, 2016). Unfortunately, due to the reasons described earlier, the results of simulations are difficult to verify experimentally. Some researchers tried using thermal cameras, yet the specificity of the disc surface may yield some measurement disturbances (Richard, 2004).

Computer software using FEM make it possible to evaluate the tension both on the surface of the studied pair, as well as underneath. Since this tension is generated by expanding materials, the obtained results are in a way an expansion on simulation thermal tests (Dakhil et al., 2014; Belhocine and Bouchetara, 2014). It is also possible to measure the distribution of pressure along the contact surface of the friction pair, or the abrasive wear rate of a brake pad. These models, however, require expanding the virtual environment with pistons, and even full callipers in some cases, and involve certain simplifications, like assuming that the disc is a rigid structure thatdoes not wear (Abubakar et al., 2006; Rashid and Strömberg, 2013; Abebaw, 2015; Söderberg and Andersson, 2009).

Tab. 4. Main advantages and disadvantages of simulations

Advantages	– lowest cost of all of the research methods presented here – no specialist instruments required – full control over test conditions (such as ambient temperature, pressure, friction pair sliding speed) – extensive universality making it possible to test practically any element and any phenomenon, provided that it be described mathematically
Disadvantages	– requires knowledge of advanced mathematics, thermodynamics, physics, and chemistry – necessary simplifications deteriorate the reflection of reality – in some cases, lack of result verification, as the tested parameter is unmeasurable or difficult to measure

4. SAMPLE RESEARCH RESULTS

In order to check how the methods described above work in the friction material testing process, ball-cratering, pin-on-disc and computer simulation tests were performed. As a test object, brand new brake pads of a popular passenger car were used. Samples of various sizes were cut from the pads to fit into the laboratory stands. Grey cast iron was used as a counter-sample. The laboratory tests were carried out at air humidity of35% and ambient temperature of 21°C. These parameters were measured using a MT886 hygrometer and a type K thermocouple connected to a Velleman DEM106 sensor.

Ball-cratering: As already mentioned, in this method, it is important to properly plan the experiment. For this purpose, the method described in previous publications was used (Borawski, 2016; Borawski and Tarasiuk, 2018). The input parameters of the experiment thus determined are: load: 0.6N, distance: 150 m, speed of rotation: 150 rpm; therefore, total time of the experiment was 752s. The recording of the friction force value (Ft) carried out during the experiment (Fig. 9) allowed the determination of the friction coefficient, which equals 0.41.

In addition, measuring the size of craters allowed the calculation of the coefficient of abrasive wear rate from the Archard's equation:

$$K_c = \pi \frac{b^4}{64RSQ} \quad (1)$$

where b is the arithmetic mean of the measurements of the crater diameter in the direction of sphere rotation and in the perpendicular direction, R- radius of the counter-sample, S- friction distance, Q- load. In the considered method, the Kc coefficient value is 4.138·10-13 mNm-3.

Pin-on-disc: In this study, a T-11 stand was used. The parameters for the experiment were as follows: velocity v = 1 m/s, path S = 1000 m, touch diameter d=18 mm, and load Q = 5 kg; so, the total time of the experiment was 1000 s. The parameter recorded during the tests, as in the previous experiment, was the value of friction force (Fig. 10). It was used to calculate the coefficient of friction of cooperating materials. The calculation result revealed a friction coefficient of 0.38.

DOI 10.2478/ama-2019-0025 acta mechanica et automatica, vol.13 no.3 (2019)

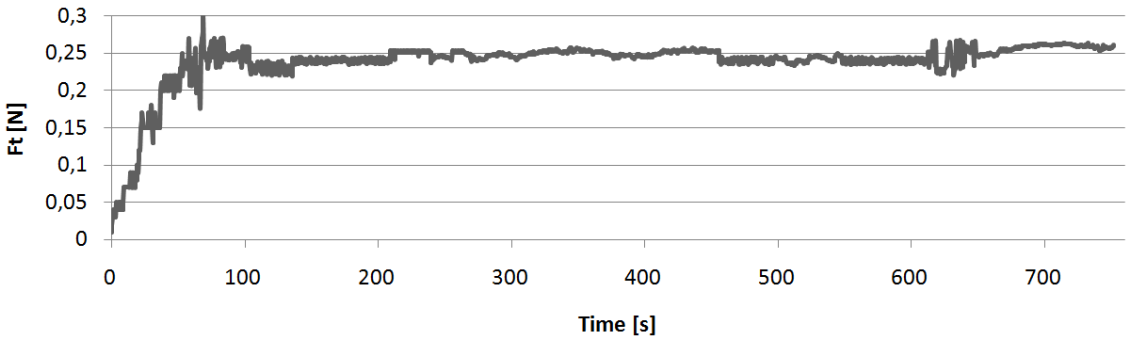

Fig. 9. Example time profile of the friction force obtained during ball-cratering test

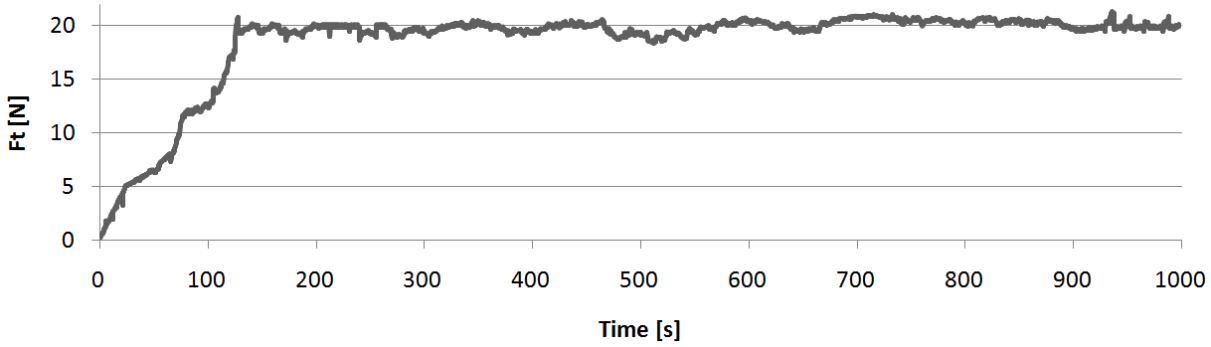

Fig. 10. Example time profile of the friction force obtained during pin-on-disc test

In addition, the sample was weighed before and immediately after testing. Before that it was thoroughly cleaned. The weight loss was 0.69896 g, while the volume loss was $2.4525 \cdot 10^{-5}$ m^3. These quantities allowed to determine the coefficient of abrasive wear rate. The Archard's equation was used to calculate the $K_c$value, but in a slightly different form:

$$K_c = \frac{S \cdot Q \cdot g}{V} \quad (2)$$

where: V - volume of wear material [m^3], g - gravitational acceleration. The obtained result is K_c=$3.917 \cdot 10^{-13}$ mNm^{-3}.

Simulation tests: In the simulation, the previously developed mathematical model was used (Borawski, 2018a; Borawski 2018b). It was assumed that a vehicle with a mass of 1500 kg (with tires 205/55/R16) will be braked from an initial speed of 90 km/h. The result of braking is a complete stop of the vehicle. It was also assumed that the tire coefficient of friction to the road is 1.0, which gives a constant delay of 9.81 m/s2. The coefficient of friction of the pad against the disc was assumed averaged from the values obtained in the tests described above, i.e. 0.395. The ambient air temperature was set to be 27°C. In addition to the above, the following assumptions were made:

- invariability of friction coefficients,
- constant and equal contact pressure for both pads,
- homogeneity of the pad material and contact with the entire surface,
- constant braking delay,
- no influence of external factors (e.g., road unevenness, air resistance).

The properties of friction materials necessary to perform the simulation were experimentally determined and summarized in Tab. 5.

Simulation tests were carried out using FEM. The model with the mesh (which consisted of about 6,200 elements, mostly of triangular shape, which gave nearly 32,000 degrees of freedom) is shown in Fig. 11.

The results of the tests were the temperature profiles of the disc and the pads. Temperature was gauged attwo points: in the geometrical centre of the braking pad at 0.2 mm from its surface (Fig. 12) and at 0.2 mm from the surface of the disc at the opposite side, after turning it by 180 ° (Fig.13).

Tab. 5. Material properties of the sample and counter sample.

	Sample	Counter sample
Thermal conductivity	150 [W/(m*K)]	47 [W/(m*K)]
Density	2860 [kg/m^3]	7870 [kg/m^3]
Heat capacity at constant pressure	1050 [J/(kg*K)]	498 [J/(kg*K)]

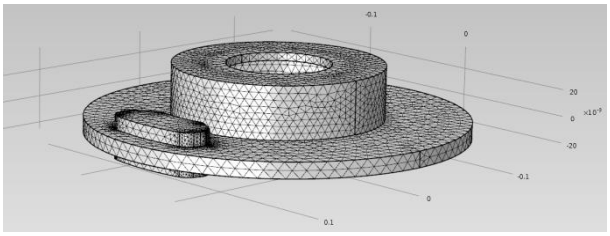

Fig. 11. A simplified model of the disc and pads with the mesh applied

In addition, the research showed that during braking under the conditions assumed above 73801 W of thermal energy will be produced.

DOI 10.2478/ama-2019-0025

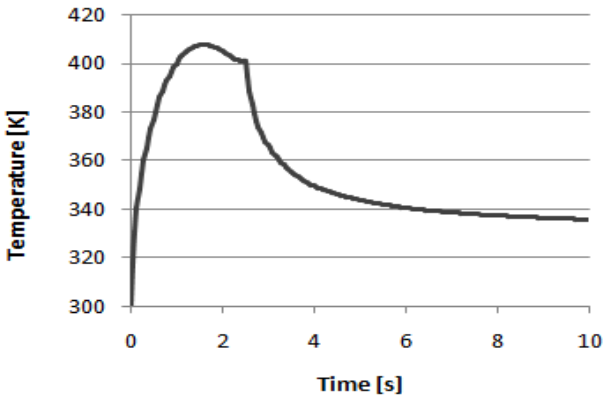

Fig.12. Brake pad temperature

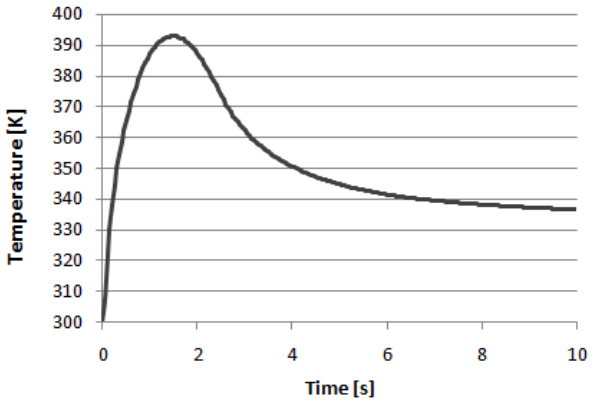

Fig.13. Brake disc temperature

Analysing the obtained results, the statement can be risked that with proper planning, ball-cratering and pin-on-disc methods can be used interchangeably. Simulation tests in turn can be treated as their development, allowing to examine parameters that are very difficult or impossible to measure.

5. CONCLUSIONS

The process of vehicle braking is very complex. The high temperatures thataccompany it may lead to various tribochemical reactions, including oxidation of metallic components (Polajnar et al., 2017), formation of new alloys (Matejka Et al., 2011), or even thermal degradation of the brake pad binder. Damaged resin (the most common brake pad binder) causes the contact layer of the brake pad to become brittle (Placha et al., 2017; Cai et al., 2015). This results in radical changes in the material's tribological properties. Unfortunately, these conditions are not easily recreated, making laboratory tests or simulations of brake pads troublesome. Moreover, in real-life settings, there is always surface contact between the friction materials. This is because the contact surface undergoes elastic or even plastic deformation, which is not always reflected in experimental settings. Development of a research method thattakes into account the disturbances occurring in road conditions (such as wheel rotation speed change corresponding the varying tire rigidity (Kulikowski and Szpica, 2014) and building a suitable test station would likely involve costs and difficulties, which could not be borne by most institutions. That is why, many researchers must compromise and choose a method thattakes into account certain simplifications in their experiments, making their test results, to a greater or lesser degree, flawed.

REFERENCES

1. **Abdullah O. I., Schlattmann J.** (2016), Temperature analysis of a pin-on-disc tribology test using experimental and numerical approaches, *Friction*, Vol. 4, No. 2, 135–143.
2. **Abebaw H. S.** (2015), *Analytical and Finite Element Analysis of Surface Wear on Disc Brake Rotor* (Ph.D. thesis), Institute Of Technology, Addis Ababa University.
3. **Abubakar A. R., Li L., James S., Ouyang H.** (2006), Wear simulation and its effect on contact pressure distribution and squeal of a disc brake, in: *Proc. of the International Conference on Vehicle Braking Technology IMechE*.
4. **Adachi K., Hutchings I. M.** (2003), Wear-mode mapping for the micro-scale abrasion test, *Wear*, Vol. 255, No. 1–6, 23–29.
5. **Adachi K., Hutchings I. M.** (2005), Sensitivity of wear rates in the micro scale abrasion test to test conditions and material hardness, *Wear*, Vol. 258, No. 1–4, 318–321.
6. **Adamowicz A.** (2016), Finite element analysis of the 3D thermal stress state in a brake disk, *Journal of Theoretical and Applied Mechanics,* Vol. 54, No. 1, 205–218.
7. **Adamowicz A.** (2017),Thermal stress state of the pad-disc tribosystem ad single braking, *Journal of Friction and Wear,* Vol. 38, No. 2, 24–30.
8. ASTM G99-17 (2017), *Standard Test Method for Wear Testing with a Pin-on-Disk Apparatus*, ASTM International, West Conshohocken, PA.
9. **Axén N., Hogmark S., Jacobson S.** (2001), *Modern Tribology Handbook, Chapter 13: Friction and Wear Measurement Techniques*, CRC Press, 493–511.
10. **Balotin J. G., Neis P. D.** (2010), Analysis of the influence of temperature on the friction coefficient of friction materials, in: *Proc. ABCM Symposium Series in Mechatronics*.
11. **Belhocine A., Bouchetara M**. (2014), Structural And Thermal Analysis Of Automotive Disc Brake Rotor, *Archive Of Mechanical Engineering*, Vol. 61, No. 1, 89–113.
12. **Bello J. O., Wood R. J. K.** (2005), Micro-abrasion of filled and unfilled polyamide 11 coatings, *Wear*, Vol. 258, No. 1–4, 294–302.
13. **Bhushan B.** (2002), *Introduction to Tribology*, John Wiley & Sons Inc., New York.
14. **Blau P. J.** (2001), Compositions, Functions and testing of friction brake materials and their additives, *Oak Ridge national laboratory report no.19*, Tenessee: US Department of Energy.
15. **Blau P. J.** (2014), The use and misuse of the pin-on-disk wear test, in: *Proc. STLE Annual Meeting*, Florida.
16. **Blau P. J., McLaughlin J. C.** (2003), Effect of water films and sliding speed on the frictional behavior of truck disc brake materials, *International journal of Tribology,* Vol. 36, 709–715.
17. **Borawski A.** (2016), Suggested research method for testing selected tribological properties of friction components in vehicle braking systems, *Acta Mechanica et Automatica,* Vol. 10, No. 3, 223–226.
18. **Borawski A**. (2018a), Simulation study of the process of friction in the working elements of a car braking system at different degrees of wear, *Acta Mechanica et Automatica*, Vol.12, No. 3, 221–226.
19. **Borawski A.** (2018b), Simulation studies of passenger car brake system elements heating process under various braking parameters, *Proceedings of 23nd International Conference MECHANIKA-2018*, 58–61.
20. **Borawski A., Tarasiuk W.** (2018),Comparative Analysis of Protective Coatings of Car Paints, *Proceedings of Scientific Automotive Conference: KONMOT-2018,* 1–7.
21. **Bouchetara M., Belhocine A.** (2014), Thermoelastic Analysis of Disk Brakes Rotor, *American Journal of Mechanical Engineering*, Vol. 2, No. 4, 103–113.

22. **Cai P., Wang Y., Wang T., Wang Q.** (2015), Effect of resins on thermal, mechanical and tribological properties of friction materials. *Tribology International*, Vol. 87, 1–10.
23. **Česnavičius R., Kilikevičius S., Krasauskas P., Dundulis R., Olišauska H.** (2016), Research of the friction stir welding process of aluminium alloys, *Mechanika*, Vol. 22, No. 4, 291–296.
24. **Chmiel A.** (2008), *Finite element simulation methods for dry sliding wear* (Ph.D. thesis), Department Of The Air Force, Air University, Air Force Institute of Technology.
25. **Cozza R. C.** (2014), Influence of the normal force, abrasive slurry concentration and abrasive wear modes on the coefficient of friction in ball-cratering wear tests, *Tribology International*, Vol. 70, 52–62.
26. **Cozza R. C., Tanaka D. K., Souza R. M.** (2009), Friction coefficient and abrasive wear modes in ball-cratering tests conducted at constant normal force and contact pressure - Preliminary results, *Wear*, Vol. 267, No. 1–4, 61–70.
27. **Czaban J., Szpica D.** (2013), Drive test system to be used on roller dynamometer, *Mechanika*, Vol. 19, No. 5, 600–605.
28. **Dakhil M. H., Rai A. K., Reedy R., Jabbar A. A.** (2014), Structural Design and Analysis of Disc brake in Automobiles, *International Journal of Mechanical and Production Engineering Research and Development*, Vol. 4, No. 1, 95–112.
29. **Dumbleton J. H.** (1981), *Tribology of Natural and Artificial Joints, Chapter 7: Friction and Wear of Materials on Laboratory Testing Machines*, Elsevier, 183–257.
30. **Dundulis R., Krasauskas P., Kilikevičius S.** (2012), Modelling and simulation of strength and damping of the support pillar welded by longitudinal weld, *Mechanika*, Vol.18, No. 2, 135–140.
31. **Dwivedi D. K., Sharma A., Rajan T. V.** (2002), Interface Temperature under Dry Sliding Conditions, *Materials Transactions*, Vol. 43, No. 9, 2256–2261.
32. **Elakhame Z. U., Olotu O. O., Abiodun Y. O., Akubueze E. U., Akinsanya O. O., Kaffo P. O., Oladele O. E.** (2017), Production of Asbestos Free Brake Pad Using Periwinkle Shell as Filler Material, *International Journal of Scientific & Engineering Research*, Vol. 8, No. 6, 1728–1735.
33. **Eriksson M., Bergman F., Jacobson S.** (2002), On the nature of tribological contact in automotive brakes, *Wear*, Vol. 252, 26–36.
34. **Fildes J. M., Mayers S. J., Kilaparti R., Schlepp E.** (2012), Improved ball crater micro-abrasion test based on a ball on three disc configuration , *Wear*, Vol. 274–275, 414–422.
35. **Gee M. G., Gant A., Hutchings I., Bethke R., Schiffman K., Van Acker K., Poulat S., Gachon Y., Stebut J.** (2003), Progress towards standardisation of ball catering, *Wear*, Vol. 255, No. 1–6, 1–13.
36. **Geromel N.** (2014), *Modelling and control of the braking system of the electric Polaris Ranger all-terrain-vehicle* (Master's thesis), University of Padova.
37. **Gopal P., Dharani L. R., Frank D. B.** (1994), Fade and wear characteristics of a glass fiber reinforced phenolic friction materials, *Wear*, Vol. 174, 119–127.
38. **Grochowicz J., Agudelo C., Li S., Abendroth H.** (2014), Influence of Test Procedure on Friction Behavior and its Repeatability in Dynamometer Brake Performance Testing, *SAE Int. J. Passeng. Cars - Mech. Syst*., Vol. 7, No. 4, 1345–1360.
39. **Grzes P**. (2017), Determination of the maximum temperature at single braking from the FE solution of heat dynamics of friction and wear system of equations, *Numerical Heat Transfer. Part A-Applications*, Vol. 71, No. 7, 737–753.
40. **Hagino H., Oyama M., Sasaki S.** (2016), Laboratory testing of airborne brake wear particle emissions using a dynamometer system under urban city driving cycles, *Atmospheric Environment*, Vol. 131, 269–278.
41. **Hoehn B. R., Oster P., Tobie T., Michaelis K.** (2008), Test Methods For Gear, *Lubricants*, Vol. 42, No. 2, 141–152.
42. **Hussein M. A., Mohammed A. S., Al-Aqeeli N.** (2015), Wear Characteristics of Metallic Biomaterials: A Review, *Materials*, Vol. 8, 2749–2768.
43. **Kaleli H.** (2016), New Universal Tribometer as Pin or Ball-on-Disc and Reciprocating Pin-on-Plate Types, *Tribology in Industry*, Vol. 38, No. 2, 235–240.
44. **Kamiński Z.** (2017), A simplified lumped parameter model for pneumatic tubes, *Mathematical and Computer Modelling of Dynamical Systems*, Vol. 23, No. 5, 523–535.
45. **Kamiński Z., Kulikowski K.** (2017), Measurement and evaluation of the quality of static characteristics of brake valves for agricultural trailers, *Measurement*, Vol. 106, 173–178.
46. **Khot S., Borah U.** (2015), Finite Element Analysis of Pin-on-Disc Tribology Test, *International Journal of Science and Research*, Vol. 4, No. 4, 1475–1480.
47. **Kilikevičius S., Česnavičius R., Krasauskas P., Dundulis R., Jaloveckas J.** (2016), Experimental investigation and numerical simulation of the friction stir spot welding process, *Mechanika*, Vol. 22, No. 1, 59–64.
48. **Kucera M., Prsan J.** (2008), Tribologic Properties of Selected Materials, *Technical Sciences*, Vol. 11, 228–241.
49. **Kulikowski K., Szpica D.** (2014), Determination of directional stiffnesses of vehicels'tires under a static load operation, *Maintenance and Reliability*, Vol. 16, No. 1, 66–72.
50. **Li S., Kahraman A., Anderson N., Wedeven L. D.** (2013), A model to predict scuffing failures of a ball-on-disk contact, *Tribology International*, Vol. 60, 233–245.
51. **Li X., Olofsson U., Bergseth E.** (2016), Pin-on-Disc Study of Tribological Performance of Standard and Sintered Gear Materials Treated with Triboconditioning Process: Pre-treatment by Pressure-induced Tribo-film formation, *Tribology Transactions*, Vol. 60, No. 1, 1–43.
52. **Maluf O., Angeloni M., Milan M.T.** (2007), Development of materials for automotive disc brakes, *Minerva*, Vol. 4, No. 2, 149–158.
53. **Matejka V., Lu Y., Matejkova P., Smetana B., Kukutschova J., Vaculík M.** (2011), Possible stibnite transformation at the friction surface of the semi-metallic friction composites designed for car brake linings, *Applied Surface Science*, Vol. 258, No. 5, 1862–1868.
54. **Matejka V., Metinoz I., Wahlstrom J., Alemani M., Perricone G.** (2017), On the running-in of brake pads and discs for dyno bench tests, *Tribology International*, Vol. 115, 424–431.
55. **Mergler Y. J., Huis't Veld H.** (2003), Micro abrasive wear of semi-crystalline polymers, *Tribology Series*, Vol. 41, 165–173.
56. **Mieczkowski G., Molski K., Seweryn A.** (2007) Finite-element modeling of stresses and displacements near the tips of pointed inclusions, *Materials Science*, Vol. 43, No. 2, 183–194.
57. **Mieczkowski G.** (2017), The constituent equations of piezoelectric cantilevered three-layer actuators with various external loads and geometry, Journal of Theoretical and Applied Mechanics, Vol. 55, No. 1, 69–86.
58. **Mieczkowski G.** (2019), Criterion for crack initiation from notch located at the interface of bi-material structure, *Eksploatacja i Niezawodnosc – Maintenance and Reliability*, Vol. 21, No. 2, 301–310.
59. **Min-Soo K.** (2011), Vibration Analysis of Tread Brake Block in the Brake Dynamometer for the High Speed Train, *International Journal Of Systems Applications, Engineering & Development*, Vol. 5, No. 1, 1–8.
60. **Min-Soo K., Jeong-Guk K., Byeong-Choon G., Nam-Po K.** (2010), Comparative studies of the tread brake dynamometer between dry and wet conditions, Selected Topics In System Science And Simulation In Engineering, in: *Proc. 9th WSEAS international conference on System science and simulation in engineering*.
61. **Nagesh S. N., Siddaraju C., Prakash S. V.** (2014), Characterization of brake pads by variation in composition of friction materials, Procedia Materials Science, Vol. 5, 295–302.
62. **Nair R. P., Griffin D., Randall N. X.** (2009), The use of the pin-on-disk tribology test method to study three unique industrial applications, *Wear*, Vol. 267, 823–827.

63. **Nicholson G.** (1995), *Facts about friction: 100 years of brake linings and clutch facings: 2nd edition*, Croydon PA: P&W Price Enterprises Inc.
64. **Nosko O., Alemani M., Olofsson U.** (2017), Characterisation of airborne particles emitted from car brake materials, in: *Proc. 6th World Tribology Congress*, September 17–22,Beijing, China.
65. **Nuraliza N., Syahrullail S., Faizal M. H.** (2016), Tribological properties of aluminum lubricated with palm olein at different load using pin-on-disk machine, *Jurnal Tribologi*, Vol. 9, 45–59.
66. **Osuch-Słomka E.** (2011), Proposed method for determining the values of tests for the ball-cratering metod, *Tribologia*, Vol. 240, 161–171.
67. **Osuch-Słomka E.** (2012), Abrasive Wear Testing Of Antiwear Coatings By Ball-Cratering-Method, *Tribologia*, Vol. 2, 59–68.
68. **Osuch-Słomka E., Ruta R., Słomka Z.** (2013), The use of a modern method of designing experiments in ball-cratering abrasive wear testing, *Journal of Engineering Tribology*, Vol. 227, 1177–1187.
69. **Patel S. K., Jain A. K.** (2014), Experimental study of brake lining materials with different manufacturing parameters, *International Journal of Engineering Trends and Technology*, Vol. 7, No. 4, 192–197.
70. **Pauschitz A., Jech M., Ebrecht J., Lebersorger T.** (2005), Investigation of Influence of Inclination on Friction and Wear Mechanisms in Piston Ring Cylinder Liner Contact With the New SRV® 4 Test Rig, in: *Proc. World Tribology Congress III*.
71. **Pérez A. T., Fatjó G. G., Hadfield M., Austen S.** (2011), Model of friction for a pin-on-disc configuration with imposed pin rotation, *Mechanism and Machine Theory*, Vol. 46, 1755–1772.
72. **Placha D., Vaculík M., Mikeska M., Dutko O., Peikertova P., Kukutschova J.** (2017), Release of volatile organic compounds by oxidative wear of automotive friction materials, *Wear*, Vol. 376–377, 705–716.
73. **Polajnar M., Kalin M., Thorbjornsson I., Thorgrimsson J. T., Valle N., Botor-Probierz A.** (2017), Friction and wear performance of functionally graded ductile iron for brake pads, *Wear*, Vol. 382–383, 85–94.
74. **Priyana M. S., Hariharan P.** (2014), Abrasive Wear Modes in Ball-Cratering Test Conducted on $Fe_{73}Si_{15}Ni_{10}Cr_2$ Alloy Deposited Specimen, *Tribology in Industry*, Vol. 36, No. 1, 97–106.
75. **Puławski G., Szpica D.** (2015), The modelling of operation of the compression ignition engine powered with diesel fuel with LPG admixture, Mechanika, Vol. 21, No. 6, 501–506.
76. **Ramesh B. T., Arun K. M., Swamy R. P.** (2015), Dry Sliding Wear Test Conducted On Pin-On-Disk Testing Setup For Al6061-Sic Metal Matrix Composites Fabricated By Powder Metallurgy, *International Journal of Innovative Science, Engineering & Technology*, Vol. 2, No. 6, 264–270.
77. **Rashid A., Strömberg N.** (2013), Thermomechanical simulation of wear and hot bands in a disc brake by adopting an eulerian approach, in: *Proc. EuroBrake2013*.
78. **Richard D. L.** (2004), Using infrared technology to detect hot or defective brakes on trucks, Colorado Department of Transportation, in: *Report No. CDOT-DTD-R-2004-15*.
79. **Rowe K. G., Bennett A. I., Krick B. A., Sawyer W. G**. (2013),In situ thermal measurements of sliding contacts, *Tribology International*, Vol. 62, 208–214.
80. **Sarkar C., Hirani H.** (2015), Frictional Characteristics of Brake Pads using Inertia Brake Dynamometer, *International Journal of Current Engineering and Technology*, Vol. 5, No. 2, 981–989.
81. **Schmidt D. L., Davidson K. E., Theibert L. S.** (1999), Unique applications of carbon/carbon composite materials, part 1, *Sampe Journal*, Vol. 35, No. 3, 27–39.
82. **Ścieszka S. F.** (1998), *Friction brakes – material, structural and tribological problems*, ITE, Radom.
83. **Shipway P. H., Hogg J. J.** (2007), Wear of bulk ceramics in microscale abrasion—The role of abrasive shape and hardness and its relevance to testing of ceramic coatings, *Wear*, Vol. 263, No. 7–12, 887–895.
84. **Sikder A. K.** (2014), *Tribo-testing Applications in Automotive and Effective Characterization of the Tribo-tests*, Bruker Nano Surfaces Division, Bangalore.
85. **Söderberg A., Andersson S.** (2009), Simulation of wear and contact pressure distribution at the pad-to-rotor interface in a disc brake using general purpose finite element analysis software, *Wear*, Vol. 267, 2243–2251.
86. **Stachowiak G. W., Batchelor A. W., Stachowiak G. B.** (2004), *Experimental Methods in Tribology*, first ed., Elsevier, Amsterdam.
87. **Sugözü B., Dağhan B.** (2016), Effect of BaSO4 on Tribological Properties of Brake Friction Materials, *International Journal of Innovative Research in Science*, Engineering and Technology, Vol. 5, No. 12, 30–35.
88. **Surojo E., Jamasri, Malau V., Ilman M. N.** (2015), Investigation of friction behaviors of brake shoe materials using metallic filter, *Tribology in industry*, Vol. 37, No. 4, 473–481.
89. **Szpica D.** (2015a), Characteristics of motion reserve of passenger vehicle engines, in: *Proceedings of the 19th International Scientific Conference Transport Means*, October 22–23, 2015, Kaunas University of Technology, Lithuania.
90. **Szpica D.** (2015b), Simplified numerical simulation as the base for throttle flow characteristics designation, *Mechanika*, Vol. 21, No. 2, 129–133.
91. **Szpica D.** (2016), The influence of selected adjustment parameters on the operation of LPG vapor phase pulse injectors, *Journal of Natural Gas Science and Engineering*, Vol. 34, 1127–1136.
92. **Szpica D.** (2018), Research on the influence of LPG/CNG injector outlet nozzle diameter on uneven fuel dosage, *Transport,*Vol. 33, No. 1, 186–196.
93. **Talati F., Jalalifar S.** (2009), Analysis of heat conduction in a disk brake system, *Heat Mass Transfer*, Vol. 45, 1047–1059.
94. **Tamboli K., Sheth S.** (2008), An Overview Of Some Experimental Methods In Tribology, in: *Proc. National Conference on "Emerging Trends in Mechanical Engineering"* (ETME-2008).
95. **Telang A., Rehman A., Dixit G., Das S.** (2010), Effect of reinforcement and heat treatment on the friction performance of Al Si alloy and brake pad pair, *Archives of Applied Science Research*, Vol. 2, No. 4, 95–102.
96. **Trzos M.** (2010), The Analysis Of Tribotester Influence On Friction Coefficient Estimation, *Tribologia*, Vol. 6, 123–135.
97. **Tsang P. H. S., Jacko M. G., Rhee S. K.** (1985), Comparison of Chase and inertial brake Dynamometer testing of automotive friction material, Wear, Vol. 103, No. 3, 217–232.
98. **Uyyuru R. K., Surappa M. K., Brusethaug S.** (2007), Tribological behavior of Al–Si–SiC p composites/automobile brake pad system under dry sliding conditions, *Tribology International*, Vol. 40, No. 2, 365–373.
99. **Varinauskas V., Diliūnas S., Kubilius M., Kubilius R.** (2013), Influence of cantilever length on stress distribution in fixation screws of All - on - 4 full - arch bridge, *Mechanika*, Vol. 19, No. 3, 260–263.
100. **Walliman N.** (2010), *Research Methods: The Basics*, Routledge, London.
101. **Wu B. D., Ma J. J., Liu X. Y., Sun J. Y.** (2009), Comparison Research on Inertia Simulation in Brake Dynamometer Test, in: *Proc. Materials Science Forum*.
102. **Yan W., O'Dowd N. P., Busso E. P.** (2002), Numerical study of sliding wear caused by a loaded pin on a rotating disc, *Journal of the Mechanics and Physics of Solids*, Vol. 50, 449–470.
103. **Yevtushenko A. A.** (2014), *Analytical and numerical modeling of transient process of heat generation in the elements of friction braking systems*: in Polish, Oficyna Wydawnicza Politechniki Białostockiej, Bialystok.

104. **Yevtushenko A. A., Grześ P.** (2015a), 3D FE model of frictional heating and wear with a mutual influence of the sliding velocity and temperature in a disc brake, *International Communications in Heat and Mass Transfer*, Vol. 62, 37–44.
105. **Yevtushenko A. A., Grześ P.** (2015b), Maximum temperature in a three-disc thermally nonlinear braking system, *International Communications in Heat and Mass Transfer*, Vol. 68, 291–298.
106. **Yevtushenko A. A., Grześ P.** (2016), Mutual influence of the sliding velocity and temperature in frictional heating of the thermally nonlinear disc brake, International Journal of Thermal Science, Vol. 102, 254–262.
107. **Yevtushenko A. A., Kuciej M., Grześ P., Wasilewski P.** (2017), Temperature in the railway disc brake at a repetetive short-term mode of braking, *International Communications in Heat and Mass Transfer*, Vol. 84, 102–109.
108. **Zdravecká E., Ondáč M., Tkáčová J.** (2013), The wear tribometer and digitalization of tribological tests data, *Journal of Achivements in Materials and Manufacturing Engineering*, Vol. 61, No. 2, 321–326.
109. **Zmitrowicz A.** (2006), Wear Patterns And Laws Of Wear - A Review, *Journal Of Theoretical and Applied Mechanics*, Vol. 44, No. 2, 219–253.

Acknowledgements: The research has been carried out within work no. MB/WM/4/2017, financed from funds used for the development of young scientists and doctoral students.

DOI 10.2478/ama-2019-0026

ATTRIBUTE SELECTION FOR STROKE PREDICTION

Małgorzata ZDRODOWSKA*

*Faculty of Mechanical Engineering, Department of Biocybernetics and Biomedical Engineering
Bialystok Technical University, ul. Wiejska 45C, 15-351 Bialystok, Poland

m.zdrodowska@pb.edu.pl

received 24 April 2019, revised 28 September 2019, accepted 30 September 2019

Abstract: Stroke is the third most common cause of death and the most common cause of long-term disability among adults around theworld. Therefore, stroke prediction and diagnosis is a very important issue. Data mining techniques come in handy to help determine the correlations between individual patient characterisation data, that is, extract from the medical information system the knowledge necessary to predict and treat various diseases. The study analysed the data of patients with stroke using eight known classification algorithms (J48 (C4.5), CART, PART, naive Bayes classifier, Random Forest, Supporting Vector Machine and neural networks Multilayer Perceptron), which allowed to build an exploration model given with an accuracy of over 88%. The potential features of patients, which may be factors that increase the risk of stroke, were also indicated.

Keywords: data mining, classifier, J48 (C4.5), CART, PART, naive Bayes classifier, Random Forest, Support Vector Machine, Multilayer Perceptron, haemorrhagic stroke, ischaemic stroke

1. INTRODUCTION

According to the American Heart Association and the American Stroke Association, stroke is a sudden, focal, vascular damage to the central nervous system (brain, retina or spinal cord), whose condition is to confirm the presence of a stroke in neuroimaging or persistence and focal symptoms over 24 hours, while excluding other causes of neurological disorders. Within the meaning of this definition, the stroke diagnosis also includes patients with infarction-related focuses revealed in imaging studies whose clinical symptoms have resolved in less than 24 hours (Sacco et al., 2013).

Stroke is a sudden life-threatening condition, which requires hospitalisation. Stroke is caused by a sudden disturbance of the blood supply to the brain. This is the case if a large artery that supplies blood to the brain or a small intracerebral artery will close, severely narrow or crack and will not supply the blood with oxygen and nutrients to a specific area of the brain. The consequence of closing or major narrowing of the arteriole is an ischaemic stroke, otherwise known as cerebral infarction. In contrast, a haemorrhagic stroke (commonly referred to as 'stroke') occurs when the artery breaks and the blood spills over a certain area of the brain. Ischaemic strokes account for 85% of all strokes, whereas haemorrhagic strokes for 15%. Thus, the essence of stroke is acute cerebral insufficiency of various aetiologies, which causes reduced cerebral perfusion in the course of ischaemia or haemorrhage. Even a small ischaemic focal point located, for example, in the inner capsule can manifest itself in complete paralysis of the mid-body and loss of sensation in it (Mazur, 2005). Clinical signs of stroke include paresis or hemiplegia, halitic sensory disorder, aphasia speech disorders – the inability to say words and understand simple commands, visual disturbances – one-eye distraction, visual field disorders, dizziness and headaches with centrifugal feeling, accompanied by nausea, vomiting, balance disorders or double vision. The most important risk factors for stroke are hypertension, heart disease, diabetes, dyslipidaemia and coagulation disorders (Jacobs and Sapers, 2011; Strepikowska and Buciński, 2009; Trochimczyk et al., 2017).

Stroke is a very important medical and social problem. It is the main cause of permanent disability and lack of independence in the group of adults. It is estimated that 15 million people fall for a stroke every year in the world, and about 5 million people die (Sacco et al., 2013). This disease is in third place among causes of death (after cardiovascular disease and cancer) (Mackay and Mensah, 2004). Long-term disability results in serious social and economic consequences of patients and their families. Economic aspects are related not only to the costs of hospital treatment but, above all, also to long-term care, long-term rehabilitation and long-term treatment of patients after stroke. Among patients who survived the stroke, as much as 60% remain less or less disabled. In this group, half of the patients are not dependent or require constant care (Mackay and Mensah, 2004). Since stroke is a serious threat to life, proper and fast help is very important. The earlier a patient with this disease goes to a hospital, the greater the chance of survival and the avoidance of severe disability (Strepikowska and Buciński, 2009; Trochimczyk et al., 2017).

Due to the development of data mining techniques, prediction and diagnosis of stroke are possible with increasing accuracy. Medical information systems have enormous data resources on patients, their health status and treatment processes. However, this information becomes meaningful only when their correlations with other information can be determined. This is what data mining algorithms deal with, which allow finding new, significant and correlated information in the data set. They are used especially to classify diseases, patients as well as for predictive pur-

poses (Maimon and Rokach, 2010; Yoo et al., 2012; Dardzińska, 2013; Alaiz-Moreton et al., 2018; Derlatka et al. 2019).

The aim of this study is to evaluate the effectiveness of selected data mining techniques for predicting the occurrence of stroke, as well as to identify those features of the patient that have the greatest impact on the occurrence of stroke. It will also be analysed how the reduction of attributes describing patients affects the accuracy of the classification.

2. METHODOLOGY

The study analysed the data of patients affected by stroke. The test sample included 215 patients diagnosed with haemorrhagic stroke and ischaemic stroke. The characteristics of the test sample are presented in Table 1.

Tab. 1. Characteristic of patients

	Amount	Average age (min–max)	Haemorrhagic stroke	Ischaemic stroke
Women	118	76, 47 (42–97)	15	103
Men	97	72, 15 (39–91)	16	81
All	**215**	**74, 53 (39–97)**	**31**	**184**

Each of the patients is characterised by 34 attributes (including age, sex, presence or absence of atrial fibrillation, blood pressure, level of consciousness, laboratory test results, types of drugs administered, etc). Part of the patients' data was incomplete.

Before data processing, the data were cleaned (incorrect values, incorrect entries, etc) and prepared for processing in the WEKA software. Columns and rows with large gaps were removed; data from non-significant assumptions were removed; gaps in numerical data were filled and data were discretised and normalised. In addition, the data were divided into two separate data sets: a set of training data (learning) to build the model (80%) and a set of test data for model evaluation (20%).

WEKA is software in the field of machine learning and knowledge acquisition created in the JAVA programming language environment, was used to analyse the data. The WEKA program, created at the University of Waikato in New Zealand, is a set of algorithms used to carry out data mining tasks, which allows, among others, for initial data processing, grouping, classification, regression, visualisation or the discovery of association rules (Witten et al., 2011).

In this work, classification was made for four models:

- Model 1: all available variables (34 attributes).
- Model 2: variables indicated in the literature as risk factors (11 attributes: hypertension, ischaemic heart disease, previous myocardial infarction, carotid artery stenosis, atrial fibrillation, diabetes, dyslipidaemia, smoking, alcohol, age and gender).
- Model 3: variables extracted using attributes selection – chi-square test (nine attributes: antiplatelet drugs, high-density lipoprotein (HDL), calcium (Ca)-blocker, low-density lipoprotein (LDL), diuretic, diabetes, ischaemic heart disease, total cholesterol and statin).
- Model 4: new variables – analysis of the principal component analysis (PCA) (five new attributes).

Due to the high accuracy, eight algorithms were used for the classification (Han and Kamber, 2006; Witten et al., 2011; Aggarwal, 2015; Frank et al., 2016, Chen et al., 2017; Kiranmai and Laxmi, 2018; Zdrodowska et al., 2018):

- J48 (C4.5) is an implementation of the C4.5 decision tree algorithm, which builds trees from a training set using entropy (information theory). It involves recursively visiting each decision-making node and selecting a possible division. To select the optimal division of the training set in the algorithm, the information gain is calculated. The C4.5 algorithm recursively visits each decision node, selecting a possible division, until further subdivisions are possible, uses trees that do not have to be binary, creates separate branches for each value of the qualitative attribute.
- CART is a very popular data classification method used to build decision trees. Its main features are high efficiency, the ability to build a tree both based on discrete and continuous data, creation of binary nodes (from each node leave at most two branches) and division of classes of solutions into superclasses (groups of classes). Like most algorithms, CART may interrupt its operation based on the interruption criterion. This criterion is determined based on the number of incorrect classifications and the number of tree leaves. It is this action that classifies the algorithm as a regression algorithm, as it evaluates and predicts the result besides the classification. There are several modifications of the CART algorithm; they differ mainly in the way of breaking the tree structure and assigning labels to the nodes.
- PART: the key of the PART algorithm is the construction of a partial decision tree, on the basis of which knowledge in the form of rules is discovered. The partial tree is an ordinary decision tree that undergoes construction and trimming operations until a stable subtree is found which cannot be simplified at a later stage. As soon as a partial tree is found, the rule is constructed and the tree discarded. This avoids rule generalisation and overdevelopment of the subtree, as happens when building rules with naive methods. Using the method of separation and winning in decision trees, the sensitivity and speed of the algorithm extracting the rule are increased. The algorithm does not require data optimisation.
- Naive Bayes Classifier is one of the machine learning methods used to solve sorting and classification problems. The task of the Bayes classifier is to assign a new case to one of the decision classes, while the set of decision classes must be finite and defined apriori. The naive Bayes classifier is a statistical classifier based on Bayes' theorem. In terms of efficiency, the naive Bayes classifier is comparable to classification algorithms by induction of decision trees and neural network classification methods. It is characterised by high accuracy and scalability even for very large data volumes. The naive Bayes classifier assumes that attribute values in classes are independent.
- Random Forest is a method of classification (and regression) involving the creation of multiple decision trees based on a random set of data. The idea of this algorithm is to build a team of experts from random decision trees, where, unlike classic decision trees, random trees are built on the principle that a subset of the analysed features in the node is randomly selected. In addition, individual trees from random forest trees are built according to the concept of bugging. Random forests are considered one of the best classification methods. Single

DOI 10.2478/ama-2019-0026

random forest classifiers are decision trees. The Random Forest algorithm is very well suited for trial testing, where the observation vector is a large dimension. Their additional advantage is the ability to use the learned random forest for other issues than just for classification. For example, based on trees from the forest, one can determine the ranking of variables, and thus determine which variables have better predictive properties.

- Support Vector Machine (SVM) offers very high accuracy compared with other classifiers, and its advantage is the use of non-linear data. The SVM can easily handle many continuous and categorical variables. SVM constructs a hyperplane in multidimensional space to separate different classes and generates the optimal hyperplane in a repetitive manner that is used to minimise the error. The basic idea of the SVM is to find the maximum boundary hyperplane (MMH) that best divides the data set into classes. SVM can be used for both classification and regression challenges. However, it is most often used in classification problems. The main purpose of the algorithm is to segregate a given data set in the best possible way. The distance between the nearest points is called the margin. The goal is to select a hyperplane that has the maximum possible margin between carrier vectors in a given data set.
- Multilayer perceptron (MLP) is a unidirectional multilayer neural networks; in other words, MLP networks are the most frequently described and most frequently used in practical applications of neural architecture. Their dissemination is related to the development of the algorithm of back error propagation, which enabled effective training of this type of network in a relatively simple manner. The multilayer neural network can approximate any complex and complex mapping. At the same time, the user does not have to know or assume any form of dependency in the sought after model and does not even need to ask himself whether any mathematical modelling of dependencies exists at all. This feature, combined with an independent method of learning a neural network, makes it an extremely useful and convenient tool for all kinds of applications related to forecasting, classification or automatic control.

The ACC (total accuracy) measure was used to assess the above classifiers. In order to test the accuracy of the constructed models, a matrix of errors (Kasperczuk et al., 2019) was used. ACC is the total efficiency of the classifier, which determines the probability of correct classification, that is, the ratio of correct classifications to all classifications. It is expressed by the equation (Bramer, 2016):

$$ACC = (TP + TN) / (TP + TN + FP + FN) \quad (1)$$

where (Bramer, 2016):

- TP (true positive) is the number of observations correctly classified to the positive class.
- TN (true negative) is the number of observations correctly classified to the negative class.
- FP (false positive) is the number of observations classified to a positive class when in fact they come from a negative class.
- FN (false negative) is the number of observations classified to the negative class when in fact they come from a positive class.

3. RESULTS AND DISCUSSION

The results of the classification of training and test sets for each of the proposed models are shown in Figs. 1–5.

For model 1 (Fig. 1), which use all attributes, in the case of a training set, the highest accuracy was achieved for the Random Forest classifier (99.42%). Equally, high accuracy (95.51%) was obtained for the MLP neural network algorithm. The SVM algorithm turned out to be the weakest; however, the accuracy is still quite high (over 86%).

For the test set, it is observable that all the algorithms work correctly, giving more than 80% accuracy. The highest accuracy was obtained using the Naive Bayes algorithm (88.38%), while the weakest results (however, still high – over 81%) were obtained using the J48 algorithm. It is easy to see in Fig. 1 that the differences in accuracy for the training and test set are small, which indicates a good model.

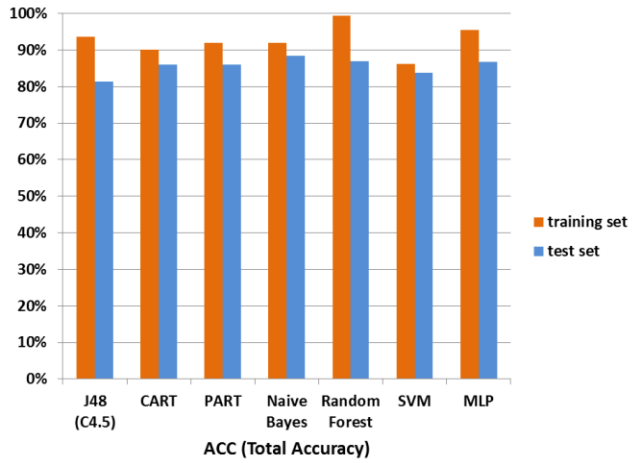

Fig. 1. Comparison of accuracy (ACC) of classifiers for model 1 (all variables) for training and test sets

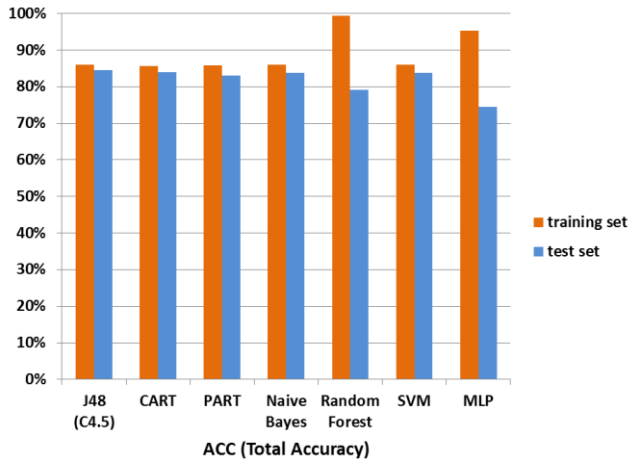

Fig. 2. Comparison of accuracy (ACC) of classifiers for model 2 (variables indicated in the literature as risk factors) for training and test sets

Let us look at model 2 (Fig. 2), which contains only variables indicated in the literature as risk factors (11 attributes: hypertension, ischaemic heart disease, past myocardial infarction, carotid stenosis, atrial fibrillation, diabetes, dyslipidaemia, smoking, alcohol, age and sex).

As we can see in Fig. 2, for model 2, the most accurate classifiers for the training set are Random Forest and MLP (99.42% and 95.35% accuracy, respectively). The total accuracy of the other classifiers is within 85–86%, which is quite a good result. For the test set, the J48 algorithm is the most accurate classifier (84.52%). Other classifiers also work correctly giving good matches. In principle, all algorithms (except Random Forest and MLP) give the test set a slightly lower accuracy index than in the case of the training set (about 2–3%), which indicates a very good model.

Let us move on to the model 3, which contains attributes extracted using feature selection – chi-square test (nine attributes: antiplatelet drugs, HDL, Ca-blocker, LDL, diuretic, diabetes, ischaemic heart disease, total cholesterol and statin). The classification results for this model are shown in Fig. 3.

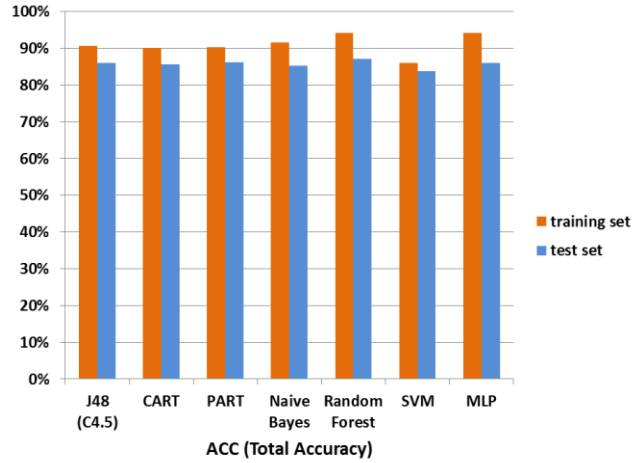

Fig. 3. Comparison of accuracy (ACC) of classifiers for model 3 (variables extracted after attributes selection) for training and test sets

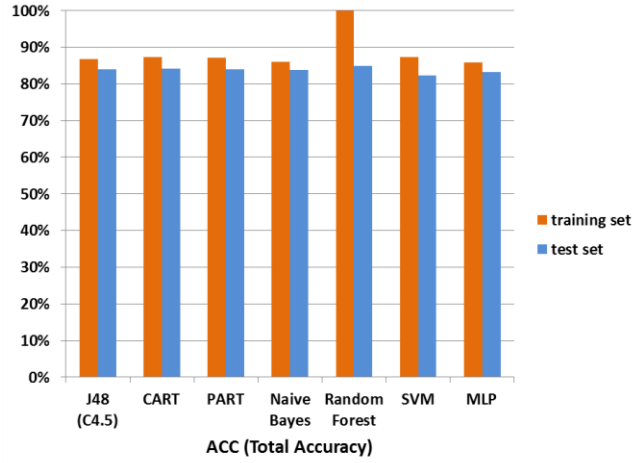

Fig. 4. Comparison of accuracy (ACC) of classifiers for model 4 (new variables – principal component analysis method) for training and test sets

In the case of model 3, the Random Forest and MLP algorithms proved to be the most accurate for the training set, which gave over 94% accuracy. Other algorithms also achieved accuracy above 90%. SVM turned out to be the weakest (86.05% accuracy). For the test set, the Random Forest algorithm was also the most accurate (87.05%), but for the other algorithms, high accuracy of over 83% was also achieved. It is worth adding here that in the case of the model with feature selection, the classification using the SVM achieved only a slightly lower accuracy for the test set than for the training set, which indicates a very good fit of the model (86.05% and 83.73%).

The last model is a model which contains five new variables obtained by PCA. The classification results for this model are shown in Fig. 5.

For model 4, the training set and the test set, the highest accuracy was obtained using the Random Forest algorithm. This accuracy is very high for both sets and reaches 84.85% for the test set, which shows us the benefits of PCA. The SVM algorithm proved to be the least accurate algorithm for model 4.

Fig. 4 shows that for all algorithms, the classification accuracy for the test set is slightly lower than for the training set, which indicates a good model.

Taking into consideration the comparison of the correctly classified objects in individual models (Fig. 5). The results obtained on the test set were compared because it shows the correct accuracy and usefulness of the model.

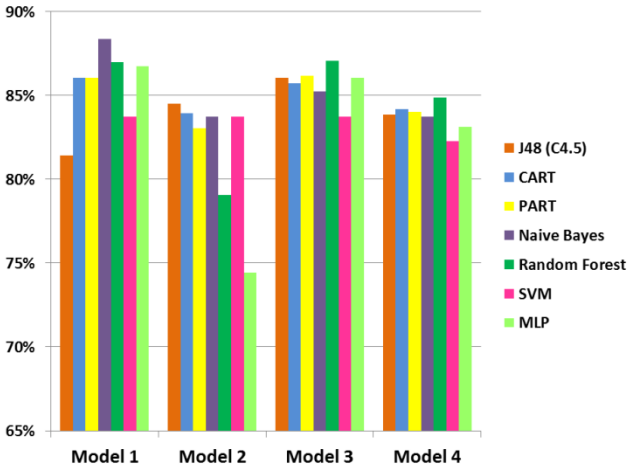

Fig. 5. Comparison of correctly classified objects in individual models (for test set)

The most accurate classification (88.38%) was obtained using the Naive Bayes algorithm for model 1, that is, working on all available attributes. A slightly lower accuracy (87.95%) was obtained for the Random Forest algorithm and model 3, which contains only attributes extracted using the feature selection – the chi-square.

The small difference between accuracy for the model containing all features and for models after feature selection. In several cases, classifiers for models after feature selection give better accuracy (or very similar) than models in which all attributes are included. It shows the usefulness of using attribute selection, which not only saves time but also gives better predictive results.

4. CONCLUSION

Knowledge discovery in databases is a dynamically developing field, whose rapid development is related to the growing number of databases and the size of information collected in them. Increasingly, data mining finds its application in medicine and medical information systems. The analysis of classification algo-

DOI 10.2478/ama-2019-0026

rithms carried out shows that they can be a very important tool supporting the prediction and diagnosis of various diseases. Detailed data analysis, their proper preparation and proper classification allow to achieve very accurate results. The study analyses the data of patients with stroke using eight popular classification algorithms, which allowed to build a mining model with an accuracy of over 87%.

By analysing the data of stroke patients, the difference between raw data and data after feature selection and analysis of basic components (PCA) was examined. The results obtained in this study confirmed the benefits of feature selection and analysis of basic components. The accuracy ratios of each of the algorithms used for the data after attribute reduction were similar to those with raw data.

Tests done with the help of WEKA software show that the attributes are most important in diagnosing a stroke. Important features were diabetes, ischaemic heart disease, dyslipidaemia, HDL, LDL and total cholesterol levels. It has also been shown that patients who have been given anticoagulants (antiplatelet drugs), blood lipid-lowering drugs (statins) and antihypertensive drugs (diuretic, Ca-blocker) have a higher risk of stroke. This may mean that patients who have been diagnosed with the above-mentioned diseases are more likely to have a stroke. This conclusion is confirmed in the literature, where hypertension, circulatory diseases and diabetes are mentioned as one of the main causes of stroke (Strepikowska and Buciński, 2009).

REFERENCES

1. **Aggarwal C.C.** (2015), *Data Classification Algorithms and Applications*, Chapman & Hall/CRC, New York.
2. **Alaiz-Moreton H., Fernández-Robles L., Alfonso-Cendón J., Castejón-Limas M., Sánchez-González L., Pérez H.** (2018),Data mining techniques for the estimation of variables in health-related noisy data, *Advances in intelligent systems and computing*, 649, 482–491.
3. **Bramer M.** (2016),*Principles of Data Mining*, Springer.
4. **Chen Y.C., Suzuki T., Suzuki M., Takao H., Murayama Y., Ohwada H.** (2017), Building a Classifier of Onset Stroke Prediction Using Random Tree Algorithm, International Journal of Machine Learning and Computing, 7(4), 61-66.
5. **Dardzińska A.** (2013), *Action Rules Mining*, Springer, Berlin.
6. **Derlatka M., Ihnatouski M., Jałbrzykowski M., Lashkovski V., Minarowski Ł.** (2019),Ensembling rules in automatic analysis of pressure on plantar surface in children with pes planovalgus,*Advances in Medical Sciences*, 64(1), 181-188.
7. **Frank E., Hall M.A., Witten I.A.** (2016), *The WEKA Workbench. Online Appendix for "Data Mining: Practical Machine Learning Tools and Techniques*", Morgan Kaufmann.
8. **Han J., Kamber M.** (2006), *Data mining. Concepts and Techniques*, 2nd ed, Elsevier, San Francisco.
9. **Jacobs L.K., Sapers B.L.** (2011), Neurological Disease, In: Cohn S. (editor), *Perioperative Medicine*, Springer, London.
10. **Kasperczuk A., Daniluk J., Dardzińska A.** *(2019),* Smart Model to Distinguish Crohn's Disease from Ulcerative Colitis, *Applied Sciences*, 9(8), 1650.
11. **Kiranmai S.A., Laxmi J.A.** (2018), Data mining for classification of power quality problems using WEKA and the effect of attributes on classification accuracy, *Protection and Control of Modern Power Systems*, 3(29),https://doi.org/10.1186/s41601-018-0103-3.
12. **Mackay J., Mensah G.** (2004), *The Atlas of Heart Disease and Stroke: Global burden of stroke*, World Health Organization.
13. **Maimon O., Rokach L.** (ed). (2010), *Data mining and knowledge discovery handbook*, Springer.
14. **Mazur R., Świerkocka-Miastkowska M.** (2005), Stroke - first symptoms (in Polish), Choroby Serca i Naczyń, 2 (2), 84-87.
15. **Sacco R.L., Kasner S.E., Broderick J.P., Caplan L.R., Connors J.J., Culebras A., Elkind M.S., George M.G., Hamdan A.D., Higashida R.T., Hoh B.L., Janis L.S., Kase C.S., Kleindorfer D.O., Lee J.M., Moseley M.E., Peterson E.D., Turan T.N., Valderrama A.L., Vinters H.V.** (2013), An updated definition of stroke for the 21st century: a statement for healthcare professionals from the American Heart Association/American Stroke Association, Stroke, 44, 2064-2089.
16. **Strepikowska A., Buciński A.** (2009), Stroke – risk factors and prophylaxis (in Polish), *Farmakopea Polska*, 65(1), 46–50.
17. **Trochimczyk A.**, **Chorąży M., Snarska K.K.** (2017), An analysis of patient quality of life after ischemic stroke of the brain, *The journal of neurological and neurosurgical nursing*, 6(2), 44–54.
18. **Witten I.H., Frank E., Hall M.A.** (2011), *Data Mining: Practical Machine Learning Tools and Techniques*, Morgan Kaufmann.
19. **Yoo I., Alafaireet P., Marinov M.** (2012), Data mining in healtcare and biomedicine, A survey of the literature, *Journal of the medical systems*, 35(4), 2431–2448.
20. **Zdrodowska M., Dardzińska M., Chorąży M., Kułakowska A.** (2018), Data Mining Techniques as a Tool in Neurological Disorders Diagnosis, *Acta Mechanica et Automatica*, 12(3), 217-220.

Acknowledgements: This work is supported by the Polish Ministry of Science and Higher Education of Poland under research project No. MB/WM/17/2018.

sciendo

DOI 10.2478/ama-2019-0027

acta mechanica et automatica, vol.13 no.3 (2019)

NEAR-SURFACE MASS DEFECT IN MODELS OF LOCALLY HETEROGENEOUS SOLID MECHANICS

Taras NAHIRNYJ*, Kostiantyn TCHERVINKA, *****

*Faculty of Mechanical Engineering, Institute of Computer Science and Production Management, University of Zielona Góra, ul. prof. Z. Szafrana 4, 65-516 Zielona Góra, Poland
**Mathematical Modeling Department, Mechanical and Mathematical Faculty, Ivan Franko University of Lviv, 1 Universytetska str., Ukraine 79000 Lviv, Ukraine
***Centre of Mathematical Modeling of Ukrainian National Academy of Sciences, 15 Dudaeva Str., Ukraine 70005, Lviv, Ukraine

t.nahirny@iizp.uz.zgora.pl, k.tchervinka@gmail.com

received 1 July 2019, revised 10 October 2019, accepted 24 October 2019

Abstract: This article deals with the model of the locally heterogeneous elastic body. The model accounts for long-range interaction and describes near-surface non-homogeneity and related size effects. The key systems of model equations are presented. From the viewpoint of the representative volume element, the boundary condition for density and the limits of applicability of the model are discussed. The difference of mass density in the near-surface body region from the reference value (near-surface mass defect) causes a non-zero stressed state. It is indicated on the strong dependence of the surface value of density from the curvature of the surface of thin fibres. The effect of the near-surface mass defect on the stressed state and the size effect of surface stresses have been investigated on an example of a hollow cylinder. Size effect of its strength has been studied as well.

Keywords: locally heterogeneous mechanics, RVE, mass defect, size effects, thin fibres

1. INTRODUCTION

In recent decades, various nanoelements are widely used in engineering practice, namely, thin films, fibres and small particles. They are often used to obtain materials and solid bodies with complex microstructure. Such bodies feature comparable surface and volume factors in internal energy.

The basis for studying the behaviour of nanoelements is non-local mathematical models of mechanics, since classical elasticity (e.g., Sneddon and Berry, 1958) that rests upon locality principle fails to describe and predict many observable properties of bodies made of microstructured materials among them surface phenomena and size effect of structural strength. A variety of non-local mathematical models of mechanics is represented in the scientific literature (Eringen, 2002; Karlicic et al., 2015; Khodabakhshi and Reddy, 2015; Matouš et al., 2017). Such models usually take into account long-range interaction, that is, the state at the considered point of the body depends on the state of all points of the body. In peridynamics theory (Silling, 2000), it is done for homogeneous materials by specifying particles force interaction at a finite distance by pairwise force function and considering a peridynamic material without memory, a microelastic material and a structureless material for different simplifying conditions. The models become far more complicated if heterogeneous materials are to be considered.

The models that employ a one-continuum approach to describe the structure of material generally include non-local and gradient models of mechanics. These models are based on a generalisation of the Hooke's law for continuous media. In gradient models, it is done by including spatial derivatives typically of the second order into the relation that links the stress and strain tensors (Aifantis, 2011; Di Paola et al., 2010; Polizzotto, 2003, 2012), or by presenting the dependence between these tensors in the form of spatial functional dependence where the kernel depends on the distance from the point in question to a travelling point (Bažant and Jirásek, 2002; Eringen, 2002; Marotti de Sciarra, 2009). In the last case, it is done by integrating over the region of the body or some neighbourhood of the considered point.

Another approach to describe structural and near-surface non-homogeneities is the local gradient approach in thermomechanics (Burak et al., 2014; Nahirnyj and Tchervinka, 2015, 2018). It is based on the general principles of irreversible thermodynamics and mechanics of rheological systems. Within this approach, a deformable solid is considered as an open thermodynamic system whose mass changes relative to the reference solid. The density and the chemical potential as a conjugated parameter are introduced into the state parameter space. It is efficiently used to describe the structure of material and internal forces in the body. Within models of the approach, the near-surface non-homogeneity of different physical fields and related size effects are caused by the mass defect, that is, the difference of density in the current and reference states. This is consistent with the statement (Silling, 2000) that in a structureless material with no change in the local density of particles, the internal forces are absent.

The parameters in the non-local model are usually associated with the microstructure of the material of the body. The composite materials that are multicomponent systems at microlevel and nanolevel are good examples of microstructured and nanostructured materials; they are widely used in technology due to their advantageous mechanical properties (Wisniewska et al., 2019). These materials are heterogeneous though may consist of essentially homogeneous components. Besides multicomponent materials, there is a variety of structured one-component materials.

DOI 10.2478/ama-2019-0027

Proper structuring of many ordinary materials may significantly change mechanical, thermal and other physical properties. Bargmann et al. (2018) considering microstructured materials classifies them into non-porous and porous; here one can find an extensive review on investigation methods for the study of heterogeneous materials with respect to geometrical and topological properties of the microstructures. The mechanics and physics of multiphase porous materials at nano and micro scales are considered by Dormieux et al. (2006), Wang and Liew (2007) and others. Cheng (2016) focuses largely on the linear theories, as in the classical linear elasticity and porous medium flow. Note that the mechanical interaction between the solid and the fluid can be very complex while considering one-component material with a variable porosity just one extra parameter may sufficient to analyse the structural influence on averaged material properties.

The study of the material structural influence on solid body properties is the subject of micromechanics. Micromechanics relies on the concept of a representative volume element (RVE) (Bargmann et al., 2018). The RVE-using approaches and techniques in mechanics of heterogeneous media are widely represented in the literature (Drugan and Willis, 1996; Dormieux and Kondo, 2013; Kwok et al., 2015; Guo and Zhao, 2016; Saeb et al., 2016; Bostanabad et al., 2018; Rezakhani et al., 2017; Wisniewska et al., 2019). The RVE is usually regarded as a volume of heterogeneous material that is sufficiently large to be statistically representative of the material (Kanit et al., 2003) or at least large enough to get a sufficiently accurate model to represent mean constitutive response (Drugan and Willis, 1996). The size of the RVE generally depends on the material system as well as the effective property under consideration (Bostanabad et al.,2018; Drugan and Willis, 1996; Kanit et al., 2003; Rezakhani et al., 2017, etc).

The size and shape of RVE can be easily justified for a known periodic structure; however, the majority of microstructures in engineering materials are non-periodic (Bargmann et al., 2018). For random composites, some approaches are presented by Monetto and Drugan (2009), Salmi et al. (2012), Wisniewska et al. (2019) and others. On the other hand, theoretical approaches able to describe structure-related effects in heterogeneous solid bodies (abovementioned non-local and gradient models) do not investigate the RVE-related problem and peculiarities. In these models, the internal scale that is associated with the heterogeneity characteristic size may be used to estimate RVE size.

In this article, we consider the formulation of boundary value problems for bodies with flat and cylindrical boundaries for the local gradient approach. Using RVE formalism, we justify boundary conditions for mass density and discuss the limitation of the model related to parameters of RVE. We also study the influence of surface curvature on near-surface mass defect and size effects for locally heterogeneous bodies.

2. NEAR-SURFACE MASS DEFECT

Thermomechanics of locally heterogeneous solids (local gradient approach in thermomechanics) introduces the energy of structurally heterogeneous material that differs from the energy of classical thermomechanics by term containing a gradient of chemical potential (Burak et al., 2014; Nahirnyj and Tchervinka, 2018). As a consequence, the free energy F for such material depends on the strain tensor e and mass density ϱ. The conjugate parameters are the stress tensor σ and the thermodynamic chemical potential H, respectively. Perturbation of the latter is associated with the binding energy perturbation. The chemical potential is the energy required to change the density per one unit, while other state parameters are constant. It is clear that such energy is different for interior body points and points of the body surface because interior points interact with other body points in their vicinity, while points of the surface interact with the body points not in all directions. Therefore, these parameters (density and chemical potential) allow to describe different interaction conditions in interior and near-surface body regions and thus enable modelling near-surface and structural non-homogeneity. The state parameters space expansion yields mass balance equation modification. The non-homogeneity of the density is the cause of internal forces as well as non-homogeneity of interconnected fields and experimentally observed size effects.

The system of equations for the locally heterogeneous elastic body model, written down for a linearised approach, has the form (Nahirnyj and Tchervinka, 2015):

$$\mu\nabla^2\mathrm{u} + (\lambda+\mu)\nabla(\nabla\cdot\mathrm{u}) - a_m(3\lambda+2\mu)\nabla\varrho = 0,$$
$$\nabla^2\varrho - \xi_m^2(\varrho-\varrho_*) = 0 \qquad (1)$$

if the displacement vector u and mass density ϱ are the key functions and the form

$$\nabla\cdot\sigma = 0,$$
$$\nabla\times\left\{\nabla\times\left[\sigma - \left(\frac{\lambda}{3\lambda+2\mu}\sigma - 2\mu a_m(\varrho-\varrho_*)\right)\mathrm{I}\right]\right\}^T = 0,$$
$$\nabla^2\varrho - \xi_m^2(\varrho-\varrho_*) = 0 \qquad (2)$$

if the stress tensor σ is chosen as a key function instead of displacement u. Here $\sigma = \sigma\colon \mathrm{I}$, I is identity tensor, λ, μ, a_m, ξ_m are constants, ϱ_* is mass density in the reference state, ∇ is del operator, $\cdot, \times, T$ denote inner, vector products and transpose, respectively. The parameter ξ_m^{-1} is a characteristic size of the structural heterogeneity of the material (Nahirnyj and Tchervinka, 2018).

When formulating the boundary value problems, the corresponding boundary conditions need to be supplemented. Generally accepted conditions in the theory of elasticity are the conditions for the stress tensor σ and the displacement vector u in the form:

$$\sigma\cdot n|_{\partial V_\sigma} = \sigma_a, \;\; u|_{\partial V_u} = u_a.$$

Here n is the unit external normal to the body surface ∂V, $(\partial V_\sigma)\cup(\partial V_u) = (\partial V)$.

The analysis of the equation for mass density (second equation of Eq. (1)) shows that its non-trivial solution exists if the value of the body surface mass density ϱ_a differs from the one of the reference body ϱ_*. The question arises what are the reasons and limitations for the surface value of mass density ϱ_a.

For spatially non-local mechanics models, one usually considers the following four states:

- the ideal continuum,
- the heterogeneous continuum,
- the reference body, and
- the actual body within the model.

It should be noted that the equations of non-local theory, in this case the system of Eqs. (1) and (2), are written for a heterogeneous continuum. These equations provide the existence of the RVE in whose region the averaging is carried out. The quanti-

ties and properties describing the behaviour of the body are defined for this element.

For the reference body, we usually take the body of the same configuration as the investigated one without the local heterogeneity and associated effects.

Let us describe in more detail the mass density of the body of structurally heterogeneous material from the viewpoint of RVE. We denote the region of the body by V and the region RVE by Ω. If describing a point deep in the body, then $\Omega \subset V$and the averaged value of the mass density of a structurally heterogeneous body coincides with ones for a structurally heterogeneous media. It is attributed to the RVE centre and is treated as a characteristic of the homogeneous reference body. In the case $\Omega \backslash V \neq \emptyset$, the domain Ω contains the part of the environment and for the mass density holds

$$\varrho = \varrho_* \left(\int_{\Omega \cap V} dV\right)/\left(\int_{\Omega} dV\right), \tag{4}$$

therefore, $\varrho < \varrho_*$.

Let Ω is a sphere of radius R_0 and V is a halfspace (Fig. 1). Moving the RVE from the halfspace depth to its surface, we arrive at mass density value $\varrho_*/2$ when the centre of RVE is at the surface of halfspace. This means that for the flat body boundary, there is a natural boundary condition

$$\varrho|_{\partial V} \equiv \varrho_a = \frac{1}{2}\varrho_*. \tag{5}$$

It may be noted that the real body surface is rough. Thus, the value of the density at the body surface which is described by Eq. (5) must be treated as the upper bound of the surface density of a real body. Postulating constant density in non-local models restricts the characteristic size of the considered body. In this case, the body characteristic size should be much greater than the long-range interaction distance.

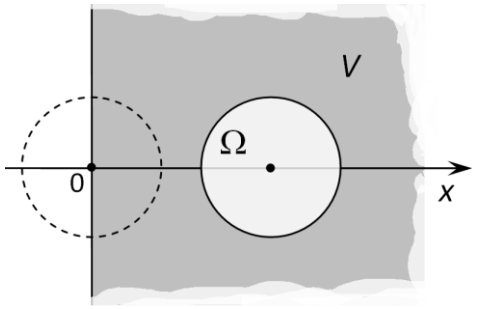

Fig. 1. Spherical representative volume element in the region of halfspaceand at its surface

The mass density in halfspace (region $x \geq 0$) as solution of the problems (1) and (5) has the form:

$$\varrho = \varrho_* - (\varrho_a - \varrho_*)\exp(-\xi_m x). \tag{6}$$

Since ϱ_* is the reference body mass density, the difference $\varrho_* - \varrho$ is the near-surface mass defect in the body actual state.

Based on the analysis of the solution (6), it can be argued that the characteristic size of a representative element (the radius of the sphere R_0) can not be less than $3\xi_m^{-1}$. This restricts the model Eqs. (1) and (2) applicability to flat body boundaries of characteristic size $3\xi_m^{-1}$. The above considerations are also important for models that take into account long-range cohesive forces in the relations for strain and strain tensors and that considers the density to be constant throughout the body.

Sometimes, it is necessary to compare the results for bodies of different geometric configurations, in particular for thin films and fibres as well as for bodies of the same configuration having different characteristic sizes (for instance, fibres of different radii). The question is which mass density value at the cylindrical surface that is equivalent to ones in the boundary condition (5) at the flat surface? Repeating the above arguments for the value ϱ_a^c of mass density at the surface of the cylinder of the radius R_e , we can write:

$$\varrho_a^c = \varrho_* \left\{\frac{1}{2} - \frac{1}{\pi}\int_{\arccos\frac{R_0}{2R_e}}^{\frac{\pi}{2}} \left[1 - 4\left(\frac{R_e}{R_0}\right)^2 \cos^2\varphi\right]^{3/2} d\varphi\right\}. \tag{7}$$

This dependence can be approximated with relative error less than $9.4 \cdot 10^{-4}$ for R_0/R_e in region [0, 0.9] by:

$$\varrho_a^e = \left(0.5 - 0.095\frac{R_0}{R_e}\right)\varrho_*. \tag{8}$$

For mass density at the hollow cylinder inner surface $r = R_i$, we obtain:

$$\varrho_a^i = \left(0.5 + 0.095\frac{R_0}{R_i}\right)\varrho_*. \tag{9}$$

These values tend to the mass density ϱ_a at the surface of the halfspace with radii increase ($R_i \to \infty, R_e \to \infty$) and the surface value of mass density dependence on the radius is more pronounced in thin fibres.

Noteworthy that considered above spherical shape of RVE is one of the most widespread along with cubic shape. If we consider RVE as a cube with edge $2R_1$ and two faces being parallel to the axis of the cylinder, when (7) takes the form:

$$\varrho_a^c = \varrho_* \left\{\frac{1}{2} - \frac{R_e}{2R_1}\left[1 - \frac{\sin^{-1}(R_1/R_e)}{2R_1/R_e} - \frac{1}{2}\sqrt{1 - \left(\frac{R_1}{R_e}\right)^2}\right]\right\}$$

and analogue of (8) is:

$$\varrho_a^e = \left(\frac{1}{2} - \frac{1}{12}\frac{R_1}{R_e} - \frac{1}{80}\left(\frac{R_1}{R_e}\right)^3 + \cdots\right)\varrho_* \approx \left(0.5 - 0.083\frac{R_1}{R_e}\right)\varrho_*.$$

In the case of flat body boundary, the cubic RVE, as well as the spherical RVE, obviously yields $\varrho_a = \varrho_*/2$.

3. STRESSED STATE OF HOLLOW CYLINDER

The body surface curvature effects on the density surface value and the near-surface mass defect, as well as the stress state caused by them, have been studied on the example of the hollow cylinder (region $R_i \leq r \leq R_e$ in the cylindrical coordinates $\{r, \varphi, z\}$). We assume that the cylinder is free of load and at its surfaces $r = R_e$, $r = R_i$, the constant density values are stated according to the formulas (8) and (9).

The distribution of density in the cylinder is described by the formula:

$$\varrho(r) = \varrho_* + \varrho_a^i \frac{K_0(\xi_m R_i)I_0(\xi_m r) - I_0(\xi_m R_i)K_0(\xi_m r)}{I_0(\xi_m R_e)K_0(\xi_m R_i) - I_0(\xi_m R_i)K_0(\xi_m R_e)} +$$

$$+\varrho_a^e \frac{I_0(\xi_m R_e)K_0(\xi_m r) - K_0(\xi_m R_e)I_0(\xi_m r)}{I_0(\xi_m R_e)K_0(\xi_m R_i) - I_0(\xi_m R_i)K_0(\xi_m R_e)},$$

where $I_0(\cdot), K_0(\cdot)$ are the modified Bessel functions of the first and second kinds, respectively.

Fig. 2 shows the density in the cylinder at $R_i/R_e = 0.2; 0.6$ (Fig. 2a and b), $\xi_m R_e = 3,6,12,50$ (curves 1–4).

DOI 10.2478/ama-2019-0027

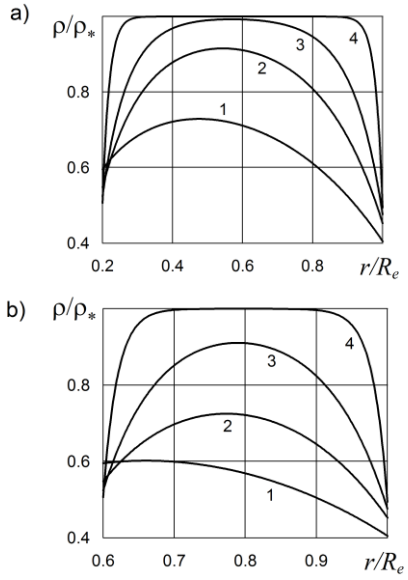

Fig. 2. Distribution of density

If the density ϱ is known, the components $\sigma_{rr}, \sigma_{\varphi\varphi}, \sigma_{zz}$ may be found using the formulae:

$$\sigma_{rr}(r) = a_0 \left[\frac{1}{R_e^2 - R_i^2}\left(1 - \frac{R_i^2}{r^2}\right)\int_{R_i}^{R_e}(\varrho(x) - \varrho_*)x\,dx - \right.$$

$$\left. -\frac{1}{r^2}\int_{R_i}^{r}(\varrho(x) - \varrho_*)x\,dx\right],$$

$$\sigma_{\varphi\varphi}(r) = a_0 \left[\frac{1}{r^2}\int_{R_i}^{r}(\varrho(x) - \varrho_*)x\,dx + \right.$$

$$\left. +\frac{1}{R_e^2 - R_i^2}\left(1 + \frac{R_i^2}{r^2}\right)\int_{R_i}^{R_e}(\varrho(x) - \varrho_*)x\,dx - \varrho(r) + \varrho_*\right], \quad (11)$$

$$\sigma_{zz}(r) = a_0 \left[\frac{2}{R_e^2 - R_i^2}\int_{R_i}^{R_e}(\varrho(x) - \varrho_*)x\,dx - \varrho(r) + \varrho_*\right],$$

where $a_0 = 2\mu a_m\,(3\lambda + 2\mu)/(\lambda + 2\mu)$. The explicit form of the formulae is cumbersome and so it is not presented here.

Figs. 3 and 4 show stresses σ_{rr}/σ_0 and $\sigma_{\varphi\varphi}/\sigma_0 (\sigma_0 = a_0\varrho_*)$, respectively, taking into account (Fig. 3a) and neglecting (Fig. 3b) the dependence of the density surface value on the surface curvature for $\xi_m R_e = 3,6,12,50$ (curves 1–4), $R_i/R_e = 0.2$.

The non-zero stress–strain state in the free body is caused by the mass defect, that is, the difference of the density in the current (actual) state and in the reference one (usually infinite homogeneous media). The distribution and value of stresses are uniquely determined by the characteristics of the material and the geometric characteristics of the body. Comparing Fig 3a and b, we see that taking into account the dependence of the surface value of density on the surface curvature is more significant in thin fibres. Taking into account this dependence can qualitatively change the stress distribution as it is illustrated in particular by the curves 1 in Fig. 3a and b.

Circumferential, $\sigma_{\varphi\varphi}$, and axial, σ_{zz} , stresses are tensile near inner $r = R_i$ and outer $r = R_e$ surfaces of the cylinder and they are compressing in the vicinity of the median surface $r = (R_i + R_e)/2$. Surface stresses $\sigma_{\varphi\varphi}(R_i) = \sigma_{zz}(R_i)$ and $\sigma_{\varphi\varphi}(R_e) = \sigma_{zz}(R_e)$ show size effect. This is exposed in Figs. 5 and 6. Fig. 5 shows the dependence of surface values of stresses $\sigma_{\varphi\varphi}(R_i)/\sigma_0$, $\sigma_{\varphi\varphi}(R_e)/\sigma_0$ (curves 1 and 2) on parameter $\xi_m R_e$ for $R_i/R_e = 0.2$. The dashed line corresponds neglecting the dependence of the density surface value on the surface curvature. Fig. 6 shows the dependence of the values of circumferential stresses at the outer surface of the cylinder $r = R_e$ on parameter R_i/R_e $(R_e - R_i = R_e(1 - R_i/R_e)$ is the thickness of the hollow cylinder wall).

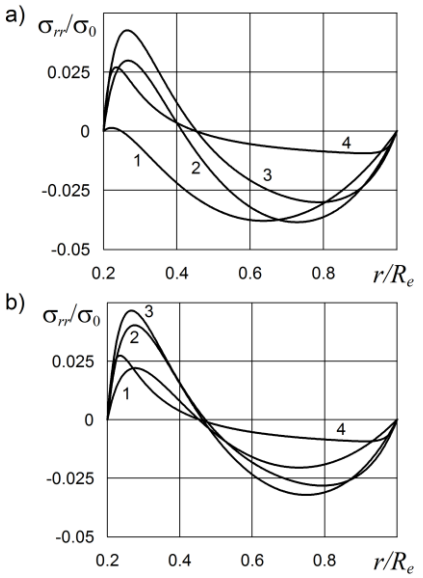

Fig. 3. Distribution of radial stresses

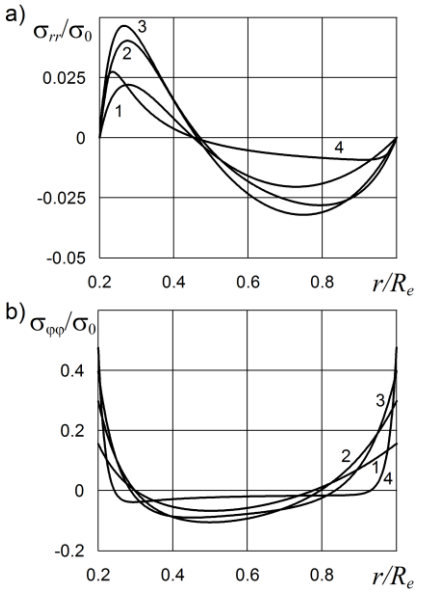

Fig. 4. Distribution of circumferential stresses

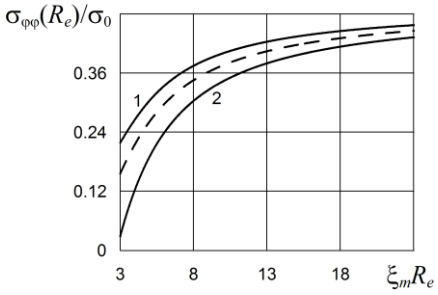

Fig. 5. Size effect of circumferential surface stress

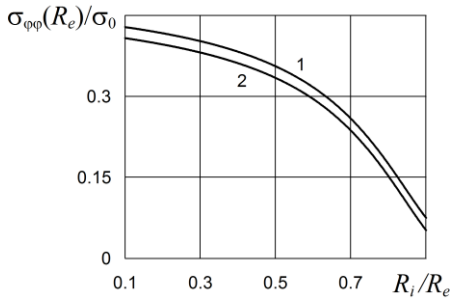

Fig. 6. Circumferential surface stress dependence on R_i/R_e

Taking into account internal stresses is important when calculating operational parameters. Superposing with external force load, they affect the strength characteristics. In the hollow cylinder which is under the action of the force load of intensity σ_a in the direction of the cylinder axis:

$$\int_0^{2\pi}\int_{R_i}^{R_e}\sigma_{zz}(r)r\,dr\,d\varphi = \pi(R_e^2 - R_i^2)\sigma_a$$

the greatest tensile stress is the stress σ_{zz} at the outer cylinder surface $r = R_e$ for which we can write:

$$\sigma_{zz}(R_e) = \sigma_a +$$

$$+a_0\left[\frac{2}{R_e^2-R_i^2}\int_{R_i}^{R_e}(\varrho(x)-\varrho_*)x\,dx - \varrho(R_e) + \varrho_*\right].$$

The method presented by Nahirnyj and Tchervinka (2018) was used to determine the hollow cylinder strength. We assume that the cylinder will fail immediately when the maximum principal stress in at least one point of the body exceeds the tensile strength of the material σ_f. On the basis of Eq. (12) for the load which leads to cylinder fracture, it can be written:

$$\sigma_{cr} = \sigma_+ +$$

$$+a_0\left[\varrho(R_e) - \frac{1}{2}\varrho_* - \frac{2}{R_e^2-R_i^2}\int_{R_i}^{R_e}(\varrho(x)-\varrho_*)x\,dx\right],$$

where:

$$\sigma_+ = \sigma_f - \mu a_m \varrho_* \frac{3\lambda+2\mu}{\lambda+2\mu}$$

is the material parameter which has the meaning of the strength of thick bodies.

Fig. 7 shows the dependence of σ_{cr}/σ_+ on parameter $\xi_m R_e$ (size effect of the strength of the hollow cylinder) for $\sigma_0/\sigma_+ = 16$, $R_i/R_e = 0.2; 0.6$ (curves 1 and 2). The dashed lines correspond to neglecting of the dependence of the density surface value on the surface curvature.

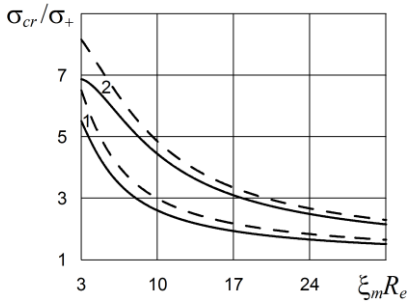

Fig. 7. Size effect of the strength of the hollow cylinder

We see that taking into account the dependence of the surface value of density on the surface curvature is important while calculating the strength of the thin fibres.

4. CONCLUSIONS

The study is concluded to the continual model of mechanics of locally heterogeneous solids which describes near-surface non-homogeneity and size effects caused by it. The key system consists of equations for stresses (displacements) and the equation for mass density. Formulation of boundary conditions for the mechanical fields and the density is necessary.

A non-zero stress-strained state in a free of external load body in the model is caused by the mass defect, that is, the difference of density in the current and reference states.

The article proposes the method to take properly into account the dependence of the surface value of density on the curvature of the surface. This is important in particular for studying thin fibres. The analysis of the boundary value problems (system of equations and boundary conditions) from the RVE viewpoint allows to determine the limits of applicability of the model as well.

Using the example of the hollow cylinder, it is shown that taking into account the dependence of the surface value of the density on the surface curvature leads to quantitative changes in the values of stresses and also qualitatively change their distribution in thin fibres. This allows correct comparison of stresses in fibres of different radii. (12)

When studying tensile strength of the stretched cylinder within maximum normal stresses theory, the account for the dependence of the surface value of density on the curvature of surface does not change the size effect regularities while reduces the value of the ultimate tensile strength.

REFERENCES

1. **Aifantis E. C.** (2011), On the gradient approach-relation to Eringen's nonlocal theory, *International Journal of Engineering Science*, 49(12), 1367–1377.
2. **Bargmann S., Klusemann B., Markmann J., Schnabel J. E., Schneider K., Soyarslan C., Wilmers J.** (2018), Generation of 3D representative volume elements for heterogeneous materials: A review,*Progress in Materials Science*, 96, 322-384.
3. **Bažant Z. P., Jirásek M.** (2002), Nonlocal integral formulations of plasticity and damage: Survey of progress,*Journal of Engineering Mechanics*, 128(11),1119–1149.
4. **Bostanabad R., Zhang Y., Li X., Kearney T., Brinson L., Apley D., Liu W., Chen W.** (2018), Computational microstructure characterization and reconstruction: Review of the state-of-the-art techniques,*Progress in Materials Science*, 95, 1-41.
5. **Burak Y., Nahirnyj T., Tchervinka K.** (2014), Local gradient thermomechanics, *Encyclopedia of Thermal Stresses*, 2794–2801.
6. **Cheng A. H-D.** (2016), *Poroelasticity*, Vol. 27, Springer.
7. **Di Paola M., Failla, G., Zingales M.** (2010), The mechanically-based approach to 3D non-local linear elasticity theory: Long-range central interactions, *International Journal of Solids and Structures*, 47(18-19), 2347-2358.
8. **Dormieux L., Kondo D.** (2013), Non linear homogenization approach of strength of nanoporous materials with interface effects, *International Journal of Engineering Science*, 71, 102–110.
9. **Dormieux L., Kondo D., Ulm F.-J.** (2006), *Microporomechanics,* John Wiley and Sons.
10. **Drugan W.J., Willis J.R.** (1996), A micromechanics-based nonlocal constitutive equation and estimates of representative volume element

DOI 10.2478/ama-2019-0027

size for elastic composites, *Journal of the Mechanics and Physics of Solids*, 44(4), 497–524.
11. **Eringen A. C.** (2002), *Nonlocal continuum field theories*. Springer.
12. **Guo N., Zhao J.** (2016), 3D multiscale modeling of strain localization in granular media, *Computers and Geotechnics*, 80, 360-372.
13. **Kanit T., Forest S., Galliet I., Mounoury V., Jeulin, D.** (2003), Determination of the size of the representative volume element for random composites: statistical and numerical approach,*International Journal of Solids and Structures*, 40(13-14), 3647–3679.
14. **Karlicic D., Murmu T., Adhikari S., McCarthy M.** (2015), *Non-local structural mechanics*. John Wiley and Sons.
15. **Khodabakhshi P., Reddy J. N.** (2015), A unified integro-differential nonlocal model, *International Journal of Engineering Science*, 95, 60-75.
16. **Kwok K., Boccaccini D., Persson Å. H., Frandsen H. L.** (2016). Homogenization of steady-state creep of porous metals using three-dimensional microstructural reconstructions, *International Journal of Solids and Structures*, 78, 38-46.
17. **Marotti de Sciarra F.** (2009), On non-local and non-homogeneous elastic continua, *International Journal of Solids and Structures*, 46(3), 651–676.
18. **Matouš K., Geers M. G., Kouznetsova V. G., Gillman A.** (2017), A review of predictive nonlinear theories for multiscale modeling of heterogeneous materials, *Journal of Computational Physics*, 330, 192-220.
19. **Monetto I., Drugan W. J.** (2009), A micromechanics-based nonlocal constitutive equation and minimum RVE size estimates for random elastic composites containing aligned spheroidal heterogeneities,*Journal of the Mechanics and Physics of Solids*, 57(9), 1578-1595.
20. **Nahirnyj T., Tchervinka K.** (2015), Mathematical Modeling of Structural and Near-Surface Non-Homogeneities in Thermoelastic Thin Films,*International Journal of Engineering Science*, 91, 49–62.
21. **Nahirnyj T., Tchervinka K.** (2018), *Fundamentals of the mechanics of locally non-homogeneous deformable solids*, Lviv: Rastr-7 (in ukr).
22. **Polizzotto C.** (2003), Gradient elasticity and nonstandard boundary conditions, *International Journal of Solids and Structures*, 40(26), 7399–7423.
23. **Polizzotto C.** (2012), A gradient elasticity theory for second-grade materials and higher order inertia, *International Journal of Solids and Structures*, 49 (15), 2121–2137.
24. **Rezakhani R., Zhou X.W., Cusatis G.** (2017), Adaptive multiscale homogenization of the lattice discrete particle model for the analysis of damage and fracture in concrete, *International Journal of Solids and Structures*, 2017, 125, 50-67.
25. **Saeb S., Steinmann P., Javili A.** (2016), Aspects of computational homogenization at finite deformations: a unifying review from Reuss' to Voigt's bound, *Applied Mechanics Reviews*, 68(5), 050801.
26. **Salmi M., Auslender F., Bornert M., Fogli M.** (2012), Various estimates of Representative Volume Element sizes based on a statistical analysis of the apparent behavior of random linear composites,*Comptes Rendus Mécanique*, 340(4-5), 230-246.
27. **Silling S.A.** (2000), Reformulation of Elasticity Theory for Discontinuities and Long-Range Forces. *Journal of the Mechanics and Physics of Solids*, 48, 175–209.
28. **Sneddon I.N., Berry D.S.** (1958), *The Classical Theory of Elasticity*. In: Flügge S. (eds) Elasticity and Plasticity / Elastizität und Plastizität. Handbuch der Physik / Encyclopedia of Physics, 3/6, Springer, Berlin, Heidelberg.
29. **Wang Q., Liew K.** (2007), Application of nonlocal continuum mechanics to static analysis of micro- and nano-structures, *Physics Letters A*, 363(3), 236–242.
30. **Wiśniewska A., Hernik S., Liber-Kneć A., Egner H.** (2019), Effective properties of composite material based on total strain energy equivalence, *Composites Part B: Engineering*, 166, 213-220.

sciendo

DOI 10.2478/ama-2019-0028

acta mechanica et automatica, vol.13 no.3 (2019)

PICK-AND-PLACE TASK IMPLEMENTATION USING VISUAL OPEN-LOOP CONTROL

Paweł KOŁOSOWSKI,[*] Adam WOLNIAKOWSKI,[**] Mariusz BOGDAN[*]

[*]Faculty of Mechanical Engineering, Bialystok University of Technology, ul. Wiejska 45C, Białystok 15-351, Poland
[**]Faculty of Electrical Engineering, Bialystok University of Technology, ul. Wiejska 45D, Białystok 15-351, Poland

pawelkolosowski0@gmail.com, a.wolniakowski@pb.edu.pl, m.bogdan@pb.edu.pl

received 10 July 2019, revised 30 October 2019, accepted 31 October 2019

Abstract: In the ever increasing number of robotic system applications in the industry, the robust and fast visual recognition and pose estimation of workpieces are of utmost importance. One of the ubiquitous tasks in industrial settings is the pick-and-place task where the object recognition is often important. In this paper, we present a new implementation of a work-piece sorting system using a template matching method for recognizing and estimating the position of planar workpieces with sparse visual features. The proposed framework is able to distinguish between the types of objects presented by the user and control a serial manipulator equipped with parallel finger gripper to grasp and sort them automatically. The system is furthermore enhanced with a feature that optimizes the visual processing time by automatically adjusting the template scales. We test the proposed system in a real-world setup equipped with a UR5 manipulator and provide experimental results documenting the performance of our approach.

Key words: Grasping, pick-and-place, object recognition, template matching, visual servoing

1. INTRODUCTION

A typical configuration of a pick-and-place task is presented in Fig. 1. A vision system is used to recognize and estimate the pose of objects located in the workcell. This information is subsequently used by the user application to control the robotic manipulator in order to grasp the objects and place them in the designated target areas. Such a setup typically requires accurate calibration.

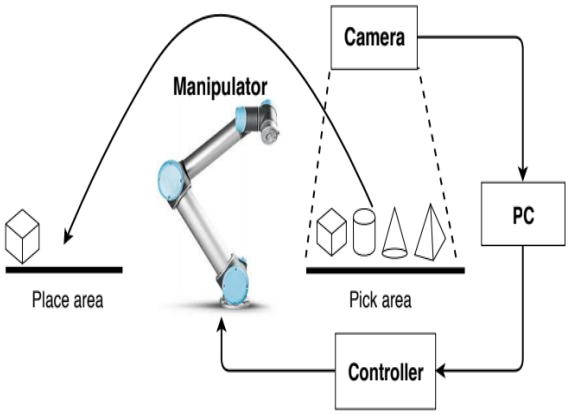

Fig. 1. Typical pick-and-place task

In this paper, we present an implementation of a 2D object recognition and sorting task using a robot manipulator and a vision system.

The successful execution of the pick-and-place task, where multiple types of objects are present, requires solving an object recognition problem. In recent years, the problem of sorting of objects of different shape, size and colour was extensively researched in the literature (Saxena et al., 2007; Kumar et al., 2014; Willaume et al., 2016; Nalini and Gondkar, 2017).

The research is often focused on the problems encountered in successful implementation of the system. These problems in the context of the pick-and-place task revolve around two most important aspects: quick and correct visual recognition of the object, and a stable grasp (Amagai and Takase, 2017).

On the vision system side, the current trend in the industry is to replace the mechanically forced object position with 'smart' recognition by the use of a vision based object recognition (Steger et al., 2017). The performance of the vision system is chiefly impacted by the object complexity, the number of objects present in the scene, the lightning conditions and the calibration quality. Solving the generalized vision problem is often not feasible due to practical considerations. Therefore, research on visual based object recognition is usually restricted to particular classes of the objects, for example, geometrical characteristics, colour or size. Despite significant progress in the recent years, still there are issues that are not handled by the vision systems very well. These include, for example, segmentation and recognition of non-rigid objects, where the observed shape is allowed to vary and there is lightning imbalance due to shadows, reflections and the object texture (Hagelskjær et al., 2017).

Object recognition is an interesting research area, very important in robotic applications. Multiple methods are currently known. One of the earliest approaches involved matching the features of the known object model (Grimson, 1990; Ellgammal, 2005; Sibiryakov, 2008) or shape primitives based recognition (Krivic and Solina, 2004; Nieuwenhuisen et al., 2012,). Currently, a very popular trend is to use machine learning algorithms (Cabre et al., 2013). Most of these approaches rely on the feature extrac-

DOI 10.2478/ama-2019-0028

tion and matching methods, such as SIFT (Lowe, 2004; Collet, et al. 2011) or SURF (Bay et al., 2008). SIFT algorithm is robust in respect to cluttered background, perspective shift, lightning conditions, scaling and rotation, but requires precise image segmentation. SURF is considered to have better performance. Still, both of these methods suffer issues due to uniform colour scheme and smooth contours of the recognized objects.

The vision systems used in industry and research can be classified into different categories. One of such classifications involves the distinction on the camera placement, which can be fixed in the workcell or attached to the robot manipulator (Chaumetter and Hutchinson, 2007; Corke, 2001; Flandin et al., 2000). The latter case has recently resulted in the emergence of the visual servoing methods (Pessoa et al., 2018; Huang and Xu, 2018; Amini and Banitsas, 2019). Both types of the vision systems offer advantages and shortcomings. The fixed camera system offers higher precision due to the stability of the calibration, while suffering from the limitation to the observed area and just one perspective. The moving camera allows for the observation of the scene from multiple vantage points, while having lower precision at the same time. Typically, the fixed camera vision systems are still used in most scenarios. The overview of our proposed system is presented in Fig. 2. Our system is divided into two parts: the offline template scale optimization process and the online process executed during the pick-and-place task realization. Both branches of the system share the first two steps: the image acquisition using the vision system and the image rectification, where the distortions are removed from the acquired image. This is performed based on the intrinsic camera calibration.

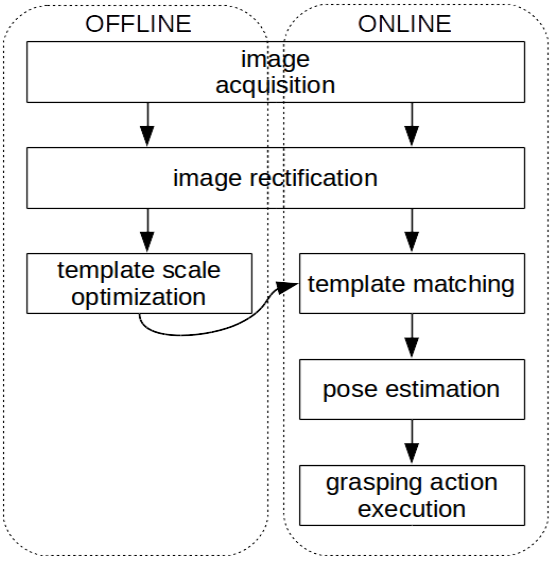

Fig. 2. Proposed system implementation workflow diagram

The offline branch of the system is responsible for preparing the templates for the template matching algorithm. Poor extrinsic camera-to-robot calibration – or even lack thereof – necessitates the assumption of multiple scales of templates, which greatly increases the computation time in the online phase. Our proposed solution uses this offline step to select the template scale that matches the object scale in the scene, thereby improving the vision system processing rate.

The online branch of our system is concerned with controlling the manipulator in order to perform the pick-and-place task based on the information on the recognized object pose obtained through the vision system. We have subsequently tested our proposed approach in an industrial-based real experiment. We provide quantitative results on the performance of our template matching system, thereby proving the feasibility of its implementation in automizing pick-and-place tasks.

2. METHODS

In this section, we present the detailed description of the individual components of our template matching system.

2.1. Template matching

Template matching is an image recognition technique based on comparing the predefined image (template) against the source image, in order to find areas with highest similarity. In this method, the template is sled over the source image and the ratio of similarity is computed, which describes how well the template matches the image in specific position, according to the specified method. There are several comparison methods; we have chosen normalized correlation coefficient, which is described in the equation (1).

$$R(x,y) = \frac{\sum_{x',y'} T'(x',y') * I'(x+x',y+y')}{\sqrt{\sum_{x',y'} T'(x'y')^2 * \sum_{x',y'} I'(x+x',y+y')^2}} \quad (1)$$

where: I is image, T - template, R - matrix of matching results that contains values between 0 and 1, where 1 means perfect match and 0 means a complete mismatch.

Template matching is a computationally complex algorithm the execution time of which increases with template and source image resolution. To speed-up the process, we used templates with lowest possible resolution, which maintained the geometry of the objects (i.e., lowest template resolution for which the different objects were still distinguished). We define the ratio between the actually used template width and this normalized width as the template scale.

Owing to the fact that template matching algorithm is not scale and rotation invariant, there is a necessity to generate templates in multiple scales and rotation angles. Scaling is usually performed by generating image pyramid with downsamples or upsamples of the given template. However, we have implemented a less time-consuming approach by using only one optimal preprocessed scale for every template (see 2.2). In order to define object rotation, every template has been rotated in range from 0° to 360° every 2°.

The grasping poses can be defined for the objects by the user as the transform between the object's CoG and the desired grasp pose. In case the grasp pose is not defined, an identity transform is assumed by default.

2.2. Template scale optimization

Since the system is designed to handle typical pick-and-place actions with the objects placed in the constant distance to the camera, no variation of the object image size is expected. Still, without prior camera-to-table pose calibration, the apparent size of the image is unknown. In order to escape the necessity of per-

forming the time-consuming extrinsic calibration, it is possible to find the optimal template scale in the template pre-processing phase.

In order to find a scale that provides the highest recognition efficiency for the given template, we have taken 20 images of scenes with single object placed in various orientations. For each scene, template has been generated in wide range of scales and compared against the object segmented from the scene. The optimal scale for the template has been designated as an average of those template scales, which gave the highest correlation coefficient value for every image. The results of this process in our experiment are presented in Section 3.3.

2.3. Experimental setup

A laboratory setup at BUT was used to perform the real world experimental testing of the proposed method. The setup consists of a UR5 manipulator mounted in the aluminium frame workcell (see Fig. 3). The objects were placed on the surface of the table, where areas were designated for the object picking and placement. The camera used was 1280 x 1024 [px] uEye Camera.

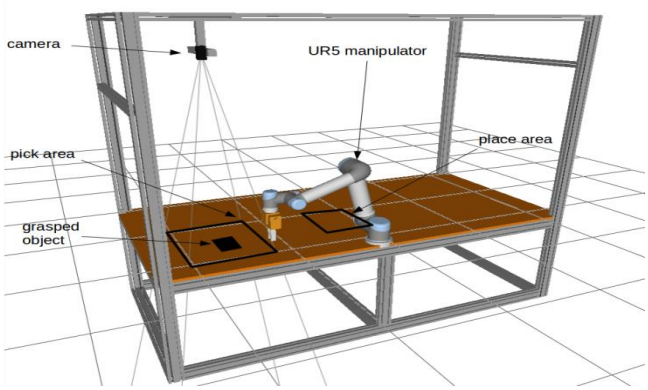

Fig. 3. The experimental setup modelled in RobWorkStudio

The UR5 manipulator used in the setup was equipped with a Schunk EVG55 electric gripper. The manipulator is capable of reaching the objects placed in the designated area and lifting up to 5 kg of weight. The experimental setup configuration is presented in Fig. 4. The ROS (Robot Operating System) package controlling the hardware is running on the laboratory workstation. The vision algorithm uses the OpenCV library to connect with the camera and process the image. The application uses ROS topics and services to control the robot and the gripper.

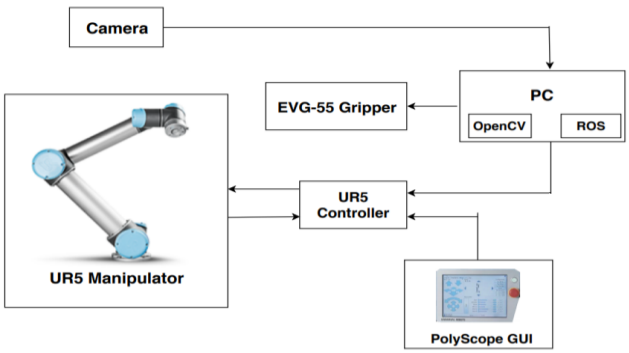

Fig. 4. The experimental setup configuration

3. RESULTS

In order to test the performance of our template matching vision system in the real setup, we have executed a pick-and-place experiment. We have tested our recognition algorithm with high success rate for both simple and complex object geometries. For the experiment, we have selected three objects: crank (object 1), bracket (object 2) and spacer (object 3). These objects are presented in Fig. 5. The objects were selected such as to have sparse visual features. The two objects (crank and bracket) were chosen such as to test the capability of the system to distinguish between similar shapes. The third object (spacer) was provided as the control.

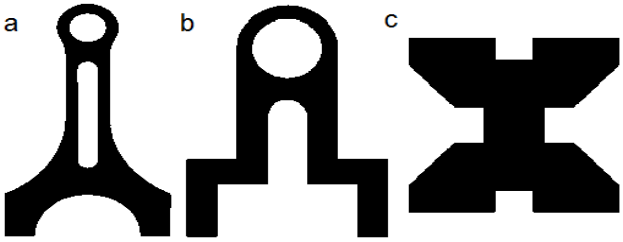

Fig. 5. The objects selected for the experiment: a) crank; b) bracket; c) spacer

The experiment was performed as described below.

3.1. Camera calibration

Firstly, the intrinsic camera calibration was performed in order to rectify the distortion of the image. The calibration was done by presenting a chessboard calibration pattern to the sensor in 130 poses and extracting the intrinsic camera matrix. This calibration was done using the OpenCV software package (Bradski, 2000). Next, the intensity analysis was performed in order to account for the lightning influence on the threshold for image segmentation (see Fig. 6). Sample images were taken, and the intensity histogram generated, from which the segmentation threshold was derived. We used the following formula to calculate the segmentation threshold (2).

$$\mathrm{I}_{thr} = 0.5(\mathrm{I}_{obj\_max} + \mathrm{I}_{bg\_max}) \quad (2)$$

where: I_{thr} – segmentation threshold; I_{obj_max} – object histogram peak; I_{bg_max} – background histogram peak (see Fig. 6c).

a)

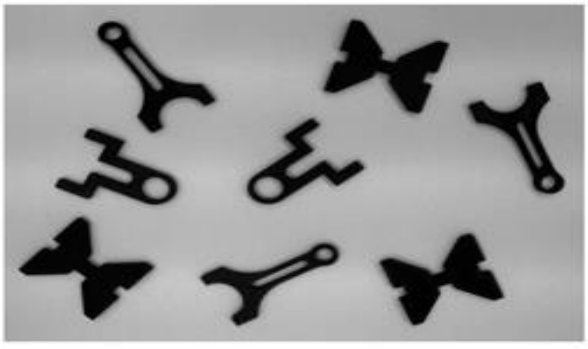

DOI 10.2478/ama-2019-0028

b)

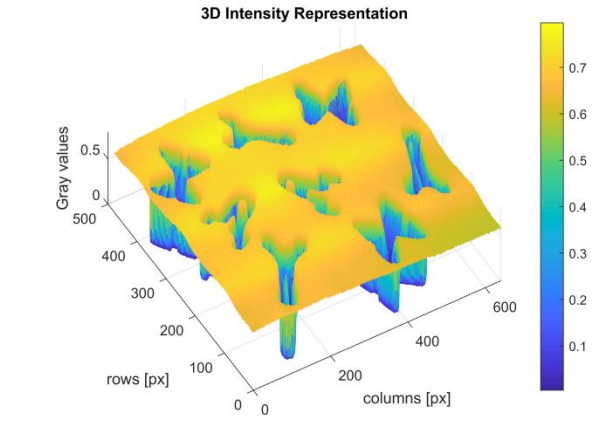

c)

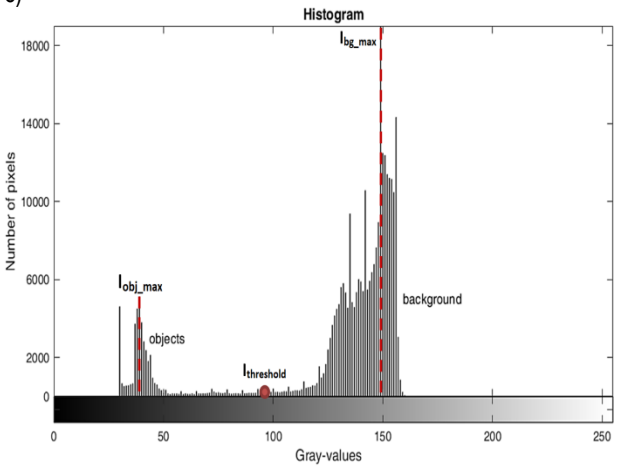

Fig. 6. Image intensity analysis: a) Sample camera image; b) 3D image intensity representation; c) Sample image intensity histogram

3.2. Image-to-robot calibration

In order to find the correspondence between the image pixel coordinates and the robot workspace coordinates, it was necessary to find the transform between the two. Since the designated grasping area was placed on the same plane as the robot base, the process was simplified to the problem of finding an affine transformation between the image space and the base plane. In order to find the transformation, we measured a set of positions uniformly distributed in the camera field of view obtaining both the pixel coordinates $[u, v]$ and the robot TCP $[x, y, \theta]$ coordinates. We then obtained the transformation matrix T using least square optimization (3):

$$\mathbf{T} = \begin{bmatrix} x_1 & y_1 & \theta_1 \\ x_2 & y_2 & \theta_2 \\ \vdots & \vdots & \vdots \\ x_n & y_n & \theta_n \end{bmatrix} \begin{bmatrix} u_1 & v_1 & 1 \\ u_2 & v_2 & 1 \\ \vdots & \vdots & \vdots \\ u_n & v_n & 1 \end{bmatrix}^{+} \tag{3}$$

where: u_1 and v_1 are the image pixel coordinates, while x_1, y_1 and θ_1 are the robot TCP coordinates and *n* is the number of the calibration samples taken.

The obtained transformation matrix **T** was then used to find the robot TCP target coordinates as the function of the image coordinates (4).

$$\begin{bmatrix} x \\ y \\ \theta \end{bmatrix} = \mathbf{T} \begin{bmatrix} u \\ v \\ 1 \end{bmatrix} \tag{4}$$

In our experiment, we used 24 calibration samples and obtained the 0.92 [mm] RMSE value for the coordinate transform between the image and the robot frame coordinates.

3.3. Optimal Template Scaling

The next step of our experiment was to find the optimal template scales for the three selected objects. For each of the objects, a set of scaled templates was generated and tested against the baseline camera image. For each of these scales, the correlation coefficient was computed and the optimal scaling factor was found. The relationship between the template scale and the matching score for the analysed objects is presented in Fig. 7.

a)

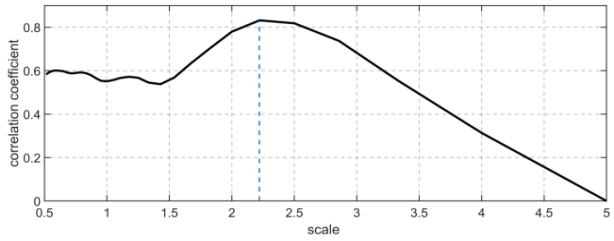

b)

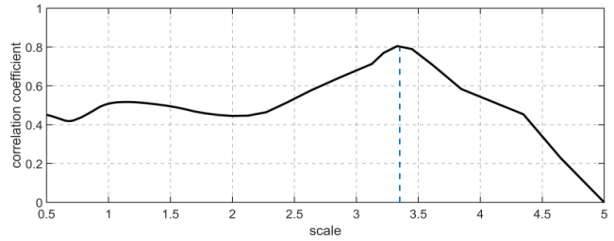

c)

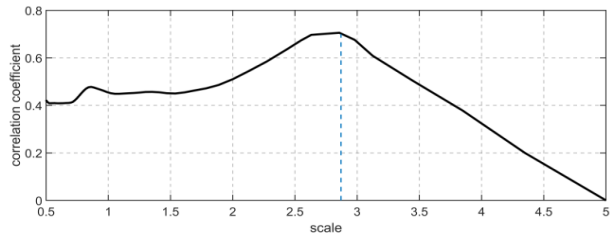

Fig. 7. The correlation coefficient as the function of template scale for three considered objects: a) Object 1 – crank; b) Object 2 – bracket; c) Object 3 – spacer

The following template sizes were chosen based on these results: 2.22; 3.40; 2,83 for object 1 (crank) 20 x 34 [px] template, 2 (bracket) 30 x 39 [px] template and 3 (spacer) 30 x 36 [px] template respectively.

The processing time for the object recognition also depends on the selected template resolution. The average recognition time for different template resolutions are shown in Fig. 8. In this work, we select the template scale based on the matching score, but it is conceivable to introduce a trade-off when faster on-line processing is required.

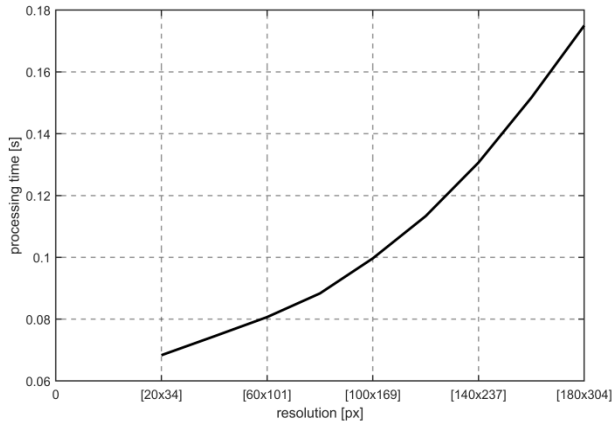

Fig. 8. Average single object recognition time as the function of template resolution

3.4. Manipulator control

In order to perform pick-and-place task, online-generated manipulator trajectory has been planned with the usage of recognized objects CoGs, rotations angles and desired grasp poses. Robot control was realized through point-to-point motions' implementation provided by the manufacturer. Pick-and-place actions were realized through linear movement in the Cartesian space, while simple joint-space point-to-point movements were used for the transfer of the pieces. The UR5 robot achieves +/- 0.1 [mm] repeatability according to the manufacturer.

3.5. Pick-and-place task

In the grasping task, the system was used to recognize and estimate the pose of 6 objects (2 of each kind) placed in the designated picking area as shown in Fig. 3. The camera image was captured and upon processing, the objects were grasped and placed in the target area. This action was repeated 50 times, and thus, 300 recognitions were performed (6 objects viewed 50 times). In this experiment, each object was expected to be recognized 100 times. During the experiment, we analysed whether the objects were correctly recognized and if they were placed in the proper target areas. The data collected during this experiment is presented in the Tab. 1 below.

Tab. 1. The confusion matrix of the cumulated experimental results

	Recognized as:			
	Object 1	**Object 2**	**Object 3**	**Not recognized**
Object 1	100	0	0	0
Object 2	0	100	0	0
Object 3	0	0	98	2

99.33% was achieved, where only the third type of object (the spacer) was not recognized in two cases. The results gathered in the confusion matrix suggest that the proposed method performs well. We have additionally recorded the vision processing time in order to track the system performance. We have achieved 0.21 [s] average recognition time per scene.

4. CONCLUSIONS

In this paper, we have presented a new implementation of the template matching algorithm applied to the solving of an industrial based pick-and-place task, where the grasped objects are characterized by few visual features. This property of the objects often makes the task impossible to solve using sophisticated vision algorithms, which rely on multiple and distinct features. We have proposed and described a two part system, in which an offline template scale optimization is introduced in order to improve the online vision system performance. The introduced system allows the user to present the object templates and define the grasping pose using an intuitive GUI.

We have tested the proposed method in a real-world setting using a robotic setup equipped with an UR5 manipulator. Three object shapes were selected for the experiment in order to test the ability of the system to distinguish distinct geometric shapes. The experiment provided the information on the success rate of the object recognition, the rate of successful grasping and the achieved processing time. A 99.33% success rate was achieved by the system, where only one kind of an object was not recognized twice in 100 samples. The average processing time achieved was 0.21 [s] per scene, which is sufficient for an online implementation. The results obtained in the experiment support the feasibility of our proposed approach. Still, the system setup requires some cost in terms of the need for calibration. The future work should be focused on reducing the setup time required, such as performing automatic camera-to-robot calibration.

REFERENCES

1. **Amagai A., Takase K.** (2001), Implementation of dynamic manipulation with visual feedback and its application to pick and place task, *Proceedings of the 2001 IEEE International Symposium on Assembly and Task Planning Assembly and Disassembly in the Twenty-first Century,* 344–350.
2. **Amini A., Banitsas K.** (2019), Using Kinect v2 to Control a Laser Visual Cue System to Improve the Mobility during Freezing of Gait in Parkinson's Disease, *Journal of Healthcare Engineering,* art. no. 3845462.
3. **Bay H., Tuytelaars T., Gool L.V.** (2008), Speeded-up robust features (SURF), *Computer Vision and Image Understanding*, 110, 346–359.
4. **Bradski G.** (2000), The OpenCV Library, *Dr. Dobb's Journal of Software Tools*.
5. **Cabre T.P., Cairol M.T., Calafell D.F., Ribes M.T., Roca J.P.** (2013), Project-Based Learning Example: Controlling an Educational Robotic Arm with Computer Vision, *Tecnologias del Aprendizaje, IEEE Revista Iberoamericana de, 8,* 135–142.
6. **Chaumette F., Hutchinson S.** (2007), Visual Servo Control, Part II: Advanced Approaches*, IEEE Robotics and Automation Magazine,* 14(1), 109–118.
7. **Collet A., Martinez M., Srinivasa S.S.** (2011), The MOPED framework: object recognition and pose estimation for manipulation, *The International Journal of Robotics Research,* 30, 1–23.
8. **Corke P.** (2001), Robotics, Vision and Control: Fundamental Algorithms in MATLAB, *Springer*.
9. **Ellekilde L.-P., Jorgensen J. A.** (2010), Robwork: A flexible toolbox for robotics research and education, *Proceedings of the 41st International Symposium on Robotics and 6th German Conference*, 1–7.
10. **Ellgammal A.** (2005), Object Detection and Recognition, *Rutgers University*.

DOI 10.2478/ama-2019-0028

11. **Flandin G., Chaumette F., Marchand E**. (2000), Eye-in-hand/eye-to-hand co-operation for visual servoing, *Proceedings of the IEEE International Conference on Robotics and Automation*, 3, 2741–2746.
12. **Grimson W.** (1990), *Object recognition by computer: the role of geometric constraints*, MIT Press.
13. **Hagelskjær F., Krüger N., Buch A.G.** (2016), Does Vision Work Well Enough for Industry?, *Proceedings of the 13th International Joint Conference on Computer Vision, Imaging and Computer Graphics Theory and Applications.*
14. **Huang W., Xu H.** (2018), Development of six-DOF welding robot with machine vision, *Modern Physics Letters B,* 32, 34–36.
15. **Krivic J., Solina F.** (2004), Part-level object recognition using superquadrics, *Computer Vision and Image Understanding,* 95, 105–126.
16. **Kumar R., Kumar S., Lal S., Chand P.** (2014), Object detection and recognition for a pick and place robot, *Computer Science and Engineering 2014 Asia-Pacific World Congress,* 1–7.
17. **Lowe D.G.** (2004), Distinctive image features from scale-invariant keypoints, *International Journal of Computer Vision,* 60, 91–110.
18. **Nalini K.M., Gondkar R.R.** (2017), Robotic recognition for unstructured 2-D parts to pick and place objects, *2017 2nd IEEE International Conference on Recent Trends in Electronics, Information & Communication Technology,* 1478–1482.
19. **Nieuwenhuisen M., Stückler J., Berner A., Klein R., Behnke S.** (2012), Shape-primitive based object recognition and grasping, *Proceedings of the 7th German Conference on Robotics*.
20. **Pessoa R., Barbosa W., McLoughlin J., Kokaram A.** (2018), Visual Servo Control of a Micro Quad-copter as a Teaching Platform for Engineering, *29th Irish Signals and Systems Conference,* art. no. 8585355.
21. **Saxena A., Driemeyer J., Ng A.Y.** (2007), Robotic Grasping of novel Objects using Vision, *The International Journal of Robotics Research*, 27(2), 157–173.
22. **Sibiryakov A.** (2008), Statistical template matching under geometric transformations, *Discrete Geometry for Computer Imaginary, Proceedings of the 14th IAPR International Conference,* 225–237.
23. **Steger C., Ulrich M., Wiedmann C.** (2017), Machine Vision Algorithms and Applications, *Wiley-VCH.*
24. **Willaume P., Parrend P., Gancel E., Deruyver A.** (2016), The graph matching optimization methodology for thin object recognition in pick and place tasks, *2016 IEEE Symposium Series on Computational Intelligence*, 1–8.